Modelling of Simultaneous Transformations in Steels

Jiawen Chen

Fitzwilliam College

A thesis submitted for the degree of
Doctor of Philosophy

Department of Materials Science and Metallurgy

Univesity of Cambridge

England

February, 2009

Preface

This dissertation is submitted for the degree of Doctor of Philosophy at the University of Cambridge. The research described herein was conducted under the supervision of Professor H. K. D. H. Bhadeshia in the Department of Materials Science and Metallurgy, University of Cambridge, between October 2005 and September 2008.

Except where acknowledgement and reference are made to previous work, the work is, to the best of my knowledge, original. This dissertation is the result of my own work and includes nothing which is the outcome of work done in collaboration except where specifically indicated in the text.

Neither this, nor any substantially similar dissertation, has been or is being submitted for any other degree, diploma, or other qualification at any other university. This dissertation does not exceed 60,000 words in length.

Some of the work described herein has been published in the proceedings of the conference on *New Development on Metallurgy and Applications of High Strength Steels*, or in the proceedings of the 1st International Conference on *Interstitially Alloyed Steels*.

Jiawen Chen
May 13, 2009

Acknowledgements

Surely, the year has historical significance. Here, we are celebrating the Cambridge 800 anniversary. Inside academia, people are reviewing the 150 years after Darwin's On the Origin of Species. And across the world, markets are becoming irrational, many governments are flying in uncharted space. Looking forward, humanity will be challenged by the inevitable man-made environmental disasters.

Abstract

The microstructure of a steel is often developed by solid-state transformation from austenite. The major transformation products are allotriomorphic ferrite, pearlite, Widmanstätten ferrite, bainite and martensite, differentiated by morphological features, and their nucleation and growth mechanisms. A steel often consists of several phases as a result of dynamic evolution during continuous cooling. The complexity of the calculation of all the transformations simultaneously poses a challenge.

There have been a few attempts at integrating all these transformations into an unified scheme. They involve varying degrees of empiricism. For the first time, a model that can predict simultaneously the volume proportions of all the major transformation products has been developed. The algorithm has taken full account of the thermodynamics and kinetics of individual transformations, instead of empirical equations, so the model should in principle generalise well.

The predictions of the model are based on a number of input parameters: the chemical composition, austenite grain size and cooling conditions. The model can simulate cooling at constant rates, or isothermal transformations. Therefore it can also generate continuous cooling transformation (CCT), or time-temperature transformation (TTT) diagrams.

The model has demonstrated a consistency in its predictions. The validations of the model against published experiment data and experiments conducted in this work have shown the predictions in most cases are reasonable with errors less than a few volume percent. Further research opportunities presented by the work are reviewed.

Contents

Abbreviations

Term	Meaning
2D	2 dimensional
BCC	Body centred cubic
CCT	continuous cooling transformation diagram
CR	cooling rate
FCC	Face-centred cubic
GB	austenite grain boundaries
TTT	time-temperature transformation diagram

Nomenclature

α allotriomorphic ferrite

α/γ interface between ferrite and austenite

α' martensite

α_B bainite

α_W Widmanstätten ferrite

$\bar{L}$ mean linear intercept for an equiaxed grain structure

$\bar{x}$ average carbon concentration is steel

$\bar{D}$ weighted average diffusivity of carbon

$\Delta E_{\alpha/\theta}$ interfacial energy between ferrite and cementite in pearlite

$\Delta G^{\gamma \to \alpha}$ driving force for diffusionless transformation from austenite to ferrite

$\Delta G^{\gamma \to \gamma' + \alpha}$ driving force for reconstructive transformations

ΔG_m maximum driving force for nucleation

$\Delta O_{i,y}^e$ total extended area change of phase i on plane y

$\Delta O_{i,y}$ real change in area of phase i on plane y at current time step

Δt time interval of calculation

Δt_s time interval between two successive sub-units

ΔV_i^e extended change in volume of phase i

ΔV_i real change in volume of phase i at current time

Δy distance between two adjacent planes

$\Delta \bar{H}_\gamma$ partial molar heat of solution of carbon in austenite

$\Delta \bar{S}_\gamma$ partial molar non-configurational entropy of solution of carbon in austenite

$\Delta \underline{G}$ change of molar Gibbs free energy

$\eta^{\alpha w}$ ratio of thickness to length of a Widmanstätten particle

η^α ratio of radius to half the height of allotriomorphic ferrite

η^P ratio of radius to half the height of pearlite particle

γ austenite

$\mathcal{H}^{\alpha w}$ lengthening rate of a Widmanstätten plate

$\mathcal{H}^\alpha$ 1D parabolic thickening rate of allotriomorphic ferrite

$\mathcal{H}^P$ growth rate of pearlite at the direction of height

μ_C chemical potential of carbon

ν attempt frequency factor

ω_α carbon-carbon interaction energy in ferrite

ω_γ carbon-carbon interaction energy in austenite

ρ radius of curvature at the tip of Widmanstätten particle

ρ^c critical radius of curvature at the tip of Widmanstätten particle

$\sigma_{\alpha\gamma}$ energy per unit area of ferrite austenite interface

τ_{dis} transformation start time for the displacive transformations

τ_{rec} transformation start time for the reconstructive transformations

a_C^α activity of carbon in ferrite

a_C^γ activity of carbon in austenite

B_s bainite start temperature

D carbon diffusivity

G^* activation energy of homogeneous nucleation

G_{het}^* activation energy of heterogeneous nucleation

G_N universal nucleation function

g_P growth rate of pearlite

h Planck constant

H^{α_B} thickness of bainite sheaf

H^{α_W} thickness of Widmanstätten ferrite particle

H^α half-thickness of allotriomorph particle

H^P half-thickness of a pearlite colony

i designated for any phase

I_1 nucleation rate of allotriomorphic ferrite

I_2 nucleation rate of Widmanstätten ferrite and bainite

$I_{i,k}$ nucleation rate of phase i at time k

I_s nucleation rate of sub-unit

k Boltzmann constant

k designated for the time a particle nucleates

l_u length of a sub-unit

n current time interval

N_v number density of nucleation sites

O_B total area of austenite grain boundaries

P pearlite

p Péclet number

Q energy barrier for the transfer of an atom across the α/γ interface

R ideal gas constant

S_0 interlamellar spacing of pearlite

S_α thickness of the ferrite lamella

S_θ thickness of the cementite lamella

S_C critical spacing of lamellae of pearlite

S_u intersection area of a sub-unit

T absolute temperature

T_h the highest temperature at which displacive transformation starts

V total volume

$V_L^{\max}$ maximum lengthening rate of Widmanstätten particle

$V_{\alpha_B}^{\max}$ the maximum amount of bainite possible at any temperature

V_i total volume of phase i

V_L plate lengthening rate

W_s Widmanstätten ferrite start temperature

x mole fraction of carbon

x_m^α carbon concentration of the embryo having the maximum driving force

$x^{\alpha\gamma}$ carbon concentration in ferrite in equilibrium with austenite

$x^{\gamma\alpha}$ carbon concentration in austenite in equilibrium with ferrite

$x^{\gamma\theta}$ carbon concentration of austenite in equilibrium with cementite lamellae

y distance of the plane from the boundary

Chapter 1

General overview

1.1 Introduction

The critical role that steel has played in the construction of our society is largely
due to its superior adaptation to the wide ranges of mechanical requirements. The
strength and toughness of steel can vary with changes in its microstructure, i.e.,
the size and shape of grains and the detailed arrangement of the atoms.

Pure iron experiences two solid-state transformations during cooling from the
melting temperature of 1538 °C. It transforms from δ-ferrite, a body-centred cubic
(BCC) structure, to austenite γ, a face-centred cubic (FCC) structure, at 1390°C,
and then back into ferrite (BCC) α at 910 °C. Almost all steels rely on the trans-
formation between austenite and ferrite for obtaining the desired microstructure.

The transformation temperature between austenite and ferrite can be greatly
affected by the presence of solutes, such as carbon, silicon, manganese, nickel,
molybdenum, chromium and vanadium. For example, 0.8 wt % carbon lowers the
second solid-state transformation temperature from 910 °C to 723 °C.

The transformation temperature can also be altered by changing the cooling
rate from elevated temperatures. A rapidly cooled steel transforms at a lower tem-
perature, given the shorter amount of time available to accomplish the necessary
changes in atomic positions. The products of such transformation are metastable
phases. The advantage of fast cooling is that the structural scale is reduced, which
is conducive to greater strength and toughness.

1.2 The Phase Transformations in Steel

As already emphasised, the properties and performance of a steel depend on its microstructure. The major transformation products: allotriomorphic ferrite α, pearlite P, Widmanstätten ferrite α_W, bainite α_B and martensite α' are categorised by the way in which atoms move in order to achieve the change in crystal structure.

1.2.1 Displacive and reconstructive transformations

Solid-state transformation from austenite to ferrite can proceed either by a deformation of the FCC structure of austenite into the BCC structure of ferrite, a mechanism designated to be displacive. Alternatively, the transformation can proceed by breaking all the atomic bonds and rearranging the atoms to form the ferrite in a way which requires diffusion and which minimises strain energy. It is designated to be reconstructive mechanism (Fig. 1.1).
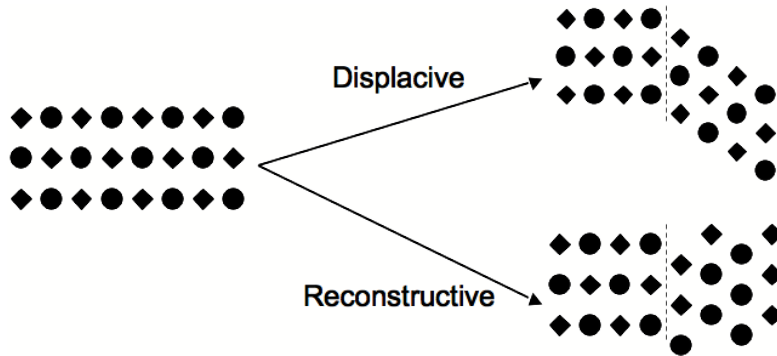
Figure 1.1: Displacive transformation is achieved by a deformation. In contrast, atomic bonds have to be broken in a reconstructive transformation and the diffusion of atoms is necessary. (After Bhadeshia [1])

An unconstrained displacive transformation can affect the shape of a material on a macroscopic scale. But when the material is constrained by the surrounding matter during the process, the displacive transformation products are forced to take the form of a thin plate, so the strain energy is reduced (Fig. 1.2).

Because the strain energy can largely be avoided in the reconstructive transformation, it is favoured from the thermodynamic point of view, though it may not be possible to sustain the necessary diffusion at low temperatures.
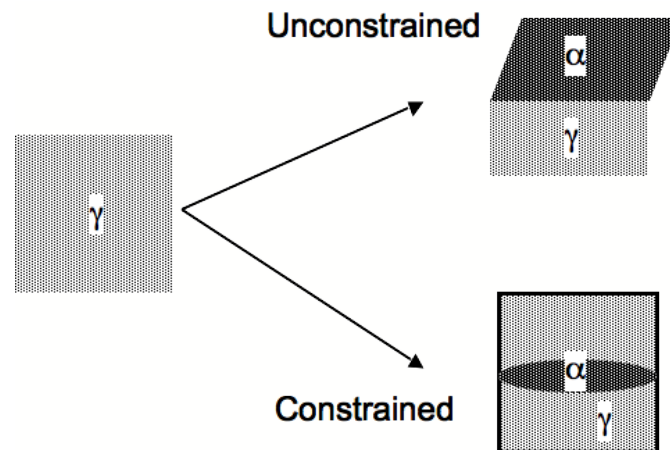
Figure 1.2: Unconstrained displacive transformation can cause a shape change on a macroscopic scale. When the displacive transformation is constrained by adjacent material, the minimisation of strain energy forces the product to grow into the shape of a thin plate. (After Bhadeshia [1])

1.2.2 The major transformation products in steel

As the name 'allotriomorph' suggests, this kind of ferrite does not exhibit obvious crystallographic facets. Allotriomorphic ferrite particles usually nucleate on and grow across the austenite grain boundaries. As the growth rate along the boundary is greater than that in the direction normal to the boundary, the shape of allotriomorph is heavily influenced by the shape of austenite grain boundaries. (Fig. 1.3).

Figure 1.3: Schematic illustration of allotriomorphic ferrite.

Pearlite colonies, P, have a lamellar structure of ferrite and cementite (Fe_3C).

17

As the spacing of the lamellae is often comparable with the wavelength of visible light, it resembles the pearlescent colour of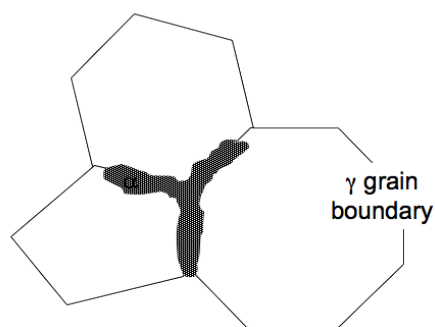 mother-of-pearl, from which it takes its name. Pearlite nucleation can take place on an austenite grain boundary, on cementite particles, or α/γ interfaces. The growth rate of pearlite is expected to be a constant in a binary Fe-C steel, because the average composition in pearlite equals that of the matrix austenite ahead of the advancing interface. However this may not be the case in ternary or higher order alloys if the growth involves the partitioning of substitutional solutes [2]. Being a reconstructive transformation, pearlite can also grow on both sides of the austenite grain boundary on which it nucleates (Fig. 1.4).
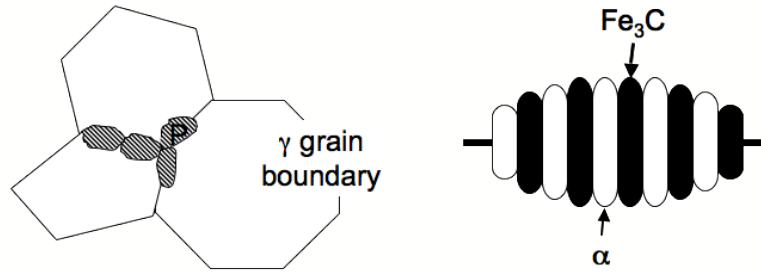

Figure 1.4: Schematic illustration of pearlite colonies. Pearlite has lamellar structure of ferrite and cementite (Fe_3C). It is emphasised that the lamellae are connected in three dimensions.

A Widmanstätten ferrite plate has the shape of a thin-wedge on a 2D metallography image, which on closer examination, consists of two adjacent plates. Widmanstätten ferrite, forms either directly on the austenite grain boundary, called primary α_W or on allotriomorphic ferrite, called secondary α_W. The plates grow on well defined lattice planes of austenite [3]. Having two Widmanstätten plates growing back to back results in a reduction of strain energy. This allows Widmanstätten ferrite to form at high temperatures with little driving force. Because of the displacive mechanism, Widmanstätten ferrite can only grow on one side of the austenite grain boundary (Fig. 1.5).

The microstructure of bainite consists of tiny platelets, called sub-units. The sub-units grow in clusters, called sheaves. When there is sufficient carbon diffusivity at the transformation temperature, carbon will be partitioned into the adjacent austenite, then precipitate as cementite. This form of bainite is called upper bai-
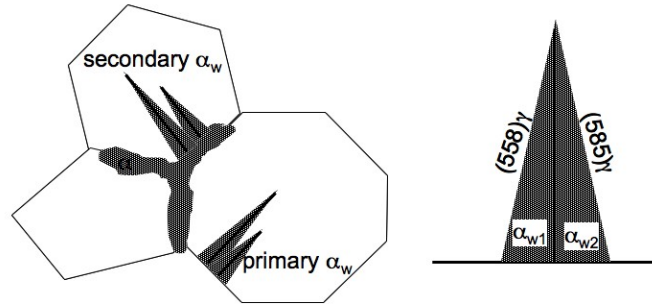
Figure 1.5: Schematic illustration of primary Widmanstätten ferrite and secondary Widmanstätten ferrite. The habit planes, on which the thin plates grow, belong to the same crystallographic family [3].

nite. During the transformation, the substitutional alloying elements are unable to partition during the time scale of the experiment, although carbon, which is a fast diffusing interstitial element, redistributes and reaches equilibrium. The mechanism is named 'paraequilibrium' [4].

The other form of bainite that is generated at lower temperature, called lower bainite, is very similar in microstructure to upper bainite. The major difference is that the cementite particles also precipitate inside the sub-units. A smaller amount of carbon is partitioned into the residual austenite.

Bainite evolves in distinct stages beginning with a sub-unit being nucleated at the austenite grain boundary. Each sub-unit can only achieve a limited size. Then the next sub-unit will be nucleated in the carbon-enriched austenite. This process ceases when the free energy of bainite is no less than that of austenite of the same composition. Because of the displacive mechanism, bainite sheaves are always limited to grow within the austenite grain in which they nucleate (Fig. 6.13).

Martensite is not directly calculated in the model that will be described later. Unlike reconstructive transformations, martensite is generated by a combination of shear and dilatation of the austenite lattice without any diffusion of atoms. The strain causes large volume expansion, which can be indicated by a sharp dilatation measure. Martensite reaction depends on the undercooling below the martensite-start temperature. The transformation mechanisms of the phases discussed so far are summarised in Fig. 1.7.
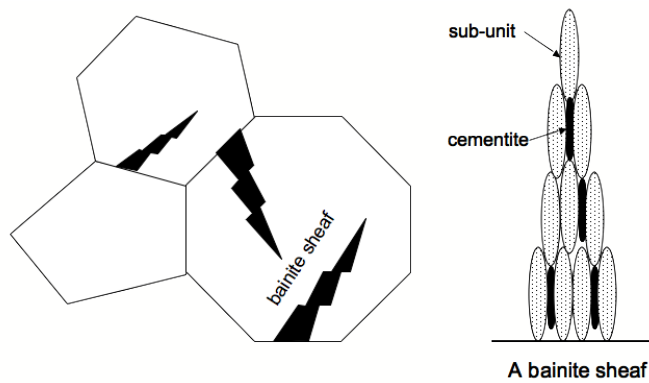
19

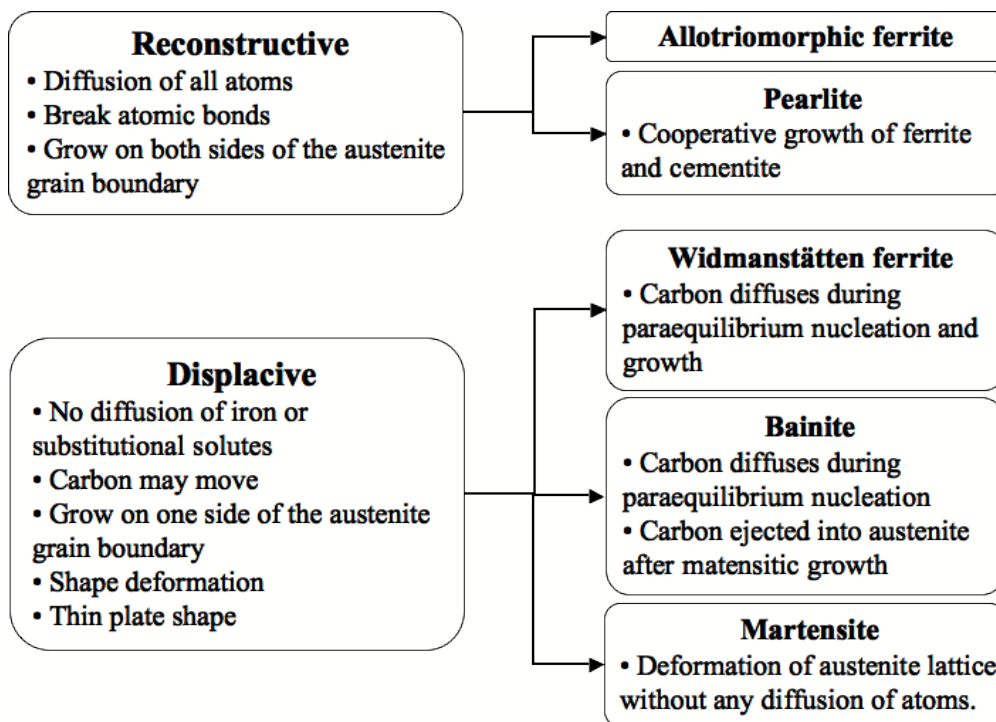Figure 1.6: Schematic illustration of bainite sheaves.

Figure 1.7: Transformation mechanisms of various phases in steel (after Bhadeshia [1]).

1.3   The Purpose

Most scientific subjects approach problems with the aid of modelling [5]. A model is often based on a selection of observations and perhaps some assumptions. It is an attempt to understand quantitatively some aspects of a infinitely varied reality.

The evolution of microstructure in steel is a complex and dynamic process involving simultaneous transformations of different types of phases. All the products compete for the limited nucleation sites, resources and space. A fast cooling condition can preserve the austenite into lower temperature regions, so that finer structure prevail. When many transformations occur at the same time, the fast reaction may consume much of the austenite. The migration of carbon through interstices, the creation rate of nuclei on the austenite grain boundaries, the growth rates of individual phases etc., all, react and interact with each other.

Previous attempts at integrating all these transformations into an unified scheme have varying degrees of empiricism and none of these models have a simultaneous transformation framework [6, 7, 8, 9, 10].

The research aim was to develop an algorithm which allows all of the key transformations, particularly bainite to be integrated into an unified calculation as a function of steel composition, austenite grain size and thermal processing. A logic flow chart is presented in Appendix B. The intention was to permit all processes to occur simultaneously at the rates consistent with the relevant thermodynamic and kinetic parameters. It should then become possible to track the fractions of each phase as the microstructure evolves.

Chapter 2

The Driving Forces

The reaction rate of a transformation can be controlled by the available Gibbs free energy, also referred to as the "driving force", and by the diffusivity of carbon.

2.1   The Influence of Carbon in Steel

Carbon is the single most important element in steel. Even in concentrations as low as 0.005 wt % it can dramatically change the strength of steel and cause a sharp transition between elastic and plastic deformation (including the upper and lower yield points A and B respectively in Fig. 2.1). The explanation of this
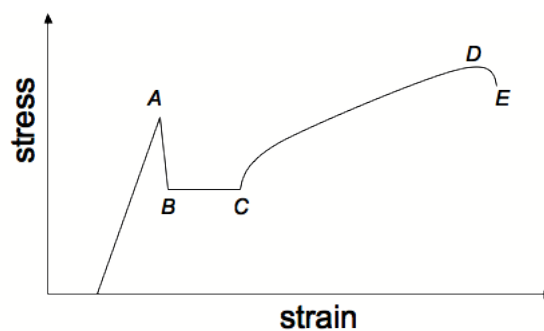

Figure 2.1: A typical tensile test result shown as stress versus strain. Point A is the upper yield point, point B is the lower yield point, involving the propagation of a Lüders band, i.e., a localised region of yielding which then spreads along the gauge length of sample, point D is the ultimate strength and point E where rupture occurs.

phenomenon first came from a model introduced by Cottrell and Bilby [11]. Unlike the larger substitutional alloying elements, carbon atoms occupy the octahedral interstices of the ferrite lattice. The strain fields around carbon atoms interact strongly with those of dislocations. When a carbon atom moves to the vicinity of a dislocation, there will be an overall reduction of strain energy. Carbon atoms tend to migrate towards dislocations until they form an 'atmosphere', which locks the positions of the dislocations. It takes energy for any dislocation to break away from its atmosphere, causing a sharp yield point.

2.1.1 The iron-carbon phase diagram

Features of the binary iron-carbon phase diagram persist in the whole variety of complex steels. A knowledge of this system therefore forms the foundation on which the effects of other alloying elements are interpreted. This makes the Fe-C phase diagram the starting point in the study of steels. There are five single-phase fields: molten steel (L), δ-ferrite, austenite (γ), ferrite (α) and cementite (C) (Fig. 2.2).
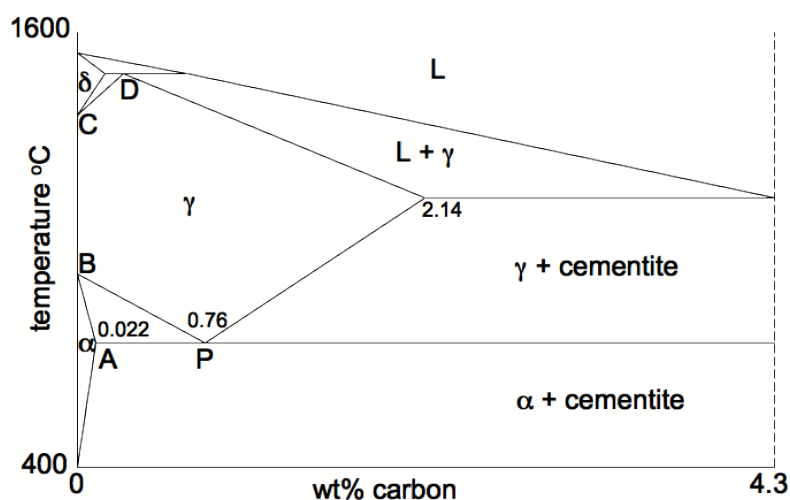

Figure 2.2: Schematic illustration of the iron-carbon phase diagram.

There are several critical temperatures to consider. Firstly, there is the Ae_1 temperature (line A-P) of the eutectoid reaction. Then, there is the Ae_3 temperature (line A-B) at which ferrite transforms to austenite. Finally there is the

Ae_4 (C-D) at which austenite transforms to δ ferrite (Fig. 2.2). These critical temperatures are diffusion controlled. Therefore, they are sensitive to heating and cooling rates. Rapid temperature change allows less time for diffusion. The critical temperatures at rapid heating Ac (arrêt chauffant), tends to be above those associated with equilibrium, and rapid cooling tends to lower the critical temperatures Ar (arrêt refroidissant). The Fe-C diagram enables the carbon concentrations of austenite and ferrite to be evaluated at any temperature.

The equilibrium solubility of carbon in austenite is greater than ferrite. During, or subsequently to, the transformation from austenite to ferrite, carbon is partitioned into the untransformed austenite. The ever increasing carbon concentration in the austenite ahead of the moving α/γ interface retards the diffusion of carbon, because it then needs to diffuse over a larger distance. As the diffusion of carbon in austenite is the slower process, it control the growth rate of ferrite particles.

2.1.2 The activities of carbon in ferrite and austenite

The activities of carbon in ferrite and austenite are needed in the later calculations of diffusivity of carbon and driving forces. In the current work, the equation of the activity of carbon in ferrite a_C^α comes from the model proposed by Lacher [12]. The equation has the form:

$$\ln a_C^\alpha = \ln \left[\left(\frac{3 - 4x}{x} \right)^3 \exp \left\{ \frac{4\omega_\alpha}{RT} \right\} \left(\frac{\delta - 3 + 5x}{\delta + 3 - 5x} \right)^4 \right] + \mathrm{C}\{T\}$$

where T is the absolute temperature; R is the ideal gas constant; x is the mole fraction of carbon; $\mathrm{C}\{T\}$ is a function of T; and

$$\delta = \left(12 - 12x + 25x^2 + 12x \exp \left\{ -\frac{\omega_\alpha}{RT} \right\} - 16x^2 \exp \left\{ -\frac{\omega_\alpha}{RT} \right\} \right)^{1/2}$$

where the carbon-carbon interaction energy in ferrite ω_α can be deduced by using the quasi-chemical model [13, 14, 15], to measured data, for example, the results of Lobo and Geiger [16]. It was, in this way, found to be 48570 J mol^{-1} based on the average of the results calculated by Bhadeshia [17].

Because of the very small solubility of carbon in ferrite, the value of the carbon-carbon interaction in ferrite is not reliable. It has been suggested that an alternative way to calculate the carbon-carbon interaction in ferrite is through first principles methods [18, 19].

The equation of the activity of carbon in austenite a_C^γ can be found in the work by Shiflet [20], and it has the form:

$$\ln a_C^\gamma = \ln\left[\left(\frac{1-2x}{x}\right)^5 \left(\frac{\delta-1+3x}{\delta+1-3x}\right)^6\right] + \frac{(\Delta\bar{H}_\gamma - 26800) - T(\Delta\bar{S}_\gamma - 12.29) + 6\omega_\gamma}{RT}$$

where the partial molar heat of solution of carbon in austenite $\Delta\bar{H}_\gamma$ is [16],

$$\Delta\bar{H}_\gamma = 35129 + 169105x \text{ J mol}^{-1}$$

the excess partial molar non-configurational entropy of solution of carbon in austenite $\Delta\bar{S}_\gamma$ is [16],

$$\Delta\bar{S}_\gamma = 7.639 + 120.4x \text{ J mol}^{-1}$$

and

$$\delta = \left(1 + 2x + 9x^2 - 4x\exp\left\{-\frac{\omega_\gamma}{RT}\right\} - 8x^2\exp\left\{-\frac{\omega_\gamma}{RT}\right\}\right)^{1/2}$$

The carbon-carbon interaction energies in austenite ω_γ in terms of the mole fraction of other solutes is obtained empirically (Fig. 2.3) [20, 21, 22].

2.1.3 Carbon diffusivity in austenite

Consider the diffusion of carbon in an austenitic FCC lattice in the direction of [100]. A carbon atom can jump either forward or backward. Diffusion is a measure of average movements. The net flux of carbon J comes from a model due to Siller and McLellan [24, 25, 26]

$$J = -\frac{kT}{h}\exp\left\{-\frac{\Delta G^*}{kT}\right\}\frac{\lambda^2}{3\gamma}$$
$$\left(a_C^\gamma\left[1 + \frac{W(1+x)}{1-(0.5W+1)x+0.5W(0.5W+1)(1-\phi)x^2}\right] + (1+x)\frac{da_C^\gamma}{dx}\right)\frac{\partial x}{\partial z}$$
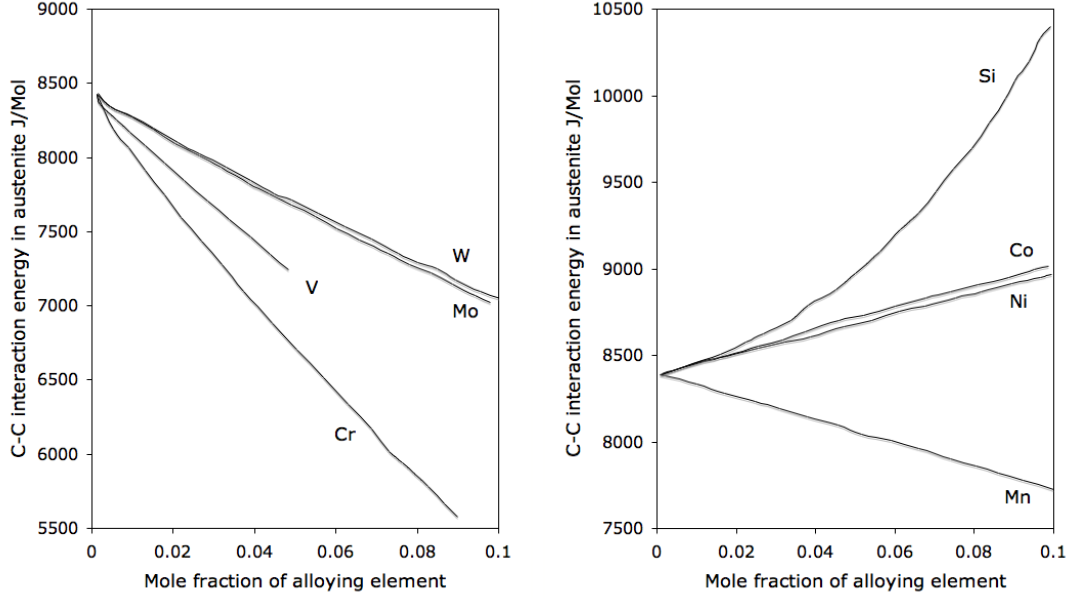
Figure 2.3: Variation of carbon-carbon interaction energy in austenite ω_γ as a function of the concentrations of various alloying elements [23].

where ΔG^* is an activation free energy between neighbouring energy wells; k and h are Boltzmann and Planck constants respectively; λ is the distance between (002) austenite planes; γ is an activity coefficient; W is the number of octahedral interstices around a single such interstice; x is the mole fraction of carbon; z is position in real space; and $\phi = 1 - \exp\left\{-\omega_C^\gamma/kT\right\}$.

Compare this equation with Fick's first law

$$J = -D\frac{\partial x}{\partial z}$$

where D is the carbon diffusivity. Therefore carbon diffusivity in austenite has the form

$$D(x,T) = \frac{kT}{h}\exp\left\{-\frac{\Delta G^*}{kT}\right\}\frac{\lambda^2}{3\gamma}$$
$$\left(a_C^\gamma\left[1 + \frac{W(1+x)}{1 - (0.5W+1)x + 0.5W(0.5W+1)(1-\phi)x^2}\right] + (1+x)\frac{da_C^\gamma}{dx}\right) \quad . \quad (2.1)$$

Through a regression analysis with respect to experimental data, Bhadeshia found [27].

$$\frac{\Delta G^*}{k} = 21230 \text{ K}$$

$$\ln\left\{\frac{\lambda^2}{\gamma}\right\} = -31.84$$

The carbon concentration profile ahead of the moving α/γ interface in austenite follows a trend described by an error function (Fig. 2.4). A weighted average
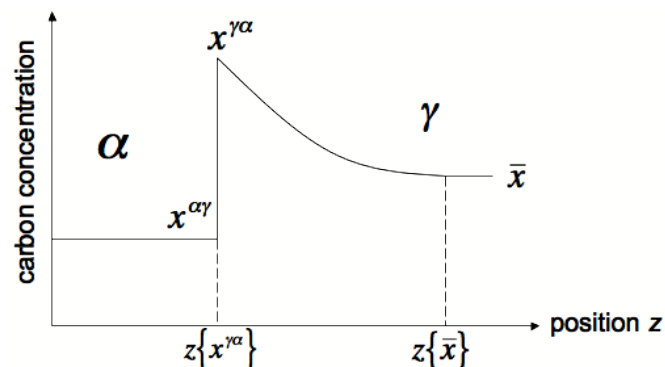
Figure 2.4: The carbon concentration profile around the advancing α/γ interface. Partitioned carbon from ferrite diffuses away from the interface into the austenite. The far field concentration is $\bar{x}$.

diffusivity $\bar{D}$ can adequately represent the effective diffusivity, which is given by integrating D (function of concentration) over the composition range $x^{\gamma\alpha}$ to $\bar{x}$, and then dividing the integral by this range [28].

$$\bar{D} = \int_{x^{\gamma\alpha}}^{\bar{x}} D \frac{dx}{\bar{x} - x^{\gamma\alpha}}$$

2.2 Thermodynamics of Phase Transformations

2.2.1 Chemical potential and the common tangent construction

The Gibbs free energy G was initially called 'available energy' by Josiah Gibbs, who first formulated it. Only if the change in the Gibbs free energy ΔG of a

process is negative, will that process occur spontaneously. A brief introduction of thermodynamics is given here inspired by the book 'Thermodynamics' by Enrico Fermi [29].

The molar Gibbs free energy of a pure substance, e.g., A, is defined as the total Gibbs free energy divided by the total number of moles

$$\underline{G}_A = \frac{G_A}{n_A}$$

Consider two pure substances A and B mixing together to form a solution. The $\Delta\underline{G}$ of the process can be calculated by subtracting the proportional molar Gibbs free energies of the pure substances from the molar Gibbs energy of the solution

$$\Delta\underline{G}\{x_B\} = \underline{G}_{mix}(x_B) - [(1 - x_B)\underline{G}_A + x_B\underline{G}_B]$$

and the equation is illustrated in Fig. 2.5.
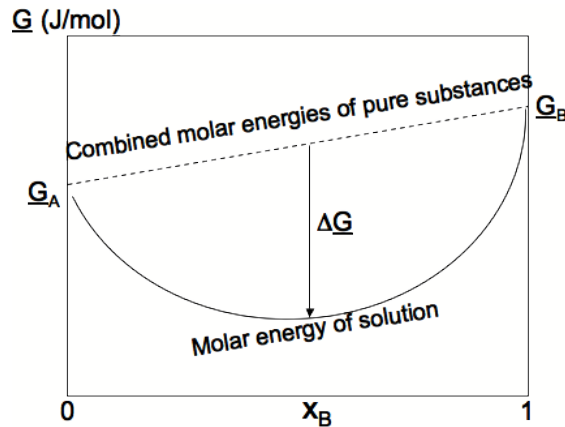
Figure 2.5: $\Delta\underline{G}$ is the reduction of free energy mixing x_B mole pure B and $1 - x_B$ mole pure A. The molar Gibbs free energies of pure substance A and B are $\underline{G}_A$ and $\underline{G}_B$ respectively.

Gibbs free energy is a state function, i.e., it depends only on the current state of the system, not on the way in which the system got to that state. The Gibbs free energy of a solution is a function of temperature T, pressure P and molar

quantities of solutes n_i. The differential form is

$$dG = \left(\frac{\partial G}{\partial T}\right)_{P,n_i} dT + \left(\frac{\partial G}{\partial P}\right)_{T,n_i} dP + \sum_i \left(\frac{\partial G}{\partial n_i}\right)_{T,P,n_{j\neq i}} dn_i \ .$$

If T and P are constant as often are, then

$$dG = \sum_i \left(\frac{\partial G}{\partial n_i}\right)_{T,P,n_{j\neq i}} dn_i \ .$$

Because of the importance of the partial molar quantity $(\frac{\partial G}{\partial n_i})_{T,P,n_{j\neq i}}$, it is designated as chemical potential μ_i. The differential equation is then written

$$dG = \sum_i \mu_i dn_i \ .$$

Written in the molar quantity form, it is

$$d\underline{G} = \mu_A dx_A + \mu_B dx_B \tag{2.2}$$

Furthermore, Gibbs free energy is an extensive quantity, i.e., it is proportional to the size of or the amount of material in the system. For a solution of n_A mole of A and n_B mole of B, the Gibbs energy equals

$$G = \mu_A n_A + \mu_B n_B$$

written in the molar quantity form (divided by $n_A + n_B$),

$$\underline{G} = \mu_A x_A + \mu_B x_B$$

Solving this equation and Eqn. 2.2 ($d\underline{G} = \mu_A dx_A + \mu_B dx_B$) gives the chemical potentials μ_A and μ_B

$$\mu_A = \underline{G} - \frac{d\underline{G}}{dx_B} x_B$$

$$\mu_B = \underline{G} + \frac{d\underline{G}}{dx_B}(1 - x_B)$$

A geometrical representation of these two equations is illustrated in Fig. 2.6. The

29

construct is named the Intercept rule.
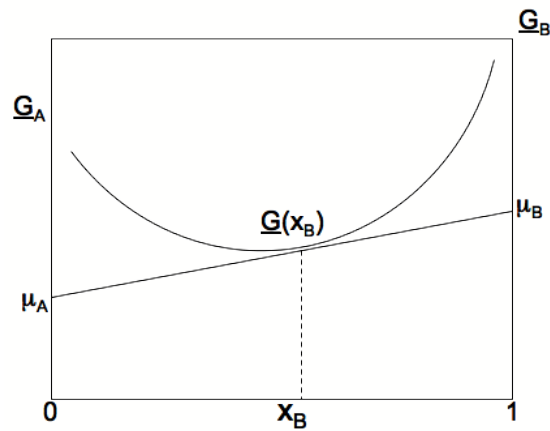
Figure 2.6: A line tangential to the molar free energy curve of a solution of A and B at the mole fraction x_B meets the vertical free energy axes at two points. They are the chemical potential of A and B, μ_A and μ_B respectively.

Consider a solution of A and B with composition $\bar{x}_B$ becoming unstable and decomposing into phase α and phase β (note α in this section is not ferrite). An equilibrium between the two phases requires

$$\mu_A^\alpha = \mu_A^\beta$$

$$\mu_B^\alpha = \mu_B^\beta$$

The geometric interpretation of these two criteria is illustrated in Fig. 2.7. And the construct is named the Common Tangent Method.

2.2.2 Activity

The chemical potential of A can be expressed as the molar Gibbs free energy of pure A plus a term making up the difference
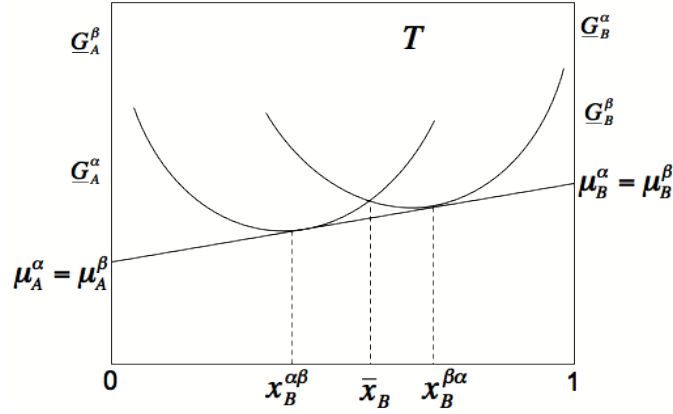
$$\mu_A = \underline{G}_A + RT \ln a_A$$

30

Figure 2.7: At temperature T, a solution of A and B with composition $\bar{x}_B$ decomposes into phase α and β, whose molar free energies are the two curves. The equilibrium between the two phases requires the chemical potentials of A or B in α and β are equal, which determines the composition of phase α and β are $x_B^{\alpha\beta}$, and $x_B^{\beta\alpha}$ respectively.

where the term a_A is called activity. It is related to the concentration x_A by a term called activity coefficient

$$a_A = \gamma_A x_A$$

Activity is the effective concentration of a solute in a solution. In the ideal solution where all the bonds are equivalent, the activity equals the concentration $a_A = x_A$.

2.3 The Driving Forces

All spontaneous transformations in steel are driven by the reduction of Gibbs free energy. This section discusses the driving forces of three different transformation processes.

2.3.1 Driving force of diffusionless transformations

Diffusionless transformation from austenite in steel requires that the molar free energy of ferrite be smaller than that of austenite of the same composition. The driving force for diffusionless nucleation and growth, $\Delta G^{\gamma \to \alpha}$, is given by the vertical distance between the austenite and ferrite curves at the composition of interest

shown in Fig. 2.8.

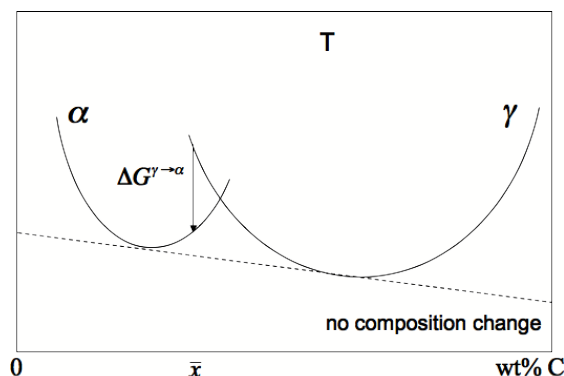
Figure 2.8: In a transformation from austenite to ferrite when there is no composition change, $\Delta G^{\gamma \to \alpha}$ is the free energy reduction for austenite of composition $\bar{x}$.

Alloying elements affect the driving force of transformation. Zener argued that the free energy difference can be factorized into two components, the magnetic $\Delta G_M^{\gamma \to \alpha}$ and non-magnetic terms $\Delta G_{NM}^{\gamma \to \alpha}$ [30]:

$$\Delta G^{\gamma \to \alpha} = \Delta G_M^{\gamma \to \alpha} + \Delta G_{NM}^{\gamma \to \alpha}$$

The non-magnetic component varies approximately linearly with temperature, but the magnetic component varies non-linearly (Fig. 2.9). This division of free energy helps to account for the effects of alloying elements, via a modification of the temperature at which the free energy is evaluated:

$$\Delta G^{\gamma \to \alpha}\{T\} = \Delta G_M^{\gamma \to \alpha}\{T - x\Delta T_M\} + \Delta G_{NM}^{\gamma \to \alpha}\{T - x\Delta T_{NM}\}$$

ΔT_M and ΔT_{NM} are temperature changes due to at. % change of alloying elements. The values used in the model are given in Tab. 2.1.

2.3.2 Driving force for reconstructive transformations

The diffusion of solute in a reconstructive transformation may contradict the intuition that atoms would migrate in the direction of lower concentration. Instead, the diffusion direction is dictated by the tendency to lower the free energy.
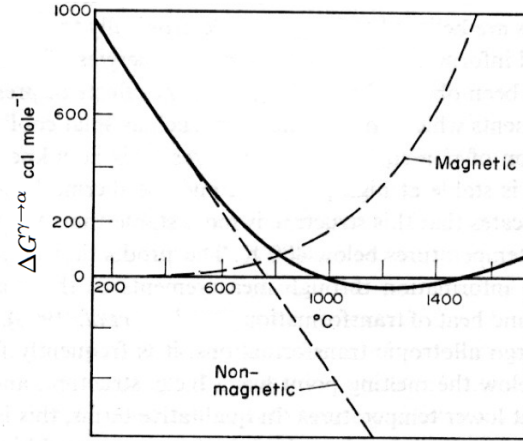
Figure 2.9: Suggested division of the free energy vs. temperature relation for pure iron into magnetic and non-magnetic components (after Zener, 1955 [30]).

Alloying element	ΔT_M / K per at.%	ΔT_{NM} / K per at.%
Si	-3	0
Mn	-37.5	-39.5
Ni	-6	-18
Mo	-26	-17
Cr	-19	-18
V	-44	-32
Co	19.5	16
Al	8	15
Cu	4.5	-11.5

Table 2.1: Values of ΔT_M and ΔT_{NM} for one unit change of alloying elements [31].

In a reconstructive transformation from austenite with carbon concentration $\bar{x}$ at temperature T, ferrite forms at a rate which allows carbon to diffuse into the austenite ahead of the γ/α interface. The migration of carbon crossing the interface is a relatively fast process. Therefore ferrite and austenite are in equilibrium near the interface, where the common tangent method applies (Fig. 2.10)

The driving force of the transformation, $\Delta G^{\gamma \to \gamma' + \alpha}$, is identified on Fig. 2.10. The tangent points on the free energy curves indicate the carbon concentrations of ferrite $x^{\alpha\gamma}$ and enriched austenite $x^{\gamma\alpha}$ respectively, and they are functions of temperature. These compositions can be plotted to form the boundaries on a phase diagram.
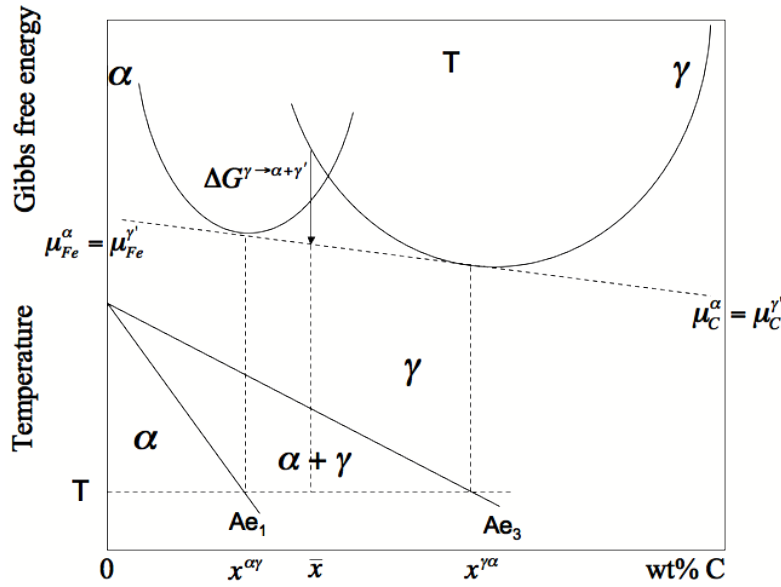
Figure 2.10: The top half shows the free energy change $\Delta G^{\gamma \to \gamma'+\alpha}$ in a reconstructive transformation. Austenite with carbon $\bar{x}$ at temperature T decomposes into ferrite with composition $x^{\alpha\gamma}$ and austenite with composition $x^{\gamma\alpha}$. The elements can be used in the construction of phase diagram.

2.3.3 Maximum driving force for nucleation

The process of nucleation involves fluctuations of atom clusters, called embryos, with different sizes and chemical compositions. Consider embryos materialising in austenite with an initial carbon concentration $\bar{x}$. The quantity of material involved in forming ferrite embryos is so minute that it hardly affects the composition of austenite. Therefore, in the free energy diagram of a reconstructive transformation (Fig. 2.10), the carbon concentration of enriched austenite $x^{\gamma\alpha}$ is close to $\bar{x}$. In the limit, where $x^{\gamma\alpha} = \bar{x}$, the line linking the two concentrations becomes tangential to the austenite free energy curve at $\bar{x}$.

The embryo most likely to survive and develop into a nucleus is the one having the largest reduction in free energy ΔG_m. Geometrically it can be found by drawing a tangent line to the ferrite free energy curve, which is parallel to the line on the austenite curve at $\bar{x}$. This geometric construct is called the parallel tangent method. The tangential line on the ferrite curve also yields the carbon composition of the embryo, x_m^{α} (Fig. 2.11) [32, 33].
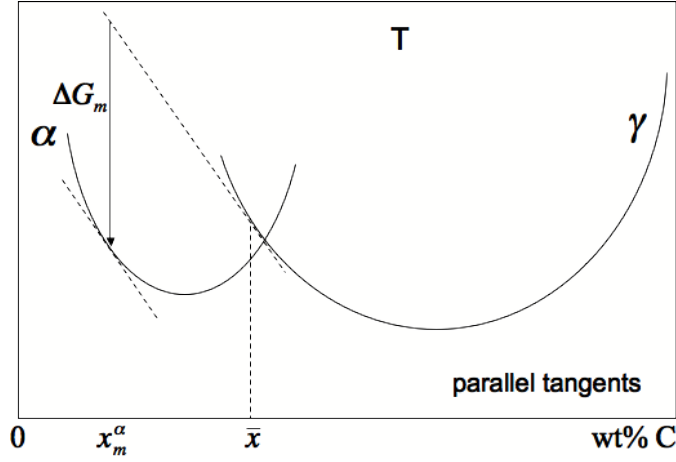
Figure 2.11: An illustration of the parallel tangent method used to find the maximum reduction of Gibbs free energy, ΔG_m forming a embryo that is most likely to survive and develop into a nucleus.

The parallel tangent method can be mathematically formulated, so ΔG_m and x_m^α can be calculated [32]. The equations of the two tangents have the form

$$G^\gamma = (1-x)[G_{Fe}^{o\gamma} + RT \ln a_{Fe}^\gamma(1-\bar{x})] + x[G_C^{o\gamma} + RT \ln a_C^\gamma(\bar{x})]$$

$$G^\alpha = (1-x)[G_{Fe}^{o\alpha} + RT \ln a_{Fe}^\alpha(1-x)] + x[G_C^{o\alpha} + RT \ln a_C^\alpha(x)]$$

where the superscription ^{o} refers to pure substances.

The difference between them gives the free energy change

$$
\begin{aligned}
\Delta G &= G^\alpha - G^\gamma \\
&= (1-x)(G_{Fe}^{o\alpha} - G_{Fe}^{o\gamma}) + x(G_C^{o\alpha} - G_C^{o\gamma}) \\
&\quad + (1-x)RT \ln \frac{a_{Fe}^\alpha(1-x)}{a_{Fe}^\gamma(1-\bar{x})} + xRT \ln \frac{a_C^\alpha(x)}{a_C^\gamma(\bar{x})}
\end{aligned}
\tag{2.3}
$$

As the two tangents are parallel, therefore

$$[G_{Fe}^{o\gamma} + RT \ln a_{Fe}^\gamma(1-\bar{x})] - [G_C^{o\gamma} + RT \ln a_C^\gamma(\bar{x})]$$
$$= [G_{Fe}^{o\alpha} + RT \ln a_{Fe}^\alpha(1-x)] - [G_C^{o\alpha} + RT \ln a_C^\alpha(x)]$$

where the terms are rearranged to have the form

$$(G_{Fe}^{o\alpha} - G_{Fe}^{o\gamma}) - (G_C^{o\alpha} - G_C^{o\gamma}) + RT\ln\frac{a_{Fe}^\alpha(1-x)}{a_{Fe}^\gamma(1-\bar{x})} - RT\ln\frac{a_C^\alpha(x)}{a_C^\gamma(\bar{x})} = 0 \qquad (2.4)$$

Solving Eqn. 2.4 will give the composition x_m of the favourable embryo. Substituting into equation 2.3 yields the maximum molar free energy change of forming a ferrite nucleus ΔG_m

$$\Delta G_m = RT\ln\frac{a_C^\alpha(x_m)}{a_C^\gamma(\bar{x})} \qquad (2.5)$$

Chapter 3

Rates of Transformations

Once the driving forces for transformations have been determined, consequently it is time to formulate the nucleation and growth rates of transformations concerned in this work.

3.1   Nucleation Rates of Phases in Steel

3.1.1   Classical nucleation for allotriomorphic ferrite and pearlite

The outermost layer of atoms on an embryo forms an interface with a relatively higher energy. In the formation of an embryo, there is a gain from materialising the new phase, and a cost in the creation of the interface. The two factors reach balance when embryo passes a critical size and becomes a stable nucleus. Once over this activation energy, the newly formed nucleus carries on with a continuous reduction in free energy.

Suppose there is a homogeneous spherical embryo with radius r (Fig. 3.1). The change of the Gibbs free energy for forming such an embryo is

$$\Delta G = \frac{4}{3}\pi r^3 \epsilon_{\alpha\gamma} + 4\pi r^2 \sigma_{\alpha\gamma} \tag{3.1}$$

where $\epsilon_{\alpha\gamma}$ (J m^{-3}) is the free energy change for materialising the new phase; and $\sigma_{\alpha\gamma}$ (J m^{-2}) is the interfacial energy per unit area.
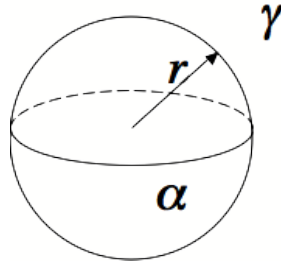
Figure 3.1: A ferrite embryo consisting of a spherical cluster of atoms with radius r enclosed in austenite.

The critical radius r^* can be found by seeking the value of r at which the derivative of ΔG with respect to r equals zero

$$\partial \Delta G / \partial r = 0$$

Substituting r^* back into Eqn. 3.1 gives the activation energy G^*

$$G^* = \frac{16 \pi \sigma_{\alpha\gamma}^3}{3 \epsilon_{\alpha\gamma}^2}$$

It is illustrated in Fig. 3.2

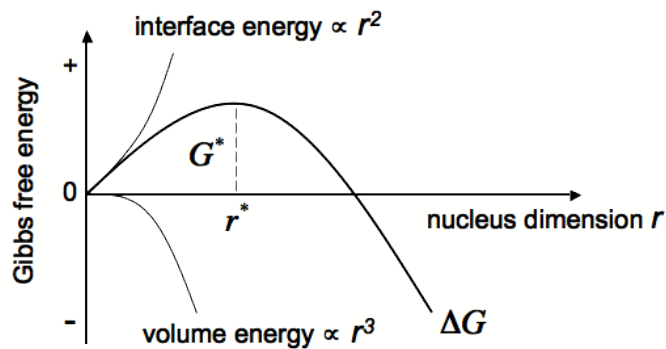Figure 3.2: The trade-off between the gain from forming new phase and loss from creating interface causes an energy barrier, called the activation energy G^*. Embryos with sizes larger than the critical radius r^* are stable and can continuously grow.

This is not how most nuclei are created. Nucleation is far more likely at austenite grain boundaries, which can help reduce the activation energy. This is

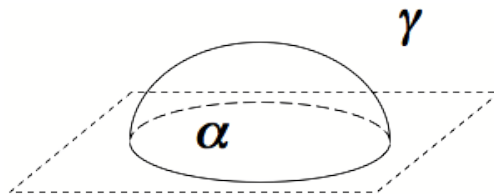termed heterogeneous nucleation (Fig. 3.3). The benefit comes from the partial

Figure 3.3: The nucleation is far more likely to occur on the austenite grain boundaries. The destruction of high energy grain boundary helps reduce G^*.

elimination of the high energy grain boundary. This process, in effect, reduces the activation energy required otherwise in a homogeneous nucleation by a factor related to the shape of the embryo

$$\Delta G^*_{het} = \text{shape} \times \Delta G^*_{hom}$$

The nucleation rate, following classical nucleation theory [34, 35], depends on the attempt frequency ν, the number density of nucleation sites N_v and the probability of successful attempts:

$$I_1^s = N_v \nu \exp\left\{-\frac{\Delta G^*_{het} + Q}{kT}\right\}$$

where Q is the energy barrier for the transfer of an atom across the α/γ interface.

There are many embryos having various sizes and compositions created by random fluctuations. Say Z_n is the number of embryos of n atoms. The distribution of Z_n may be approached slowly in a solid transformation, as there is an activation energy barrier to add or remove an atom. So the above equation as a steady state nucleation rate is inadequate. It is necessary to investigate the time-dependence of the nucleation rate. This has been suggested to have the form [36, 37]:

$$I_1 = I_1^s e^{-\tau/t}$$

where τ is a characteristic time and t is the time elapsed since nucleation started.

$$\tau = \frac{n_c^2 h}{4 a_c kT} \exp\left\{\frac{Q}{RT}\right\}$$

39

where n_c is the number of atoms at the nuclei with critical size and a_c is the number of atoms at the interface of the critical nucleus.

In the present work, the nucleation rate of pearlite and allotriomorphic ferrite is assumed to be related with a constant ratio.

3.1.2 Paraequilibrium nucleation for Widmanstätten ferrite and bainite

It has been demonstrated that Widmanstätten ferrite and bainite do not follow classical nucleation theory involving heterophase fluctuations, but rather the nucleation rate is directly related to the driving force [3], similar to that of martensite [38, 39]. Unlike martensitic nucleation, carbon must be allowed to partition during nucleation. The nucleation rate (m^{-2}) has been suggested to have the form [40, 41, 42].

$$I_2 = K_1 \nu \exp\left\{ -\frac{K_2}{RT}\left(1 + \frac{\Delta G_m}{K_3}\right) \right\}$$

where $\nu = kT/h$ is the attempt frequency factor, $K_1 = 3.049 \times 10^{-2}$ $\mathrm{m}^{-2}\mathrm{s}^{-1}$, $K_2 = 9.481 \times 10^4$ J mol^{-1}, $K_3 = 2540$ J mol^{-1}.

The same nucleus can develop into either Widmanstätten ferrite or bainite on the conditions to be discussed later.

Universal nucleation function

Theoretically time-temperature transformation diagrams consist essentially of two 'C' curves. The lower one has a characteristic flat top and represents the highest temperature, T_h, at which displacive transformation starts. T_h can be either the start temperature of Widmanstätten ferrite or bainite. In a plot of the experimental data of maximum driving force for nucleation G_m versus T_h, the points fall on the same general line (Fig. 3.4) [43, 3].

The general line has been regarded as the universal nucleation function G_N, which expresses the minimum free energy required to obtain a detectable amount of Widmanstätten ferrite or bainite

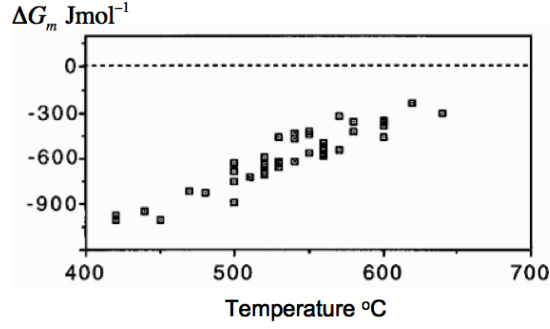$$G_N = 3.637(T - 273.15) + 2540 \text{ J mol}^{-1}$$

Figure 3.4: A plot of the experimental data of the maximum driving force for nucleation G_m versus the T_h. The points fall on the same general line.

where T is the absolute temperature.

Widmanstätten ferrite and bainite start temperature, W_s and B_s

The same nucleus can develop into either a Widmanstätten ferrite particle or a bainite sheaf, depending on the following conditions. To achieve a detectable nucleation rate for both phases, the maximum free energy of para-equilibrium nucleation, ΔG_m, has to be less than the universal nucleation function G_N.

$$\Delta G_m < G_N \tag{3.2}$$

The transformation starts only when there are enough energy for growth. The strain energy stored in the transformation to Widmanstätten ferrite is estimated to be 50 J mol^{-1} [3]. Therefore the condition for the growth of Widmanstätten ferrite is

$$\Delta G^{\gamma \rightarrow \gamma' + \alpha} < -50 \text{ J mol}^{-1} \tag{3.3}$$

Therefore the Widmanstätten ferrite start temperature W_s is where Eqn.3.2 and Eqn. 3.3 are simultaneously satisfied.

The stored energy for bainite has been estimated as 400 J mol^{-1} [3]. The condition for bainite growth is

$$\Delta G^{\gamma \rightarrow \alpha} < -400 \text{ J mol}^{-1} \tag{3.4}$$

The bainite start temperature B_s is where Eqn. 3.2 and Eqn. 3.4 are simultane-

41

ously satisfied.

3.2 Growth Rates of Phases in Steel

3.2.1 Growth for allotriomorphic ferrite and pearlite

Allotriomorphic ferrite

The growth rate of allotriomorphic ferrite is governed by the diffusion of carbon in the austenite ahead of the α/γ interface. The profile of carbon concentration in austenite follows an error function. Although a rigorous solution of error function is used in the work, a simplified model is presented here, which captures the essence of the problem (Fig. 3.5).
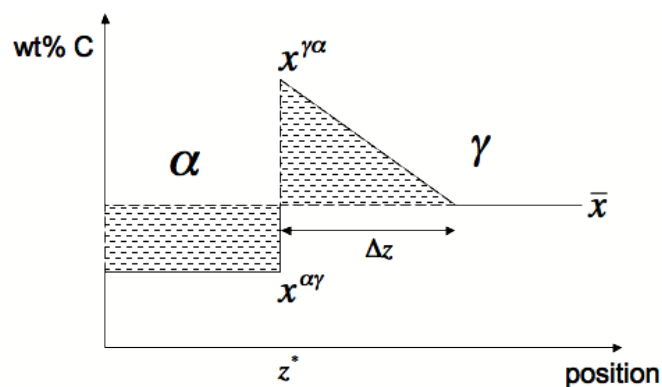
Figure 3.5: A schematic illustration of the carbon concentration profile ahead of a moving α/γ interface, as an allotriomorph grows. The concentration gradient in the austenite is assumed to be constant.

The two shaded areas in Fig. 3.5 must have the same size to ensure the conservation of mass:

$$z^*(\bar{x} - x^{\alpha\gamma}) = \frac{\Delta z}{2}(x^{\gamma\alpha} - \bar{x}) \tag{3.5}$$

Using Fick's first law of diffusion, the rate at which the solute is pushed by the interface must be equal to the rate at which the solute is carried away by the diffusion (Fig. 3.6).

$$\frac{\partial z^*(x^{\gamma\alpha} - x^{\alpha\gamma})}{\partial t} = D\frac{x^{\gamma\alpha} - \bar{x}}{\Delta z} \tag{3.6}$$

Figure 3.6: During a time interval dt, the α/γ interface has moved forward by a distance dz^*.

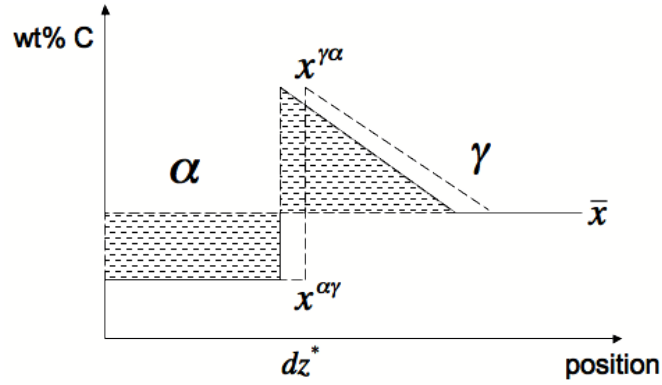where D is the diffusivity of carbon in austenite. Solving Eqns. 3.5 and 3.6 gives

$$z^*\partial z^* = \frac{D(x^{\gamma\alpha} - \bar{x})^2}{2(x^{\gamma\alpha} - x^{\alpha\gamma})(\bar{x} - x^{\alpha\gamma})}\partial t$$

The coefficient part of ∂t in the above equation contains the one-dimensional parabolic thickening rate $\mathcal{H}^\alpha$ of allotriomorphic ferrite. The integral form of z^* in terms of t has the form

$$(z^*)^2 = (\mathcal{H}^\alpha)^2 Dt$$

Which tells that the thickness of an allotriomorph particle has a parabolic relation with time.

Pearlite

A pearlite colony has a lamellar structure of ferrite and cementite. The reaction naturally involves the precipitation of both of the two phases. The difference in carbon concentration of austenite at the vicinity of cementite lamellae, $x^{\gamma\theta}$, and the neighbouring ferrite lamellae, $x^{\gamma\alpha}$, can induce a flux of carbon (Fig. 3.7). The model first analysed by Zener [44] is adopted in this work, though the true mechanism of the growth of a pearlite colony is still under debate.

Consider a growing pearlite colony with the inter-lamellar spacing S_0
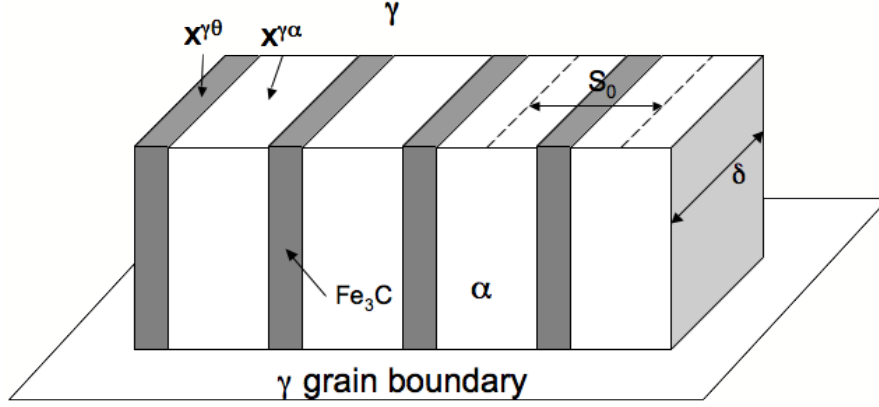
$$S_0 = S_\alpha + S_\theta$$

43

Figure 3.7: A pearlite colony with an interface advancing into austenite in Zener's pearlite growth model. S_0 is the interlamellar spacing, δ is the depth.

where S_α is the thickness of the ferrite lamella; and S_θ is the thickness of the cementite lamella. If growth is allowed to occur by dz in the direction normal to grain boundary, then the volume of austenite transformed per lamellar spacing is $S_0 \delta\ dz\ \rho$, where ρ is the density. The free energy ΔG needed to form this volume of pearlite has the form

$$\Delta G = \Delta H \left(\frac{T_e - T}{T_e} \right) S_0 \delta\ dz\ \rho$$

where T_e is eutectoid temperature, T is the transformation temperature and ΔH is the latent heat of transformation.

The formation of this new volume of pearlite causes an increase in interfacial energy, $E_{\alpha/\theta}$, between new ferrite and cementite interfaces.

$$E_{\alpha/\theta} = 2\sigma_{\alpha/\theta}\delta\ dz$$

where $\sigma_{\alpha/\theta}$ is interfacial energy per unit area.

Growth of lamellae can only occur if the increases in the surface energy is no more than the decrease in free energy due to transformation. Therefore,

$$\Delta H \left(\frac{T_e - T}{T_e} \right) S_0 \rho = 2\sigma_{\alpha/\theta}$$

This is a very simple treatment which neglects any strain energy term. Neverthe-less, the equation predicts the pearlite spacing S_0 decreases with transformation temperature, as is observed experimentally.

Assuming that the diffusion flux equation for carbon in austenite at the vicinity of a pearlite colony follows Fick's first law

$$J = -D\frac{\partial x}{\partial z}$$

Zener proposed an equation of the carbon concentration difference dx over the distance aS_0

$$dx = \left(1 - \frac{S_C}{S_0}\right)(x^{\gamma\alpha} - x^{\gamma\theta})$$

where a is a dimensionless constant; S_C is the critical spacing at which all the driving force is consumed in the construction of interfaces. The values of $x^{\gamma\alpha}$ and $x^{\gamma\theta}$ can be extrapolated from the austenite-ferrite and austenite-cementite phase lines in the phase diagram first proposed by Hultgren [45] (Fig. 3.8).
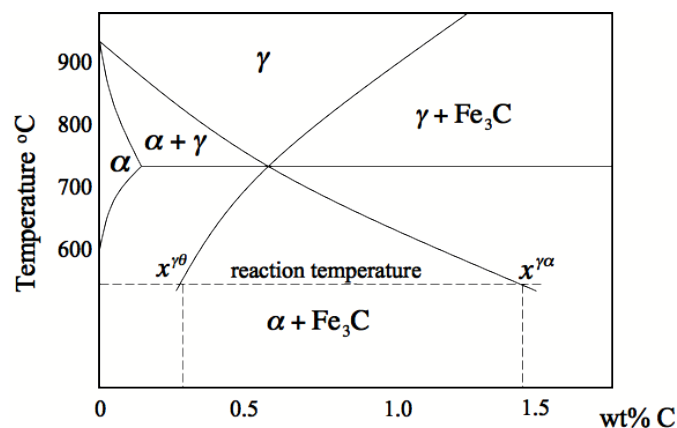

Figure 3.8: The austenite-ferrite and austenite-cementite phase lines in the Fe-C phase diagram are extrapolated to determine the $x^{\gamma\alpha}$ and $x^{\gamma\theta}$ in the non-equilibrim region, as first proposed by Hultgren [45].

Therefore, the diffusion flux equation becomes

$$J = -D\frac{(1 - S_C/S_0)(x^{\gamma\alpha} - x^{\gamma\theta})}{aS_0}$$

On the other hand, the diffusion of carbon results in a planar growth of each lath. The exchange of carbon between newly formed cementite and ferrite is through the flux of carbon

$$J = -\mathcal{H}^P(x^{\theta\gamma} - x^{\alpha\gamma})$$

where $\mathcal{H}^P$ is the growth rate of pearlite in the direction normal to the grain boundary; $x^{\theta\alpha}$ and $x^{\theta\gamma}$ are the carbon concentrations of ferrite and cementite in equilibrium with austenite respectively.

Solving the two equations of J gives the expression for the growth rate of pearlite

$$\mathcal{H}^P = D\frac{1}{aS_0}\left(1 - \frac{S_C}{S_0}\right)\frac{x^{\gamma\alpha} - x^{\gamma\theta}}{x^{\theta\gamma} - x^{\alpha\gamma}}$$

The diffusivity of carbon in austenite can be written in terms of the interface-boundary diffusivity of carbon in austenite D_b and the thickness of interface boundary

$$D = D_b\delta \ .$$

A more sophisticated model developed by Hillert, Cahn and Hagel, Kirkaldy and Lundquist [46] gives

$$\mathcal{H}^P = D_b\delta\frac{S_0^2}{S_\alpha S_\theta}\frac{1}{aS_0}\left(1 - \frac{S_C}{S_0}\right)\frac{x^{\gamma\alpha} - x^{\gamma\theta}}{x^{\theta\gamma} - x^{\alpha\gamma}}$$

3.2.2 Paraequilibrium growth for Widmanstätten ferrite

Unlike allotriomorphic ferrite, the growth rate of a Widmanstätten ferrite plate can be constant, because carbon is partitioned to the side. Many models have been reviewed by Christian [34]. The most comprehensive one was proposed by Trivedi [47]. The plate is assumed to be in the form of a parabolic cylinder and to be constant throughout growth (Fig. 3.9).

The plate lengthening rate $v^{\alpha W}$ at temperature T for steady state growth is obtained by solving the following two equations of supersaturation Ω

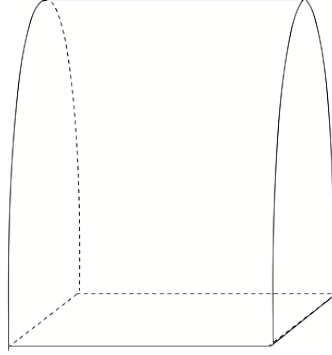$$\Omega = \frac{x^\gamma - \bar{x}}{x^\gamma - x^{\alpha\gamma}}$$

Figure 3.9: A Widmanstätten ferrite particle is modelled as a paraboloid cylinder.

$$\Omega = \pi^{1/2} \exp\{p\} \operatorname{erfc}\{p^{1/2}\} \left(1 + \frac{v^{\alpha w}}{v^{\alpha W}_{\rho=\infty}} \Omega S_1\{p\} + \frac{\rho_c}{\rho} \Omega S_2\{p\} \right)$$

where p is the Péclet number, which is given by

$$p = \frac{v^{\alpha w} \rho}{2 \bar{D}}$$

where $\bar{D}$ is the weighted-average diffusivity of carbon in austenite; ρ is the radius of curvature at the tip of the parabolic cylinder; and ρ_c is the critical radius when growth ceases. The functions $S_1\{p\}$ and $S_2\{p\}$ depend on the Péclet number, and have been evaluated by Trivedi. $v^{\alpha w}_{\rho=\infty}$ is the velocity of a flat interface.

x^γ is the carbon concentration in austenite at the plate tip. It may differ significantly from the equilibrium carbon concentration $x^{\gamma\alpha}$ because of the Gibbs-Thompson capillarity effect. An equation has been given by Christian for finite plate tip radius [34]

$$x^\gamma = x^{\gamma\alpha} \left(1 + \frac{C_{\text{capillary}}}{\rho} \right)$$

where $C_{\text{capillary}}$ is the capillarity constant. The equations indicates that x^γ decreases as interface curvature increase.

Zener proposed that the plate should tend to adopt a tip radius which allows $v^{\alpha w}$ to be maximised. The maximum growth rate $v^{\alpha w}_{\text{max}}$ is obtained when the derivative of the growth rate with respect to ρ equals zero

$$\frac{\partial v^{\alpha w}}{\partial \rho} = 0 \ .$$

This maximum lengthening rate is used as the growth rate for Widmanstätten ferrite $\mathcal{H}^{\alpha_W}$ in this work, though there is lack of experimental evidence to support this hypothesis

$$\mathcal{H}^{\alpha_W} = v_{\max}^{\alpha_W}$$

3.2.3 The growth of bainite and the T_0' condition

Oblak & Hehemann [48] first suggested that the bainite growth proceeds in a step-wise manner, that new platelets or sub-units nucleate on the tips of existing sub-units and each individual sub-unit grows without diffusion (Fig. 3.10). The details have been reviewed by Hehemann [49]. The first theory based on this mechanism emerged in 1982 by Bhadeshia [40]
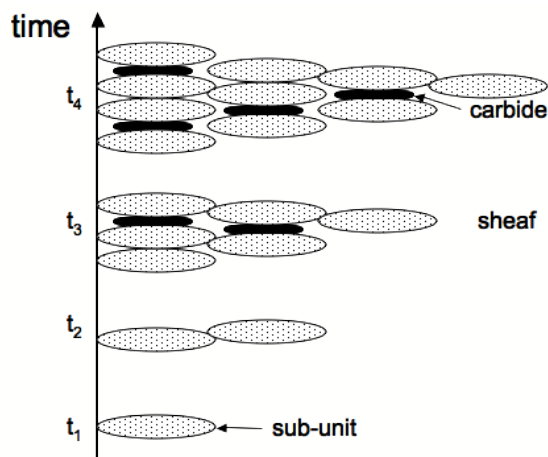
Figure 3.10: Schematic illustration of a growing bainite sheaf over time in a step-wise manner. A sheaf grows by the propagation of tiny thin plates, called sub-units, which successively nucleate on the tip of previous sub-units.

The rate of the successive nucleation of sub-units I_s can be described in the same manner as the nucleation rate for a displacive transformation [50, 41]

$$I_s = K_4' \nu \exp\left\{-\frac{K_5}{RT}\left(1 + \frac{\Delta G_m}{K_3}\right)\right\}$$

The time interval between two successive sub-unit is

$$\Delta t_s = \frac{1}{I_s} = \frac{K_4}{\nu} \exp\left\{ \frac{K_5}{RT} \left(1 + \frac{\Delta G_m}{K_3} \right) \right\}$$

where K_3 is 2540 J mol^{-1}; K_4 is 1.663×10^{13} J mol^{-1}; and K_5 is 6.233×10^4 J mol^{-1}.

T$'_0$ Mechanism

At temperature T, diffusionless transformation requires that the carbon concentration is below x_{T_0}, where

$$\Delta G^{\gamma \to \alpha} = 0 \text{ J mol}^{-1}$$

at x_{T_0}. The points x_{T_0} fall on a line called the T_0 curve (Fig. 3.11).
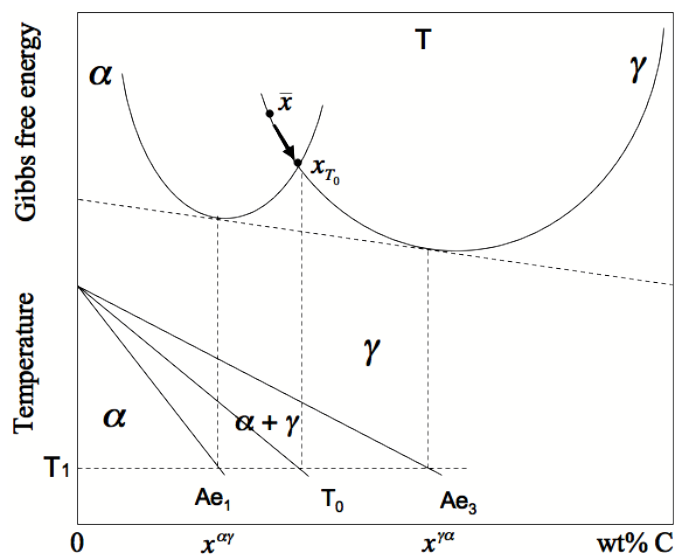
Figure 3.11: Schematic illustration of the T_0 construction on the Fe-C phase diagram. Diffusionless transformation of a sub-unit occurs when the carbon concentration in the austenite lies to the left of the T_0 boundary.

Suppose in an isothermal transformation that a bainite plate forms without diffusion from austenite with initial carbon concentration $\bar{x}$, and any excessive carbon is soon afterwards rejected into the residual austenite. The next sub-unit has to grow from carbon-enriched austenite. This process must cease when the

austenite carbon concentration reaches x_{T_0}, corresponding to the T_0 curve (Fig. 3.12).
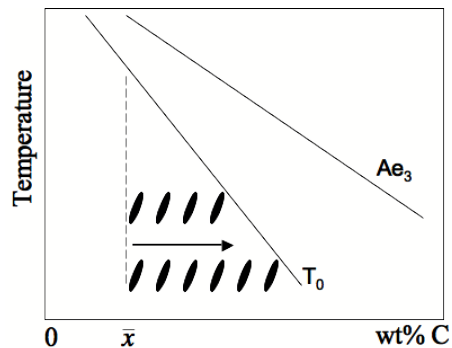
Figure 3.12: In an isothermal transformation, sub-units are created from carbon-enriched austenite until the carbon composition in the austenite eventually reaches the T_0 boundary, where diffusionless transformation becomes impossible.

Taking into account the stored energy 400 J mol^{-1}, the diffusionless transformation under the new condition requires

$$\Delta G^{\gamma \to \alpha} < -400 \text{ J mol}^{-1} \ .$$

This moves the T_0 curve to a new position in phase diagram designated T$_0'$ (Fig. 3.13). The T$_0'$ mechanism sets a limit on the volume fraction of bainite $V_{\alpha_B}^{\text{max}}$ at any temperature

$$V_{\alpha_B}^{\text{max}} \simeq \frac{x_{T_0'} - \bar{x}}{x_{T_0'} - x^{\alpha \gamma}} \tag{3.7}$$

where $x_{T_0'}$ is the carbon concentration corresponding to the T_0'.

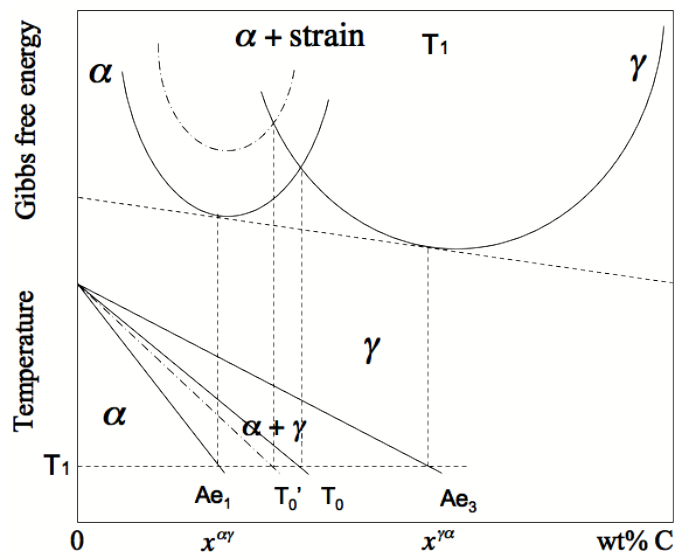Figure 3.13: A schematic illustration of the T_0' construct which takes strain energy into consideration. In an isothermal transformation at temperature T, bainite sub-units are formed in carbon-enriched austenite until the carbon composition in austenite reaches the T_0' boundary.

Chapter 4

Modelling Simultaneous Transformations

Once the nucleation and growth rates are established, it is time to deal with overall transformation kinetics. There are a few simplifications in the scheme. First it is assumed that the chemical composition, temperature, grain size and the microstructure are homogeneous. Therefore the model does not represent the entire body of a bulk, real material, which may have compositional segregation, temperature gradients, and changes in the austenite grain size from the surface to the core. Second the growth rate of any phase applies to all its particles, whether it has existed for some period or has just been nucleated. This simplification deviates from reality, as the local environment of any particle may be different. Finally, in the numerical scheme, the particles of any phase nucleated in the same time interval are identical. So they are grouped by their nucleation time.

4.1 General Kinetic Model

Hard-impingement between particles growing from different locations can be implemented using Avrami theory [51, 52, 53, 54]. Further approximations are necessary to account for the soft impingement in bainite transformation, such as the assumption of a mean field, which describes the overlap of diffusion fields from distant particles.

4.1.1 Avrami model

Referring to Fig. 4.1, suppose that two particles exist at a time t; a small interval Δt later, new regions marked a, b, c and d are formed assuming that they are able to grow unrestricted whether or not the region into which they grow is already transformed. This is the concept of extended space. However, only those components of a, c and d which lie in previously untransformed matrix can contribute to a change in the real volume of the product phase (α).
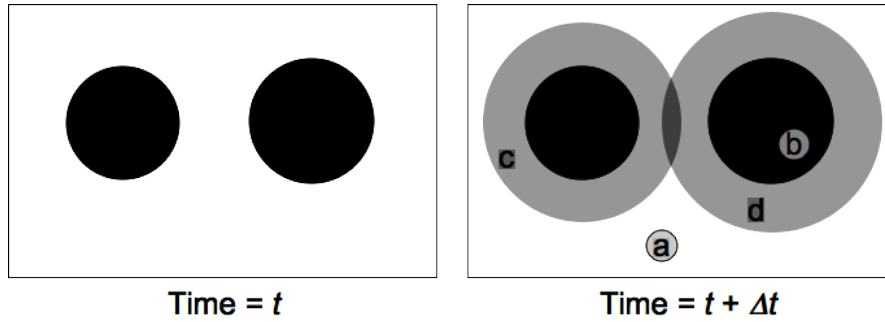

Figure 4.1: Concept of extended volume. New regions c and d are formed in the interval Δt as the original particles grow, and new particles a and b nucleate. However, not all of the new regions are real.

The way to remove the impossible growth is to multiply the change in extended volume dV_e^α by the probability of finding untransformed regions. This has the effect of excluding regions such as b in the Fig. 4.1, which clearly cannot contribute to the real change in volume of the product:

$$dV^\alpha = \left(1 - \frac{V^\alpha}{V}\right) dV_e^\alpha$$

where the subscript e refers to extended space; V^α is the volume of α and V is the total volume. It is assumed that the microstructure develops at random. For such a random distribution of precipitated particles, this equation can easily be integrated to obtain the real volume fraction

$$\frac{V^\alpha}{V} = 1 - \exp\left\{-\frac{V_e^\alpha}{V}\right\}$$

The extended volume V_e^α is straightforward to calculate using nucleation and growth models since it neglects completely any impingement effects.

Multiple reactions occurring simultaneously can be accounted for by forming coupled equations [55, 56, 57, 36, 37]. Thus for two phases α and β

$$dV^\alpha = \left(1 - \frac{V^\alpha + V^\beta}{V}\right) dV_e^\alpha$$

$$dV^\beta = \left(1 - \frac{V^\alpha + V^\beta}{V}\right) dV_e^\beta$$

This can be done for any number of simultaneous reactions. Although analytical solutions for simultaneous equations exist for trivial cases, they must in general be solved numerically, which in fact has the advantage of permitting the boundary condition to change as transformation progresses.

4.1.2   Numerical scheme

The nucleation and growth rate of any transformation product may change as the composition of austenite and the temperature change. To model the gradual development of microstructure, the calculation is divided into time steps. The size of the time step may affect the accuracy of the calculation, if the value chosen is not small enough.

The number of particles of phase i nucleated at time interval k is the product of nucleation rate $I_{i,k}$ $(\mathrm{m}^{-2}\mathrm{s}^{-1})$, the size of time interval Δt and the total volume V. The change of extended volume of these particles at the current time step n is

$$\Delta V_{i,k}^e = I_{i,k} V \Delta t \times \mathcal{V}_{i,n} \Delta t$$

where $\mathcal{V}_{i,n}$ is the growth rate of phase i at the current time interval n.

The change in the extended volume of all the particles of phase i at the current time step is

$$\Delta V_i^e = \sum_k (I_{i,k} V \Delta t)(\mathcal{V}_{i,n} \Delta t) \ .$$

The real change of volume in the current time interval is then

$$\Delta V_i = \left(1 - \frac{\sum_i V_i}{V}\right) \Delta V_i^e \quad (4.1)$$

where $\sum_i V_i$ sums the total transformed volume of all phases and V is the total volume of the entire system. Finally this volume change is updated to the real volume of phase i at the current time

$$V_{i,n} = V_{i,n-1} + \Delta V_i \ .$$

4.1.3 Grain boundary nucleated reactions

Since many reactions are nucleated at austenite grain boundaries rather than at random locations, an adaptation to the extended space concept proposed by Cahn [2] is used to deal with such reactions. Impingement then occurs in two forms, along the grain boundary plane (dealt with the extended area concept) and between particles originating from different boundaries [36, 37].

Consider a system of several phases with total area of austenite grain boundaries O_B, which is a constant. It can be estimated using the stereological relation that [58]

$$O_B = \frac{2}{\bar{L}}$$

where $\bar{L}$ is the mean linear intercept for an equiaxed grain structure (Fig. 4.2).

The model continuously tracks the volume fraction of any phase. The shape of any phase are simplified to be constant throughout simulation, and it is fixed by ratios of geometric parameters. Particles of any phase are grouped by nucleation times, as particles nucleated at the same time interval are identical (Fig. 4.3).

A growing particle penetrates imaginary planes parallel to the grain boundary (Fig. 4.4). On parallel plane y (y is the distance of the plane from the boundary), new regions of transformation occur randomly. But not all regions contribute to the new growth, as some are on the transformed area. An adaptation to the extended volume concept is used to remove the regions in which transformation is impossible.

Consider the change of extended area of phase i on plane y, $\Delta O_{i,y}^e$. It is
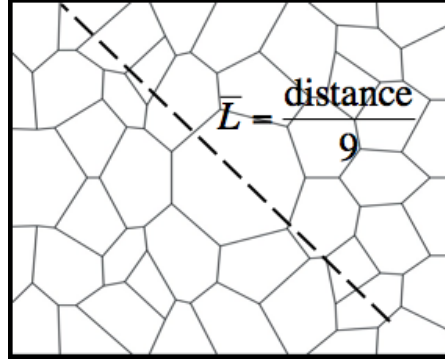
Figure 4.2: The mean linear intercept, $\bar{L}$, is obtained by dividing the length of the intercept line by the number of grain boundaries it crosses. The number is the number of grains crossed by the line. A statistically significant number of measurements must be made depending on the desired level of accuracy.
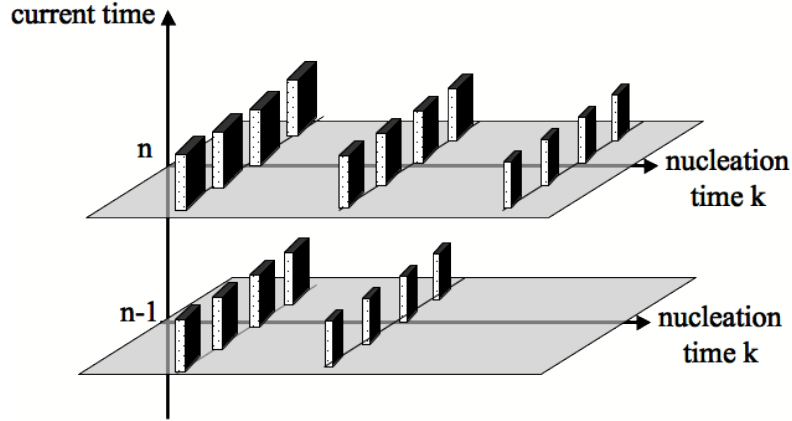

Figure 4.3: Particles of any phase are organised according to their nucleation time. The shape of any particle are simplified as constant by fixed ratios of geometric parameters. New particles are added into the system by nucleation.

obtained by adding the contributions of particles that have just reached and have penetrated plane y

$$\Delta O^e_{i,y} = \sum_k (I_{i,k} \Delta t O_B)(\mathcal{O}_{i,n,y} \Delta t) \tag{4.2}$$

where $\mathcal{O}_{i,n,y}$ is the growth rate of area at current time n (m^{2}s^{-1}). The real-area change at current time step is obtained by multiplying $\Delta O^e_{i,y}$ with the proportion
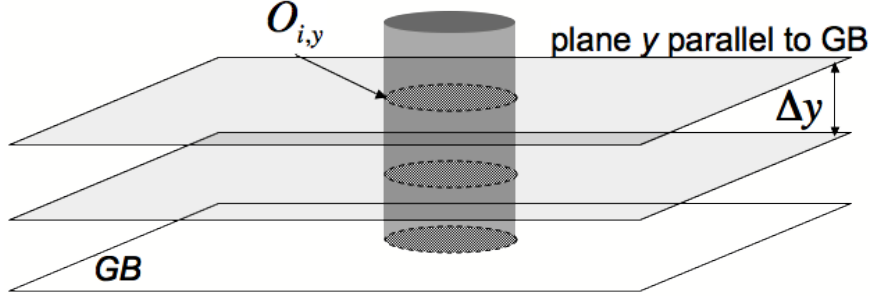
56

Figure 4.4: The area of phase i on a imaginary plane y parallel to the grain boundary (GB) (y is the distance of the plane from the boundary) is $O_{i,y}$. Δy is the distance between two adjacent planes, which was set as $\Delta y = 0.1$ μm in the work.

of total untransformed area on plane y

$$\Delta O_{i,y} = \left(1 - \frac{\sum_i O_{i,y}}{O_B}\right) \Delta O_{i,y}^e \tag{4.3}$$

where $\sum_i O_{i,y}$ sums all phases. The total area of phase i on plane y then is updated

$$O_{i,y,n} = O_{i,y,n-1} + \Delta O_{i,y}$$

The extended volume of phase i at current time step can be calculated by

$$V_{i,n}^e = \Delta y \sum_y O_{i,y,n} \tag{4.4}$$

where Δy is the distance between adjacent parallel planes. The extended volume change of phase i at current time step is

$$\Delta V_i^e = V_{i,n}^e - V_{i,n-1}^e$$

On combining with Eqn. 4.1, the change of real volume of phase i is

$$\Delta V_i = \left(1 - \frac{\sum_i V_i}{V}\right) \Delta V_i^e$$

57

Finally, the total volume of phase i at time n is

$$V_{i,n} = V_{i,n-1} + \Delta V_i$$

4.2 Kinetic Models of Individual Phases

The numerical Avrami scheme has provided the template for the treatment of any of the phases concerned.

4.2.1 Allotriomorphic ferrite

Allotriomorphic ferrite particles are modelled as thin discs forming on the grain boundary with aspect ratio $\eta^\alpha = 3$, i.e., the ratio of radius to half the height [59]. Because the ferrite forms by reconstructive transformation, an allotriomorph particle can cross the grain boundary and continue its growth into the adjacent grain [60, 35] (Fig. 4.5).
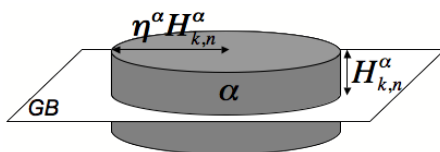

Figure 4.5: Model of an allotriomorphic particle

It is assumed that the growth of any allotriomorph on either side of the boundary is symmetric, so the following calculation concerns only half of the particle. The half-thickness in the direction normal to the grain boundary, H^α, has been shown that it has a parabolic relation with time

$$H_\tau^\alpha(t) = \mathcal{H}^\alpha \bar{D}^{1/2}(t - \tau)^{1/2}$$

where τ is the nucleation time of the particle; t is the current time; $\mathcal{H}^\alpha$ is the one-dimensional parabolic thickening rate; and $\bar{D}$ is the weight-averaged diffusivity of the carbon in austenite. The differentiation of this function with respect to time is

$$dH_\tau^\alpha(t) = \frac{1}{2}\mathcal{H}^\alpha \bar{D}^{1/2}(t - \tau)^{-1/2}dt \ .$$

In the language of numerical calculations, the change in the half-thickness of an allotriomorph nucleated at time k, at the current time step n is

$$\Delta H_k^\alpha = \frac{1}{2}\mathcal{H}^\alpha \bar{D}^{1/2}(n\Delta t - k\Delta t)^{-1/2}\Delta t$$

A small modification is needed to this equation for an allotriomorph just nucleated

$$\Delta H_k^\alpha = \mathcal{H}^\alpha \bar{D}^{1/2}\Delta t^{1/2} \ .$$

The change of half-thickness is then added to the half-thickness at previous time to yield that at the current time

$$H_{k,n}^\alpha = H_{k,n}^\alpha + \Delta H_k^\alpha$$

The information of the half-thickness of a particle gives a measure of whether the particle has reached the parallel plane under concern. Using Eqn. 4.2, the extended area of a particle nucleated at k on plane y has the form

$$\Delta O_{k,y}^{\alpha,e} = I_k^\alpha \Delta t O_B \times \mathcal{O}_{n,y}^\alpha \Delta t \tag{4.5}$$

where $\mathcal{O}_{n,y}^\alpha$ is the growth rate of intersection area at time n. As shown later, the value of $\mathcal{O}_{n,y}^\alpha$ is a function of $\mathcal{H}^\alpha$ and $\eta^\alpha = 3$.

The equation of the change of extended area of those particles nucleated at k on plane y depends the position of the plane. The particle has just reached the plane, when $H_{k,n}^\alpha = y$; has exceeded the plane, when $H_{k,n}^\alpha > y$ and is below the plane, when $H_{k,n}^\alpha < y$

$$\Delta O_{k,y}^{\alpha,e} = \begin{cases} I_k^\alpha \Delta t O_B \times \pi(\eta^\alpha H_{k,n}^\alpha)^2 & H_{k,n}^\alpha = y \\[2mm] I_k^\alpha \Delta t O_B \times \pi(\eta^\alpha \mathcal{H}^\alpha \bar{D}^{1/2}\Delta t^{1/2})^2 & H_{k,n}^\alpha > y \\[2mm] 0 & H_{k,n}^\alpha < y \end{cases}$$

where the product $\eta^\alpha H_{k,n}^\alpha$ gives the radius of an allotriomorph disc. And the

extended area of all allotriomorph particles on plane y is

$$\Delta O_y^{\alpha,e} = \sum_k \Delta O_{k,y}^{\alpha,e} \ .$$

Substituting the value of $\Delta O_y^{\alpha,e}$ into the equations in section 4.1.3 returns the volume fraction of allotriomorphic ferrite at the current time. Because only half the particle has been modelled here, the total volume is, by symmetry, twice as much.

4.2.2 Pearlite

The shape of a pearlite colony is taken to be that of a cylinder with a fixed aspect ratio $\eta^P = 1$, i.e., the ratio of radius to half the height. The shape is maintained, as the particle grows proportionally in all directions. Like allotriomorphic ferrite, pearlite also grows by reconstructive transformation, and hence can propagate across austenite grain boundaries (Fig. 4.6).
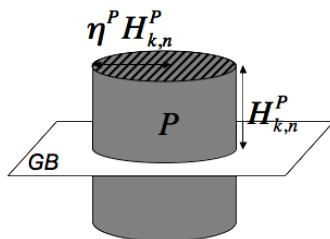
Figure 4.6: Model of a pearlite colony.

The half-thickness of a colony H^P nucleated at time τ has a linear relation with time

$$H_\tau^P(t) = \mathcal{H}^P(t - \tau)$$

where $\mathcal{H}^P$ is the growth rate in the direction normal to grain boundaries. As shown later, the growth rate of the diameter of cylinder is a function of $\mathcal{H}^P$ and η^P. The corresponding numerical equation is

$$\Delta H^P = \mathcal{H}^P \Delta t$$

As pearlite can nucleate on ferrite as well as cementite, a new pearlite nucleus can form on top of layers of transformed material accumulated on grain boundaries. The distance from the boundary of a pearlite nucleus has to include the average thickness of all the transformed material

$$\Delta H^P = \mathcal{H}^P \Delta t + \sum_i V_i^e / O_B \ .$$

The change of extended area of those pearlite particles nucleated at k on plane y is one of the following equations on three exclusive conditions

$$\Delta O_{k,y}^{P,e} = \begin{cases} I_k^P \Delta t O_B \times \pi [\eta^P (H_{k,n}^P - \sum_i V_i^e / O_B)]^2 & H_{k,n}^P = y \\\\ I_k^P \Delta t O_B \times 2\pi (\eta^P)^2 [\mathcal{H}^P (n\Delta t - k\Delta t)] \mathcal{H}^P \Delta t & H_{k,n}^P > y \\\\ 0 & H_{k,n}^P < y \end{cases}$$

For the case $H_{k,n}^P > y$, the term with higher power of Δt is omitted. Because only half of the height of any colony is modelled, the equation of extended volume needs to be multiplied by 2

$$V^{P,e} = 2\Delta y \sum_y O_y^P \ .$$

4.2.3   Widmanstätten ferrite

The thin plates of Widmanstätten ferrite are modelled as tetragonal shape of dimension $a = b \neq c$ with aspect ratio $\eta^{\alpha w} = 0.05$, i.e., the ratio of thickness to length. [61]. Because Widmanstätten ferrite is a displacive transformation, the plates are confined to the single grain in which it has nucleated (Fig. 4.7). The change of thickness in the direction normal to the grain boundary at a time interval is given by

$$\Delta H^{\alpha w} = \mathcal{H}^{\alpha w} \Delta t$$

where $\mathcal{H}^{\alpha w}$ is the plate lengthening rate. Because Widmanstätten ferrite nucleates on both the grain boundary and existing allotriomorphic ferrite, the distance
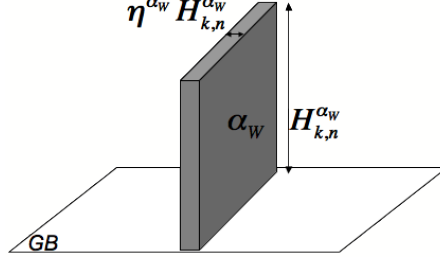
Figure 4.7: Model of a Widmanstätten plate.

of a newly nucleated Widmanstätten ferrite particle has to include the average thickness of the material that has already cumulated on the grain boundary

$$\Delta H^{\alpha_W} = \mathcal{H}^{\alpha_W} \Delta t + \sum_i V_i^e / O_B$$

The change of extended area of those particles nucleated at time k on the plane y is given by one of three exclusive conditions

$$\Delta O_{k,y}^{\alpha_W,e} = \begin{cases} I_k^{\alpha_W} \Delta t O_B \times \eta^{\alpha_W} (H_k^{\alpha_W} - \sum_i V_i^e / O_B)^2 & H_{k,n}^{\alpha_W} = y \\[2mm] I_k^{\alpha_W} \Delta t O_B \times 2\eta^{\alpha_W} \mathcal{H}^{\alpha_W} (n\Delta t - k\Delta t) \mathcal{H}^{\alpha_W} \Delta t & H_{k,n}^{\alpha_W} > y \\[2mm] 0 & H_{k,n}^{\alpha_W} < y \end{cases}$$

where the high power term of Δt is omitted. Combining it with the equations in section 4.1.3 yields the volume fraction of Widmanstätten ferrite.

4.2.4 Bainite

A bainite sheaf is made up of many tiny sub-units. They are nucleated on the tips of previous sub-units. The growing of a sub-unit is a process much faster than the time lapse to nucleate the next sub-unit. Therefore, the growth rate of a bainite sheaf is determined by the nucleation rate of sub-units. Bainite sheaves are modelled as plates. They are confined to grow in one of the grains at a boundary due to a displacive transformation mechanism (Fig. 4.8) [62, 63].

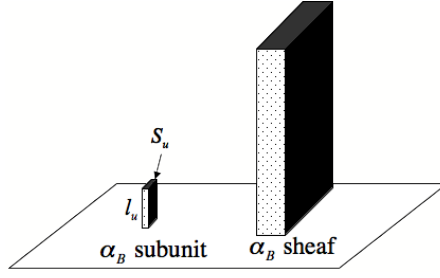As sub-units nucleate and attach themselves on both sides and the top of a

Figure 4.8: Model of a bainite sub-unit and sheaf.
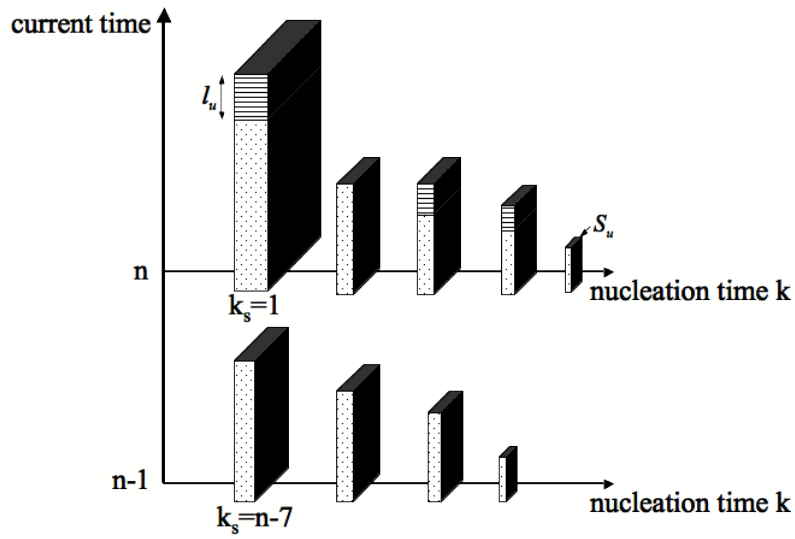
sheaf, it grows in all dimensions (Fig. 4.9) [50].

Figure 4.9: The evolution of bainite sheaves is in a discontinuous fashion. The condition for further growth is the comparison between the time lapsed since the last nucleation and the required incubation time at the current time.

The incubation time required to nucleate the next sub-unite Δt_s is

$$\Delta t_s = \frac{1}{I_s} = \frac{C_4^{\alpha_B}}{\nu} \exp\left\{ \frac{C_5^{\alpha_B}}{RT} \left(1 + \frac{\Delta G_m}{C_3^{\alpha_B}} \right) \right\}$$

where $C_4^{\alpha_B} = 1.663 \times 10^{13}$ J mol^{-1}, $C_5^{\alpha_B} = 6.233 \times 10^4$ J mol^{-1} [50].

The empirical equations of the length and intersection area of a sub-unit are

[59]:

$$l_u = \begin{cases} 10.0 \times 10^{-6}(\frac{T-528}{150}) & T > 528 \\ 1.0 \times 10^{-7} & T \leq 528 \end{cases}$$

$$S_u = \begin{cases} 2.0 \times 10^{-12}(\frac{T-528}{150})^2 & T > 528 \\ 2.0 \times 10^{-16} & T \leq 528 \end{cases}$$

These equations are based on experimental data by Chang and Bhadeshia for steels containing 0.095-0.5 wt % C, transformed isothermally between 523 and 773 K [64].

For particles which had the last sub-unit added at time interval k_s ($k \leq k_s \leq n$), if the time elapsed to the current time ($n\Delta t - k_s\Delta t$) is greater then Δt_s, a new sub-unit can then be added. On the other hand, if the time elapse is shorter, then the sheaf is not permitted to grow at the current time. The change of the height of a single bainite sheaf is

$$\Delta H_{k,n}^{\alpha_B} = \begin{cases} l_u & (n\Delta t - k_s\Delta t) \geq \Delta t_s \\ \\ 0 & (n\Delta t - k_s\Delta t) < \Delta t_s \end{cases}$$

A similar treatment for the change of extended area of a single bainite sheaf nucleated at k on plane y is given by

$$\Delta O_{k,y}^{sf,e} = \begin{cases} S_u & k_s = k + 1 \\ \\ \theta S_u & (n\Delta t - k_s\Delta t) \geq \Delta t_s \\ \\ 0 & (n\Delta t - k_s\Delta t) < \Delta t_s \end{cases}$$

where in the case $k_s = k + 1$, a sheaf has just nucleated; The constant θ is chosen to be 2, for preserving the shape of the sheaf.

The change of intersection area of all the sheaves nucleated at the same time

k on plane y is given by

$$\Delta O_{k,y}^{\alpha_B,e} = \begin{cases} I_k^{\alpha_B} \Delta t O_B \times \Delta O_{k,y}^{sf,e} & H_{k,n}^{\alpha_B} \geq y \\ \\ 0 & H_{k,n}^{\alpha_B} < y \end{cases}$$

The change for all sheaves is then

$$\Delta O_y^{\alpha_B,e} = \sum_k \Delta O_{k,y}^{\alpha_B,e} \ .$$

For the T_0' mechanism, the volume fraction of bainite cannot exceed $V_{\alpha_B}^{\max}$. To implement this mechanism, instead of using Eqn. 4.1, for bainite, the volume Avrami method has the form

$$\Delta V_B = \left(1 - \frac{V_B}{V_{\alpha_B}^{\max}}\right) \Delta V_B^e \ .$$

Chapter 5

Validation of the Model: the Trends

The model based on the theories discussed in the previous chapters has been validated by various methods. Before we can compare the model against experimental data, it is necessary to validate separately the model on the factors that can affect the microstructure of steels, so to assure that known physical phenomena are repeated. Some simple systems are selected for the purpose. Any variable under test was altered systematically over a series of calculations, and the resulting trends were examined.

5.1 The Effect of Carbon

To have a clean examination on carbon, a series of binary Fe-C systems were used with carbon concentration ranging from 0.1 wt % to 0.7 wt % (Tab. 5.1). The

Carbon (wt %)	0.1	0.2	0.3	0.4	0.5	0.6	0.7

Table 5.1: Carbon concentrations of the binary Fe-C steels used in the study on the effect of carbon.

reason that hypereutectoid steels (carbon $\geq$ 0.8 wt %) were not included, was because proeutectoid cementite would be produced firstly in a continuous cooling transformation of a hypereutectoid steel and the model at the current status does

not include the mechanism of forming proeutectoid cementite.

As shown later, cooling rate can greatly affect the transformation. A slow cooling rate 0.05 °C s^{-1} was used and the austenite grain size was set as 30 μm. The same inputs were applied to all the transformations considered. The time step of any calculation was set in a way that the size of the time steps was small enough to affect the predicted volume fraction by less than 0.002. This adjustment procedure was performed before every calculation demonstrated in the thesis. The predicted microstructures are listed on Tab. 5.2. As the carbon concentration moves from 0.1 to 0.7 wt %, the transformation start temperature declines and more pearlite is predicted to form. Pearlite is a fast reaction in the model.

C wt %	α	P	α_W	α_B	Time / s
0.1	0.90	0.10	0.000	0.000	3714
0.2	0.77	0.23	0.000	0.000	3036
0.3	0.64	0.36	0.000	0.000	2574
0.4	0.54	0.46	0.000	0.000	2298
0.5	0.45	0.55	0.000	0.000	2058
0.6	0.36	0.64	0.000	0.000	1794
0.7	0.14	0.86	0.000	0.000	1074

Table 5.2: The predicted volume fractions of allotriomorphic ferrite (α), pearlite (P), Widmanstätten ferrite (α_W) and bainite (α_B), and transformation finishing time. The data are plotted in Fig. 5.1

All the transformations are completed with no austenite left. The pearlite content steadily increases with rising carbon concentration. The transformation start temperature decreases with increasing carbon.

For more detailed analysis, diagrams of volume fraction vs. temperature were produced. Such a diagram first appeared in the paper by Jones and Bhadeshia [37]. Comparing the diagrams of 0.1 wt % carbon and 0.7 wt % carbon, allotriomorphic ferrite forms much earlier, before pearlite, in the steel having 0.1 wt % carbon. This is expected, as pearlite can only grow once the untransformed austenite is adequately enriched with carbon (Fig. 5.2).
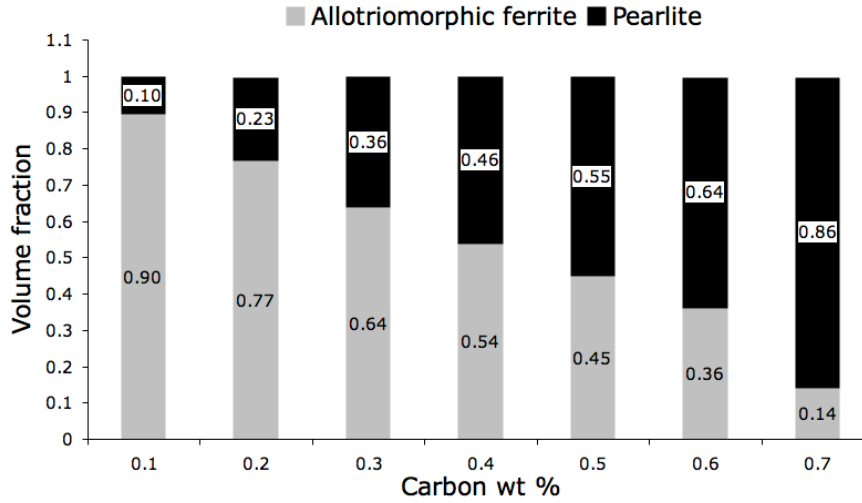
Figure 5.1: Predicted volume fractions of allotriomorphic ferrite and pearlite. Cooling rate was 0.05 °C s^{-1}. Austenite grain size was 30 μm.
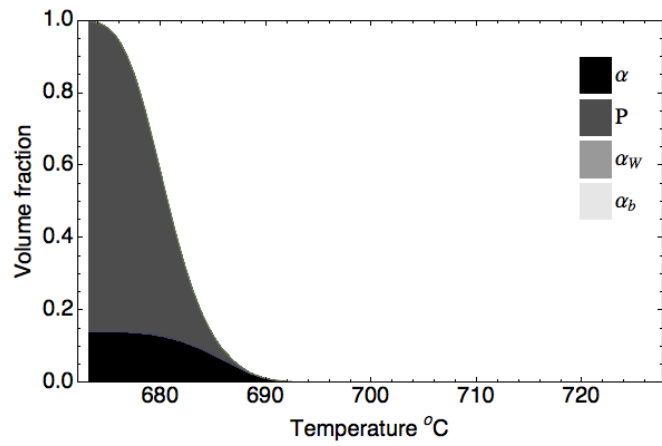
5.2 Substitutional Alloying Elements

Adding alloying elements to plain carbon steels can dramatically extend the properties of carbon steels and also introduce new properties. Alloying elements alter the driving force of transformation (section 2.3) and the interaction energy between carbon atoms (section 2.1.2). A thorough discussion of this subject is beyond this thesis, but details can be found in the references [65, 66, 1].

Substitutional alloying elements to be discussed are silicon, manganese, nickel, chromium, molybdenum and boron. One of their effects on steel is that they affect the shape of the austenite γ field in the Fe-C phase diagram. According to a scheme introduced by Wever, alloying elements expand or contract the γ field by raising or lowering the Ae_4 and the Ae_3 temperatures. In extreme scenarios, the austenite stabilising alloying elements can open the γ field, or the ferrite stabilising elements can contract the γ field so much so that at a certain carbon concentration and above, there is no solid-state phase transformation in steel (Fig. 5.3).

A ternary Fe-C-X system is used for the study, where X stands for any of the six elements. Carbon concentration was set at 0.6 wt % and the cooling rate was 1.0 °C s^{-1}. The austenite grain size was set at 30 μm. The predicted results are summarised on Tab. 5.3.
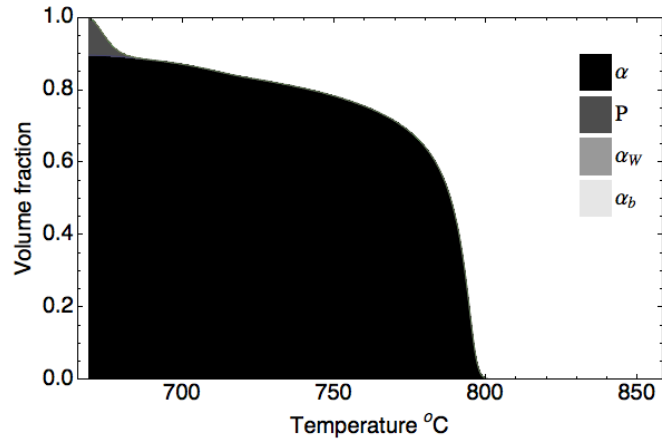
(a) Fe - 0.1 wt % C

(b) Fe - 0.7 wt % C

Figure 5.2: Comparison of the transformations in steels with 0.1 wt % carbon and 0.7 wt % carbon at a cooling rate 0.05 °C s^{-1}.
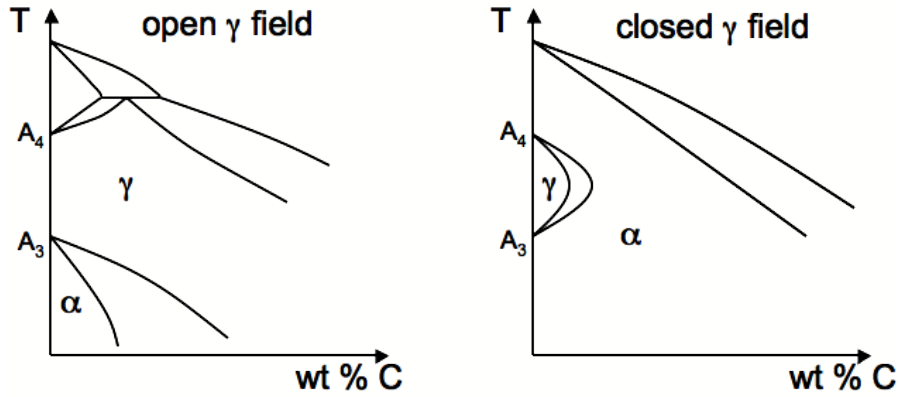
Figure 5.3: The extreme scenarios of the effects of substitutional alloying elements on the austenite γ field in the Fe-C phase diagram [67].

	Fe-(C)	Fe-C-(Si)				Fe-C-(Mn)			
(wt %)	0.6	0.5	1.0	1.5	2.0	0.5	1.0	1.5	2.0
α	0.164	0.169	0.174	0.180	0.186	0.147	0.127	0.078	0.001
P	0.833	0.828	0.821	0.817	0.809	0.850	0.870	0.919	0.997
α_W	0.000	0.000	0.000	0.000	0.000	0.001	0.000	0.000	0.000
α_B	0.000	0.000	0.000	0.000	0.000	0.000	0.000	0.000	0.000
		Fe-C-(Ni)				Fe-C-(Mo)			
(wt %)		0.5	1.0	1.5	2.0	0.5	1.0	1.5	2.0
α		0.150	0.137	0.125	0.112	0.161	0.158	0.155	0.152
P		0.846	0.860	0.872	0.886	0.834	0.839	0.843	0.844
α_W		0.000	0.000	0.001	0.000	0.000	0.000	0.000	0.000
α_B		0.000	0.000	0.000	0.000	0.000	0.000	0.000	0.000
		Fe-C-(Cr)				Fe-C-(B)			
(wt %)		0.5	1.0	1.5	2.0	0.0005	0.001	0.0015	0.002
α		0.156	0.148	0.140	0.131	0.153	0.147	0.086	0.086
P		0.842	0.849	0.857	0.865	0.840	0.829	0.726	0.726
α_W		0.000	0.000	0.001	0.001	0.003	0.021	0.186	0.186
α_B		0.000	0.000	0.000	0.000	0.000	0.000	0.000	0.000

Table 5.3: The predicted volume fractions of various phases. The values in weight percent are for the concentrations of any element in bracket (). The ferrite data are plotted in Fig. 5.4.
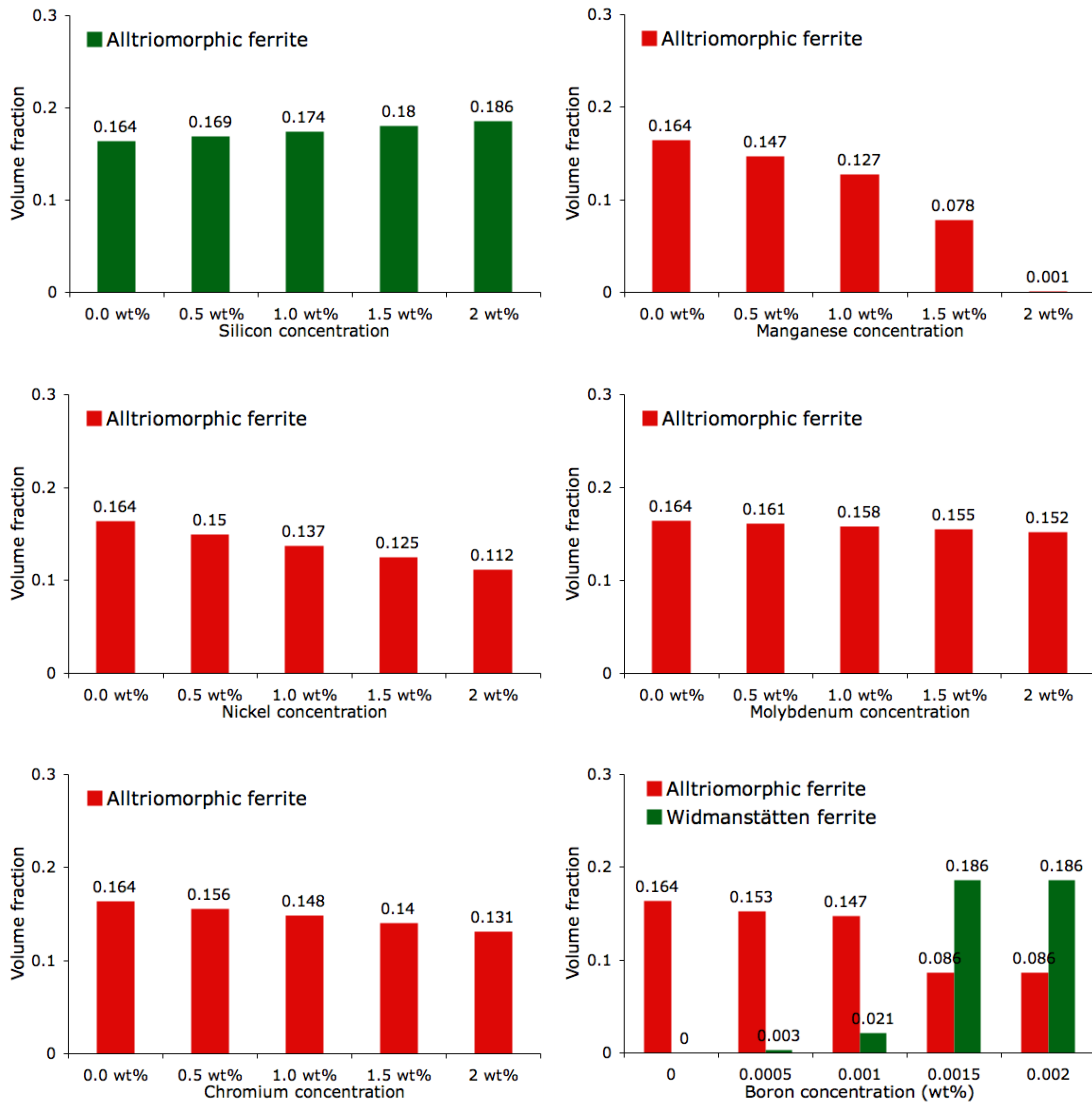
Figure 5.4: The comparison of the effect of alloying elements on ferrite formation.

The experimental work by Andrews [68] has shown the relative strengths of alloying elements (Fig. 5.5). The predictions for Si, Mn and Ni of their effects and the strength of the effects on austenite or ferrite are comparable with experimental data. Mo and Cr are experimentally identified as ferrite formers. However the calculations have shown that the presence of Mo and Cr has a slight negative effect on ferrite formation.

Boron has been recently integrated into the model. The work of adding boron

has not been completed, as the interaction of boron with titanium and nitrogen has not been fully integrated into the model (Appendix A). Nevertheless, boron has been correctly predicted by the model as having a negative effect on the formation of allotriomorphic ferrite.
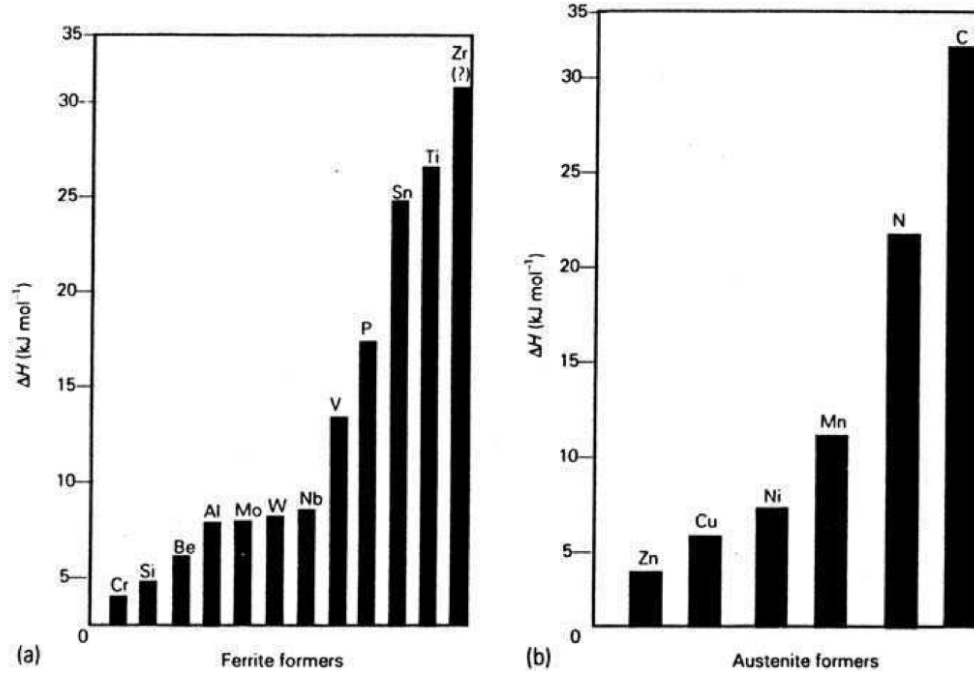

Figure 5.5: Relative strength of alloying elements as: (a) ferrite formers; (b) austenite formers [68].

5.3   Grain Size

To study the effect of grain size, the choice of the chemical composition was a mildly alloyed steel (Tab. 5.4). The tests were performed on transformations with

C	Si	Mn	Ni	Mo	Cr	V	Cooling rate
0.2	1.21	1.382	0.1	0.32	1.19	0.0	2.0 °C s^{-1}

Table 5.4: The chemical composition (wt %) of the steel sample used to explore the effect of grain size.

a cooling rate 2.0 °C s^{-1}. The values of austenite grain sizes used in the tests are listed on Tab. 5.5.

grain size (μm)	10	20	50	100

Table 5.5: The austenite grain sizes used in the test.

A grain boundary is the border between two crystals, a region in which atoms are packed less perfectly than in the defect-free lattice. Such boundaries are good places for heterogeneous nucleation. Steels having smaller austenite grains will have a larger surface area of grain boundaries per volume (Fig. 5.6). Hence, small
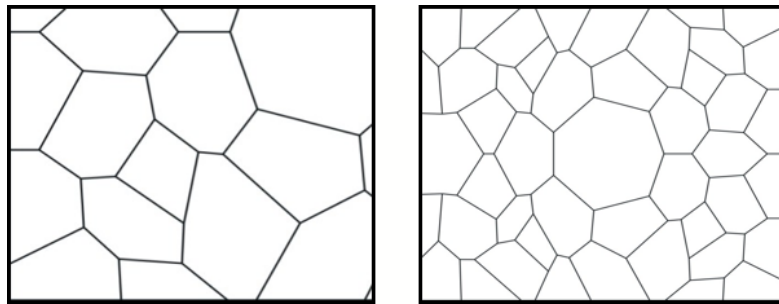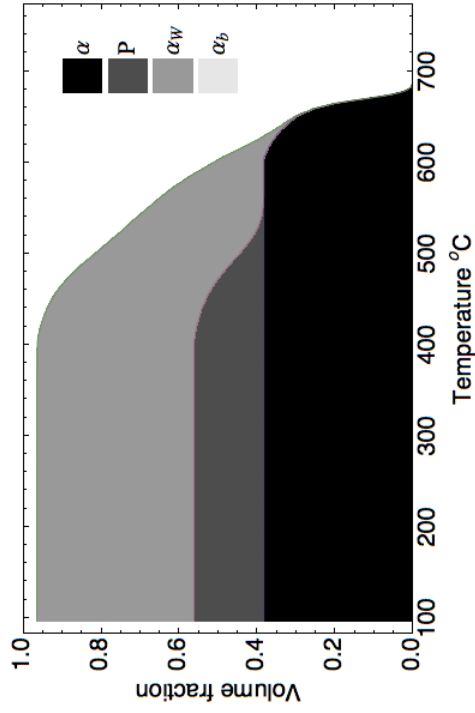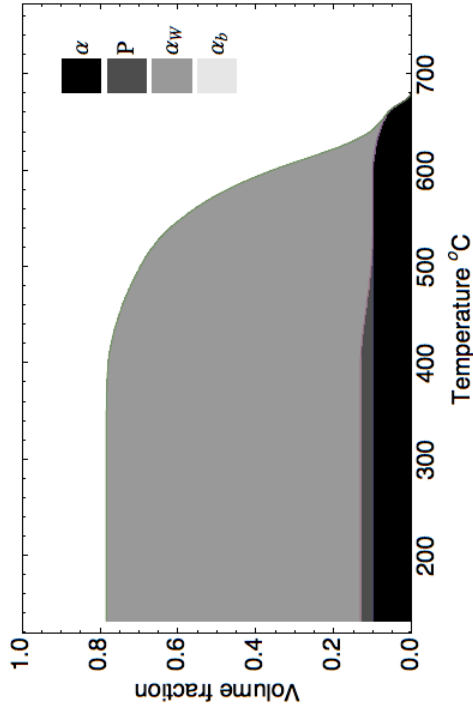

Figure 5.6: Steel with smaller austenite grain size has larger gain boundary surface area per unit volume.

austenite grains effectively increase the number density of nucleation sites and should increase the fraction of α and P as the model has predicted (Fig. 5.7).
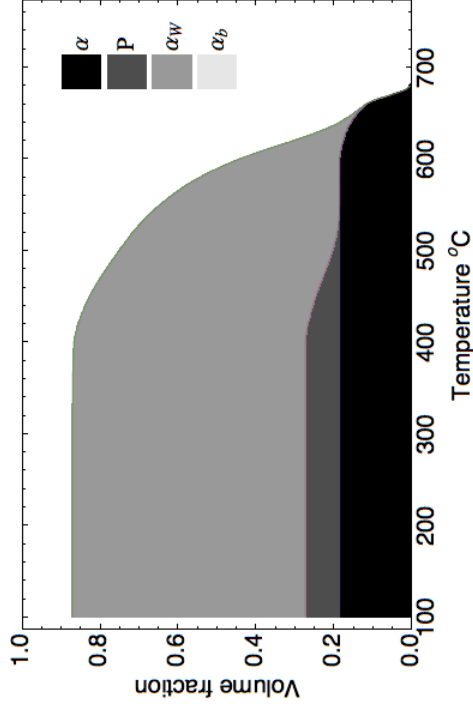
Figure 5.7: The figures show the effect of grain sizes. Note there is a decrease of reconstructive transformation products α and P and increase of displacive products α_W and martensite (in the case of $\bar{L} = 100 \ \mu m$, there is over 20 % martensite).

5.4   Cooling Rates

The rate of transformation is greatly affected by the temperature at which it takes place. For this reason, the cooling rate is an important factor in the development of microstructure. The test was to validate the model whether it could reproduce the effect of cooling rate as would be expected. The chemical composition was the same as in Tab. 5.4. The value of cooling rates chosen for the tests are listed in Tab. 5.6.

Cooling rate ($°C\ s^{-1}$)	0.1	0.3	0.5	1.0	1.5	2.5	3.5	4.5	8	15	25

Table 5.6: The cooling rates used in the test. The austenite grain size was set as 30 μm.

The predicted volume fractions are summarised on Tab. 5.7 and plotted in Fig. 5.8. They demonstrate that with increasing cooling rates, there is a decrease of reconstructive transformation products (α and P), and an increase of displacive products (α_W and martensite).

CR	0.1	0.3	0.5	1.0	1.5	2.5	3.5	4.5	8	15	25
α	0.658	0.501	0.426	0.345	0.306	0.264	0.236	0.236	0.174	0.122	0.091
P	0.340	0.307	0.287	0.247	0.220	0.063	0.009	0.009	0.000	0.000	0.000
α_W	0.000	0.189	0.285	0.406	0.468	0.522	0.506	0.506	0.282	0.050	0.008
α_B	0.000	0.000	0.000	0.000	0.000	0.000	0.000	0.000	0.000	0.000	0.000
α'	0.000	0.000	0.000	0.000	0.006	0.151	0.249	0.249	0.544	0.828	0.901

Table 5.7: Transformation products predicted from mildly alloyed steel (se Tab. 5.4). CR stands for cooling rate in unit $°C\ s^{-1}$. Data are plotted in Fig. 5.8.
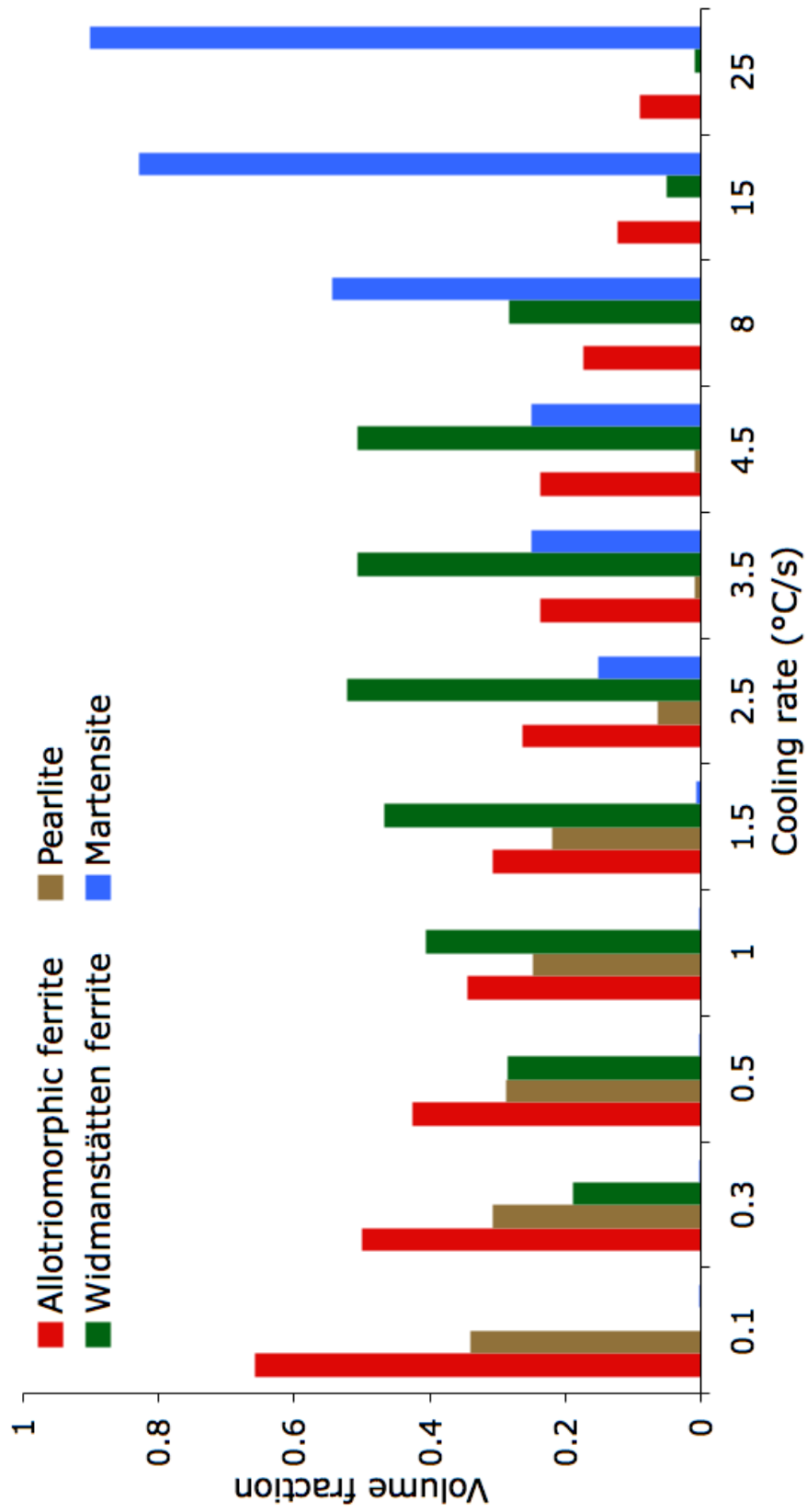
Figure 5.8: The predicted effect of cooling rate on the volume fractions of various transformation products.

Chapter 6

Experimental Validation of the Model

The theory behind the microstructure model is based on decades of research in Cambridge, and large parts of it have been validated independently through a variety of experiments and theoretical assessments. The incorporation of bainite is a major feature of the present work. This chapter describes new experimental validation tests of the model. Some of the test samples and data were supplied by Swiss Steel AG.

6.1 Transformations to allotriomorphic ferrite, pearlite and Widmanstätten ferrite

Bainite was not included in the original model developed by Jones and Bhadeshia [36, 37], who validated the work using the results by Bodnar and Hansen [69]. The chemical composition of the steel used in the experiment was Fe-0.18C-0.18Si-1.15Mn-0.003V wt %. A variety of austenite grain sizes and cooling rates were applied (Tab. 6.1).

The level of agreement between the original model and experiment is illustrated in Fig. 6.1(a). Although the agreement was considered at the time to be reasonable, there clearly are discrepancies and the data are not uniformly distributed about the line of perfect consistency between experiment and theory.

austenite grain size / μm	cooling rate / °C min^{-1}				
30	101	59	30	16	11
55	99	59	30	16	11
100	101	59	30	16	11

Table 6.1: The specifications of the experiments on steel Fe-0.18C-0.18Si-1.15Mn-0.003V wt % by Bodnar and Hansen [69].

Better agreement has been achieved in the present work (Fig. 6.1(b)), in which Most of the main program and some subroutines have been rewritten, though based on the same theories. The improvement of the new results comes from merely the improvement in the quality of program code.
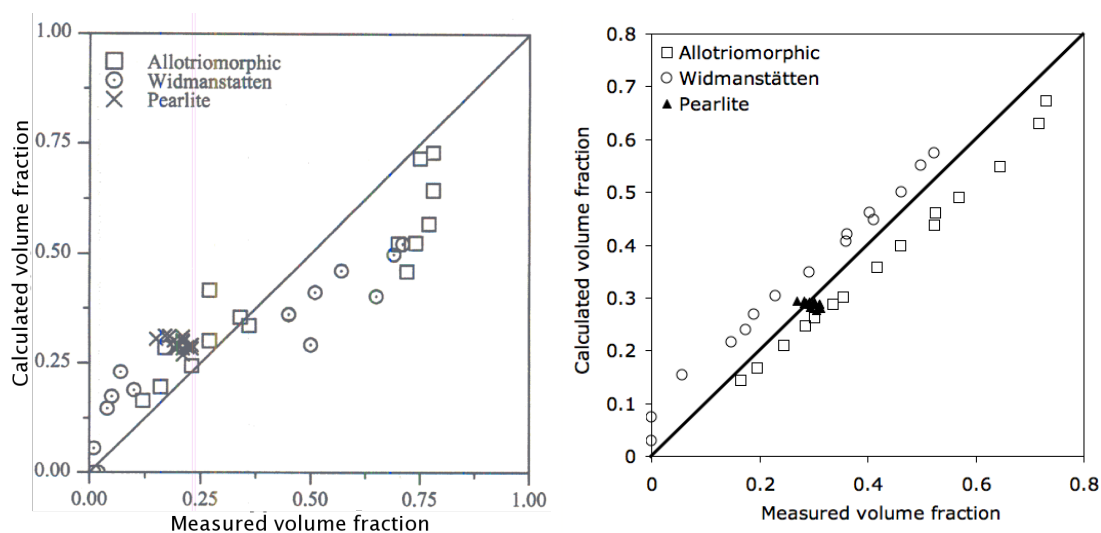

Figure 6.1: (a) Comparison of calculated [37] and measured fractions [69] for the original work by Jones and Bhadeshia. (b) Comparison of calculations produced using the present work, with the Bodnar and Hansen data.

6.2   Isothermal Transformation to Bainite

The theory for bainite reaction used in this model was developed by Matsuda and Bhadeshia [50]. Most of the constants used in the calculations were set by the tests against published data from isothermal experiments on carbide-free bainite

[40]. The steel used in the experiments had chemical composition Fe-0.44C-1.74Si-0.67Mn-1.85Ni-0.83Mo-0.39Cr-0.09V wt % and mean lineal austenite grain size of 86 μm.

The reasonable agreement obtained given the fitting parameters is not surprising (Fig. 6.2). The model has captured the incomplete reaction phenomenon accurately [4, 70]. It has also correctly predicted that the extent of reaction decreases when the isothermal temperature is increased towards the bainite start temperature.
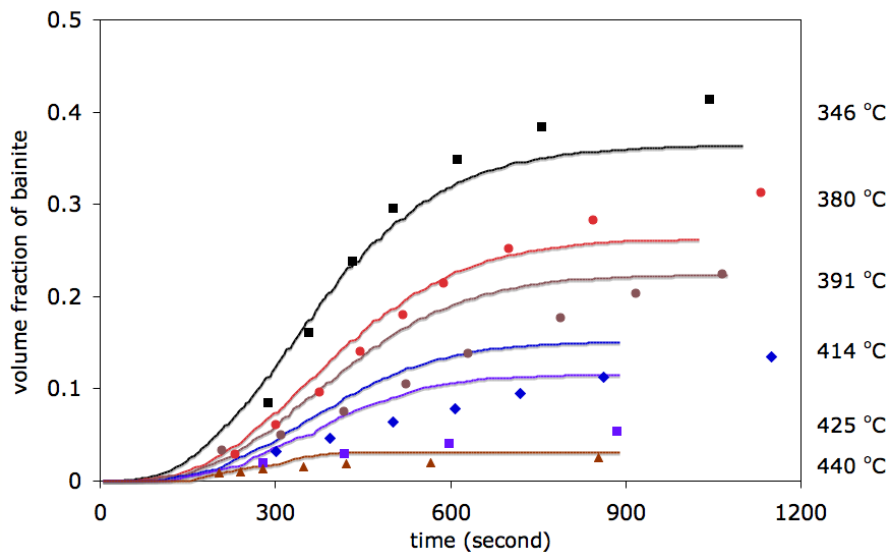

Figure 6.2: Comparison of experimental measurements [40] of the fraction of carbide-free bainite as a function of the isothermal transformation temperature, against computations (curves).

6.3 Case Hardening Steel

Samples of a case hardening steel were supplied by Swiss Steel AG [71]. The molten steel was produced in an electric arc furnace from scrap, and then cast continuously into 140×140 mm billets. These were then reheated to 1200°C and hot-rolled into wire-rods or bars. The final product was in the forms, 6.5 mm diameter wire rod, 23.5 mm diameter wire rod and 36 mm diameter bar.

6.3.1 Sample with 6.5 mm diameter

The 6.5 mm wire rod was processed in a Stelmor controlled-cooling conveyor. In the Stelmor line, coils are separated and each ring of a coil is treated under the same cooling condition. The cover of the production line allows slow and homogeneous cooling. For wires at this diameter, the cooling rate is not expected to vary much from the surface to the core of the wire. The chemical composition of the steel is given in Tab. 6.2. The surface cooling rate between 800 °C and 500 °C measured by a pyrometer was 0.34 °C s^{-1}.

C	Si	Mn	Ni	Mo	Cr	V	Cooling Rate / °C min^{-1}
0.16	0.21	1.21	0.13	0.015	0.98	0	20.4

Table 6.2: The chemical composition (wt %) of the steel wire with the diameter of 6.5 mm.

To determine the austenite grain size $\bar{L}$, samples need to be taken just before any phase transformation starts, prior to the last hot-rolling stage. The grain size was then determined using an optical microscopy. It increases from the surface (20±2 μm) to the core of the wire (36±4 μm) (Fig. 6.3).

(a) At the surface   (b) At the core
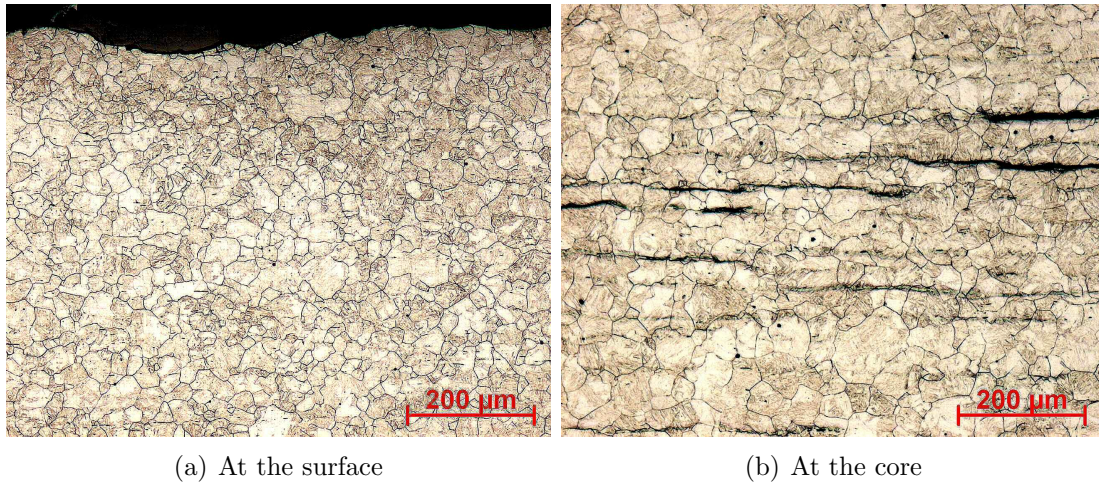
Figure 6.3: The austenite grain size of the 6.5 mm sample is 20±2 μm on the surface and 36±4 μm at the core (measured by Swiss Steel).

The experimental results and the corresponding predictions from the model

are summarised in Tab. 6.3. The superscript in V_α^e refers to an experimentally measured value, whereas the superscript in V_α^c stands for a calculated value.

	grain size / μm	V_α^e	V_α^c	V_P^e	V_P^c	$V_{\alpha_B}^e$	$V_{\alpha'}^e$	$V_{\alpha_W}^c$	$V_{\alpha_B}^c$	$V_{\alpha'}^c$
surface	20.3	0.75	0.66	0.21	0.24	0.01	0.02	0.10	0	0
1/2 radius	25.4	0.71	0.58	0.15	0.24	0.07	0.07	0.18	0	0
core	36.2	0.71	0.45	0.09	0.23	0.09	0.11	0.32	0	0

Table 6.3: Calculated and measured phase fractions on a 6.5 mm diameter rod cooled at 0.34 °C s^{-1}. The grain sizes presented are the mean values (measured by Swiss Steel). The superscript in V_α^e refers to an experimentally measured value, whereas the superscript in V_α^c stands for a calculated value. This convention applies throughout.

The test shows there is a general decrease in the volume of allotriomorphic ferrite and pearlite at the core compared with the surface. This trend is reproduced in the predictions, because of the difference in the austenite grain size which leads to corresponding variations in the development of microstructure.

The predictions at the core is relatively worse than that on the surface. The same observation can be found in the following two samples with 23.5 mm and 36 mm diameter. The deviation may be due to the composition variance suggested in some metallographic images, which are not accounted for in the model.

The discrepancy observed in the displacive transformations may be due to the difficulty for Swiss Steel to differentiate Widmanstätten ferrite and bainite under microscopy, or may be due to the growth rate of α_W, which may be overpredicted. The concern of α_W will be discussed in the next section.

If the grain size at half radius is considered to represent the mean value in the sample, the comparison between calculation and measurement is reasonably good if in the former case the Widmanstätten ferrite, bainite and martensite are combined (Fig. 6.4).

6.3.2 Sample with 23.5 mm diameter

The second trial, 23.5 mm wire rod, was performed in the Garrett coiling line. In this line, the wire is coiled after hot rolling, which leads to a change in the cooling rate between the outer and inner rings of a coil. Such a compact coil cools slowly
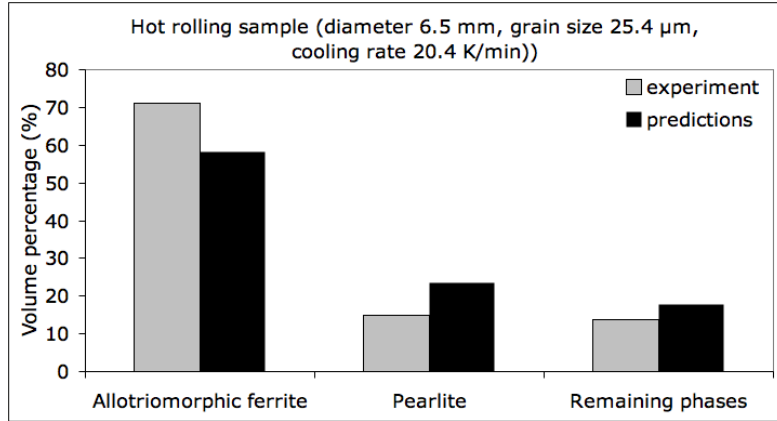
Figure 6.4: Calculated and measured phase fractions for the 6.5 mm diameter sample with a mean austenite grain size of 25.4 μm

and the measured cooling rate was 0.16 °C s^{-1}. The composition of the steel is given in Tab. 6.4.

C	Si	Mn	Ni	Mo	Cr	V	Cooling Rate / °C min^{-1}
0.2	0.19	1.23	0.11	0.017	1	0	9.6

Table 6.4: The chemical composition (wt %) of the steel from the 23.5 mm Garrett rolling trial.

The sampling for the determination of austenite grain size was made after coiling, and before the steel samples were quenched into water. The size changes from 26±2 μm at the surface to 50±4 μm at the centre of the sample. Because of the lower cooling rate at the core, a smaller amount of displacive transformation products were observed there. The results are summarised in Tab. 6.5.

	grain size / μm	V_α^e	V_α^c	V_P^e	V_P^c	$V_{\alpha_B}^e$	$V_{\alpha'}^e$	$V_{\alpha_W}^c$	$V_{\alpha_B}^c$	$V_{\alpha'}^c$
surface	26	0.66	0.64	0.35	0.32	0	0	0.03	0	0
1/2 radius	31.8	0.57	0.58	0.41	0.32	0.02	0	0.10	0	0
core	49.5	0.78	0.42	0.22	0.32	0.01	0	0.26	0	0

Table 6.5: Calculated and measured phase fractions from a 23.5 mm diameter rod cooled at 0.16 °C s^{-1}. The grain sizes are mean values measured by Swiss Steel.

A reasonable overall agreement is obtained with the estimates from the model. In the case of the microstructure at a depth equal to half the radius, a region which

is considered to represent the mean grain size, there is a large discrepancy in the prediction of remaining phases. A possible explanation is that although the model can distinguish between phases, it may be difficult to do so in practice without the use of a variety of techniques other than optical microscopy (Fig. 6.5).
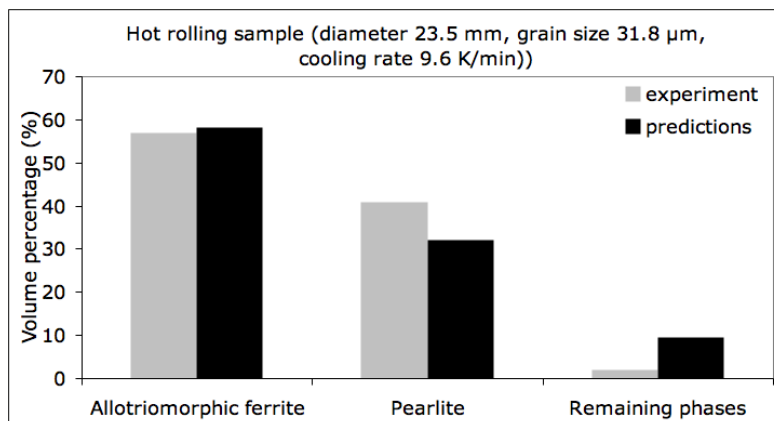

Figure 6.5: Calculated and measured phase fractions for the 23.5 mm diameter sample with a mean austenite grain size of 31.8 μm.

6.3.3 Sample with 36 mm diameter

In the third trial, a 36 mm bar was produced. The predictions for a thick bar can be challenging, because the cooling rate varies much from the surface to the core, with a large variation in the austenite grain size. The latter changes from 19 μm at the surface, to 67 μm at the centre. The composition of the steel is given in Tab. 6.6.

C	Si	Mn	Ni	Mo	Cr	V	Cooling Rate / °C min^{-1}
0.17	0.19	1.22	0.09	0.018	1.03	0	48

Table 6.6: The chemical composition (wt %) of the steel from a 36 mm diameter bar. The cooling rate is measured on the surface. Because of the dimension of the bar, the cooling rate can be expected to be lower in the core.

The combined bainite and martensite content at the surface is 23%. It is higher than the smaller diameter samples, because of relatively higher cooling rate (0.8 °C s^{-1}) at the surface. Despite of slower cooling rate in the core, large grain size

discouraged the nucleation of allotriomorphic ferrite and pearlite, hence there is 86% bainite and martensite at the core of the bar. The results are summarised in Tab. 6.7.

	grain size / μm	V_α^e	V_α^c	V_P^e	V_P^c	$V_{\alpha_B}^e + V_{\alpha'}^e$	$V_{\alpha_W}^c$	$V_{\alpha_B}^c$	$V_{\alpha'}^c$
surface	19.3	0.48	0.56	0.29	0.23	0.23	0.22	0	0
1/2 radius	47.8	0.34	0.27	0.09	0.21	0.58	0.51	0	0
core	66.9	0.13	0.20	0.02	0.21	0.86	0.58	0	0

Table 6.7: Calculated and measured phase fractions from a 36 mm diameter rod cooled at 0.8 °C s^{-1}

Considering the microstructure at half of the radius as the mean value, the comparison between the predictions and measurements is illustrated in Fig. 6.6.
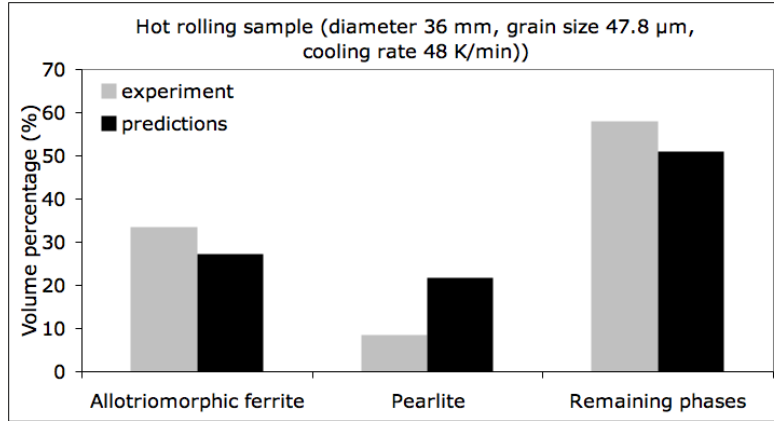

Figure 6.6: Calculated and measured phase fractions for the 36 mm diameter sample, with a mean austenite grain size of 47.8 μm.

6.4 Continuous Cooling Transformation Diagrams

A continuous cooling transformation (CCT) diagram was produced (Fig. 6.7) on a steel having the composition listed in Tab. B.3. The transformation time was determined by dilatometry measurements conducted by Swiss Steel AG.

Pearlite was never observed in these tests. As sulphur can combine with manganese to form MnS, the Mn content in solution was calculated using an empirical equation (Mn wt %)$-1.72\times$(S wt %) suggested by Hans Roelofs in Swiss Steel.

C	Si	Mn	Ni	Mo	Cr	V	S	Grain Size / μm
0.2	1.21	1.64	0.1	0.32	1.19	0.0	0.15	30

Table 6.8: The chemical composition (wt %) of the steel samples.

Because manganese sulphide acts as a heterogeneous nucleation site for ferrite, the calculation should underestimate the ferrite content. Swiss Steel AG has expressed the concern that Widmanstätten ferrite and bainite can be challenging to distinguish.
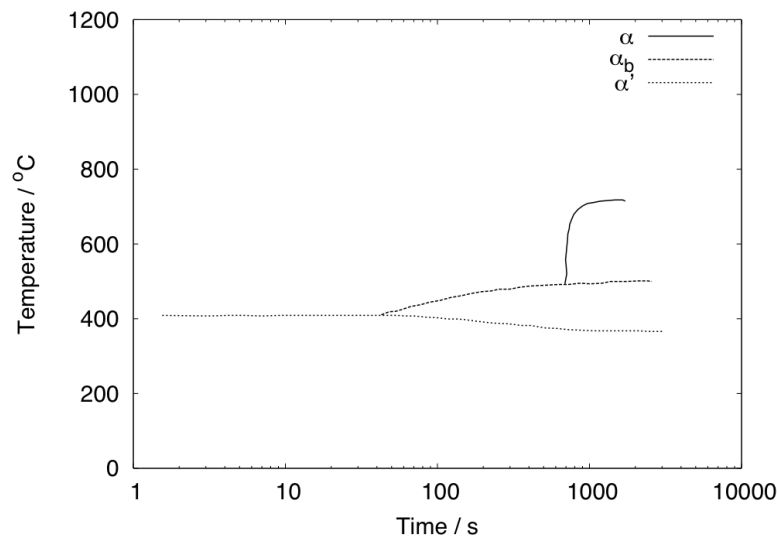

Figure 6.7: Measured continuous cooling transformation (CCT) diagram by Swiss Steel AG.

The allotriomorphic ferrite start curve in the prediction extended into the high cooling rate area where in the measured CCT diagram there is no ferrite transformation (Fig. 6.8). This may be an issue in the growth rate of allotriomorphic ferrite in the model. Pearlite is not predicted and this agrees with the experiments. The displacive transform product was considered as bainite in the experiments, whereas it is predicted as Widmanstätten ferrite by the model. Martensite start curves have a good agreement between the measured and predicted data.
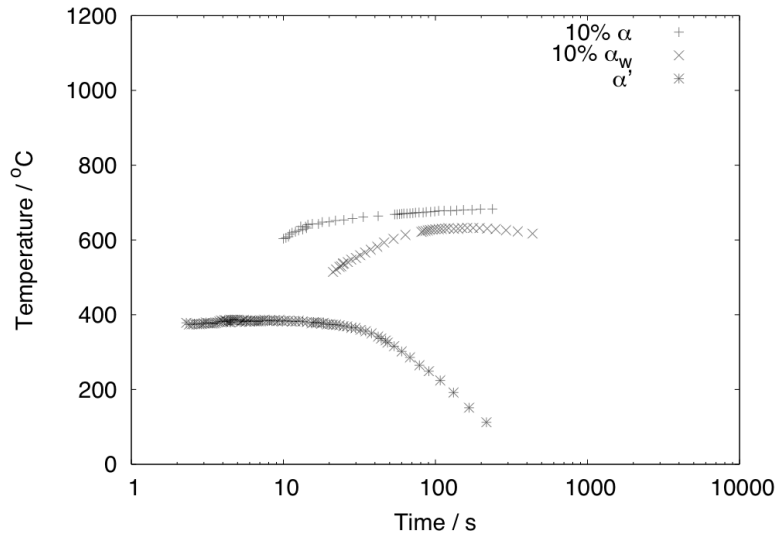
85

Figure 6.8: Predicted Continuous cooling transformation (CCT) diagram by the model.

6.5 Dilatometric Tests

6.5.1 The experiment

A 600 g steel ingot was made using refined iron and high-purity alloying elements in an induction furnace to yield the composition shown in Tab. 6.9. It was melted

C	Si	Mn	Ni	Mo	Cr	V	S
0.2	1.21	1.64	0.1	0.32	1.19	0.0	0.15

Table 6.9: The chemical composition of the ingot (wt %).

and cast into a cylinder 35 mm in diameter and 85 mm in length (Fig. 6.9).

To reduce segregation in the ingot, so samples cut from the ingot can have similar composition, the ingot was homogenised at 1200 °C for 48 h. The ingot was then wire-cut into dilatometry samples as circular cylinders of 12 mm in length and 8 mm in diameter.

The dilatometry experiments were performed in a thermo-mechanical simulator, THERMECMASTOR-Z. A sample was placed inside an induction coil in vacuum. Then the machine implements a programmed thermal treatment on the
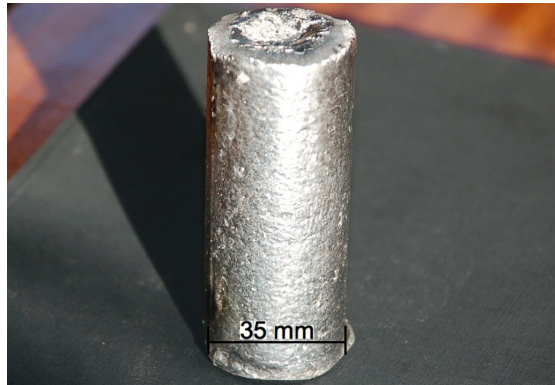
Figure 6.9: The steel ingot made for the dilatometric tests 35 mm diameter and 85 mm length.

sample. It heats the sample generated by the induction coil and cools the sample using compressed helium gas. The surface temperature of the sample was monitored continuously by a thermocouple welded on the side throughout the experiment. The change in diameter was measured by a laser passing across the sample.

In each test, a sample was heated from room temperature to 900 °C at a rate of 10 °C s^{-1}, then held at 900 °C for 10 min, then quenched from 900 °C to a pre-set temperature at a rate of 40 °C s^{-1}, and finally held at that temperature for 120 min. The test temperatures were 750, 710, 670, 630, 610, 590, 550, 510, 470 and 430 °C.

The transformed sample was then cut at the point where the thermocouple was attached (about half way along the length). Each half was mounted. The cut surface was then ground, polished and etched using 2 % Nital (2 % nitric acid in methanol) for about 20-30 s (samples tested at low isothermal temperature required less time).

6.5.2 Austenite grain size

Two samples were tested to determine the austenite grain size at the end of the 10 min held at 900 °C. The austenite grains were preserved by quenching the sample at rate 40 °C s^{-1} from 900 °C down to the room temperature.

Before the test, the sample was worn down at one side to create a facet, near

which a thermocouple would be welded. The facet was then polished before the sample was placed into the testing machine. The partial oxidation of the polished surface at the austenitisation temperature reveals the prior austenite grains. This method is called thermal etching.

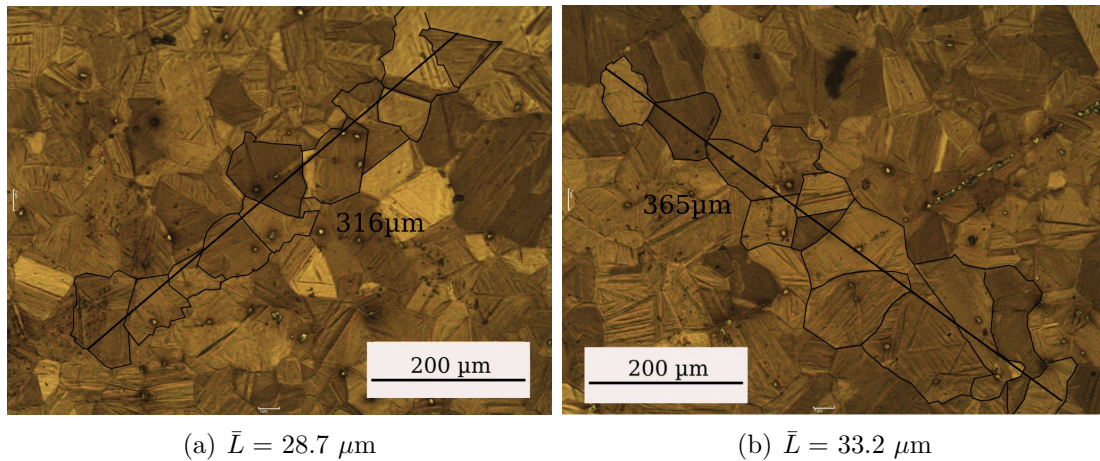The mean linear grain size is estimated as 30.9 μm (Fig. 6.10).

(a) $\bar{L} = 28.7$ μm   (b) $\bar{L} = 33.2$ μm

Figure 6.10: Two examples to illustrate the method used to obtain the mean linear grain size. The average value of $\bar{L}$ is estimated as 30.7 μm.

6.5.3 Martensite temperature

Quenching the sample from 900 °C to room temperature at a rate of 40 °C s^{-1} in the tests for the austenite grain size guarantees a completely martensitic microstructure. As martensite transformation causes a reverse change on the dilation-time curve, The martensite-start temperature was determined as about 390 °C (Fig. 6.11).

Another martensite-start temperature was produced by the dilation-time curve of the test at 590 °C. When the power was switched off at the end of the 2 h isothermal transformation, the sample started to cool by radiation at a rate about 12 °C s^{-1}. There was a reverse change on the dilation-time curve clearly revealed at around 410 °C (Fig. 6.12).

The difference between the martensite-start temperatures obtained by the two experiments is caused by the temperature gradients in the testing sample. When
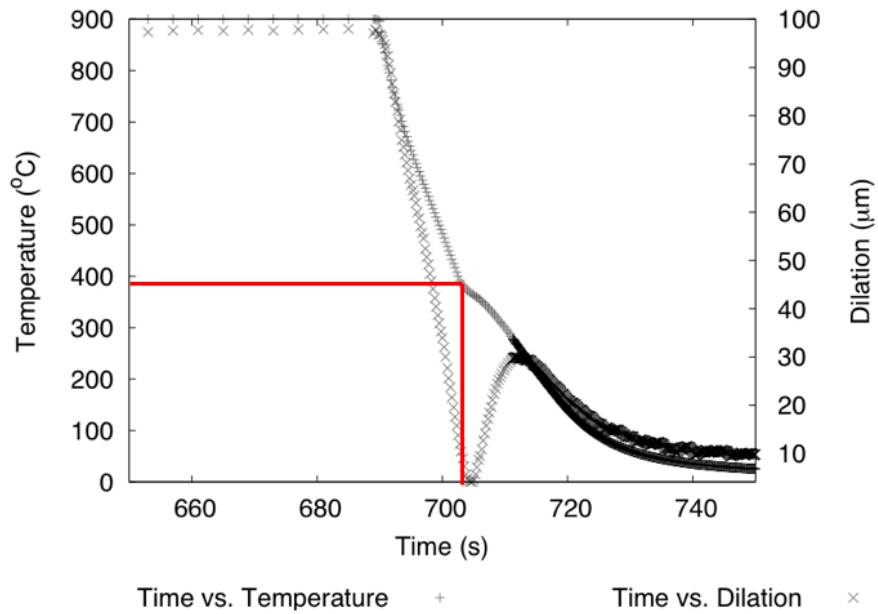
Figure 6.11: Temperature and dilation vs. time for the sample quenched by gas from 900 °C at rate 40 °C s^{-1}. The dilation-time curve reverses at about 390 °C.

a sample is quenched at high rate, there is a larger temperature gradient from the surface to the core. The transformation at the core of the sample is behind the transformation on the surface. Therefore, the reading by the thermocouple, which reads the surface temperature is below the real martensite-start temperature.
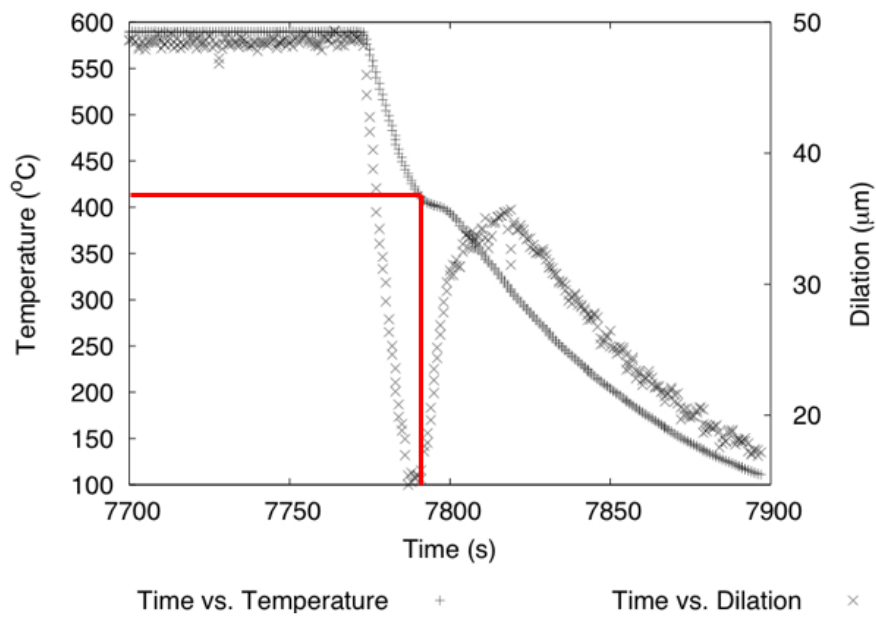
Figure 6.12: Temperature and dilation vs. time for the sample cooled by radiation from 590 °C at rate about 12 °C s^{-1}. The dilation-time curve reverses at about 410 °C.

6.5.4 Results

The discussion in this section will be in two parts. The first part analysis is to determine what phases are present in a metallographic image and how much of each phase there is. To maintain readability, a large number of the metallographic images and related plots of the dilation data are moved to the end of the chapter. The second part discussion concerns the transformation-start time for each test and the difficulty in estimating an accurate value.

The dilation data alone were inadequate to identify the phases. To have a more definitive identification, micro-hardness tests were performed on some individual grains of every testing sample. The results of micro-hardness tests on every sample are summarised on Tab. 6.10.

Temp. / °C	testing area	test 1	test 2	test 3	test 4	average
750	light	262.4	238.6	258.1		253.0
	dark	391.9	380.1	383.5		385.2
710	light	184.9	220.2			202.5
	dark	494.3	478.8			486.5
670	light	199.1	177.2	146.5		174.3
	dark	473.9	467.4	519.6		487.0
	black	212.4	210.8			211.6
630	light	263.6	226.4	237.3		242.4
	dark	436.4	436.3	416.8	408.6	424.5
610	light	214.0	195.7			204.8
	dark	405.1	394.7			399.9
590	random	392.5	372.3	387.6		384.1
550	random	389.4	391.8	399.9		393.6
510	random	416.5	392.0	413.6		407.4
470	random	375.9	386.9	386.7		383.1
430	random	321.9	351.3	316.7		330.0

Table 6.10: Results of micro-hardness tests in H_v.

Microstructure analysis

The following analysis of the microstructure of every test is based on combined information of hardness, dilation curve and metallographic features.

750 °C

Referring to Fig. 6.18, there are two easily distinguishable phases. The average hardness on the light areas is 253.0 H_v, and on the dark matrix is 385.2 H_v. The dilation curve confirms some transformation during the 2 h isothermal treatment. The method used to estimate volume percent is to randomly place a 10x10 grid on the image, then count the numbers of boxes filled by any phase. The combined information suggests the microstructure consists of 6 % allotriomorphic ferrite and 94 % martensite, which was formed from the untransformed austenite when the sample was cooled from 750 °C at the end.

710 °C

Referring to Fig. 6.20, it has similar feathery morphology as 750 °C with extended light-coloured regions. The average hardness on the light area is 202.5 H_v and on the dark matrix is 486.5 H_v. Using the same method in the previous test, it was estimated that the microstructure consists of 23 % allotriomorphic ferrite and 77 % martensite.

670 °C

Referring to Fig. 6.22, the light-coloured regions are further extended. There are some very dark small areas which were not observed in the previous tests. The hardnesses on these dark areas were 212.4 and 210.8 H_v, which suggests these dark areas may be merely over-etched allotriomorphic ferrite. The average hardness on the light areas is 174.3 H_v and on the dark matrix is 487.0 H_v. It was estimated that the microstructure consists of 37 % allotriomorphic ferrite and 63 % martensite.

630 °C

Referring to Fig. 6.24, the size of the light regions appears smaller, which reverses the trend set in the previous three tests. The average hardness on the light area is 242.4 H_v and on the dark areas is 424.5 H_v. It was estimated that the microstructure consists of 19 % allotriomorphic ferrite and 81 % fine-structure material.

610 °C

Referring to Fig. 6.26, the area of light regions is further reduced. The average hardness on the light area is 204.8 H_v and on the dark 399.9 H_v. The microstructure consists of 12 % allotriomorphic ferrite and 88 % fine-structure material.

590 °C

Referring to Fig. 6.28, the previously seen light-coloured regions have completely disappeared. But the rising dilation curve suggests an other transformation had occurred. Feather like features are visible on the metallographic image, which may suggest bainite. The existence of martensite was confirmed, as the dilation curve reversed and rose up at temperature 410 °C during the cooling after 2 h (Fig. 6.12). The average hardness is 384.1 H_v. The entire microstructure is a fine-structure material, which is believed to be a mixture of bainite and martensite. However, these phases cannot be unambiguously determined from optical microscopy.

550 °C

Referring to Fig. 6.30, the microstructure is similar to that obtained at 590 °C and is believed to consist of a mixture of bainite and martensite. Some transformation was confirmed by the slightly rising dilation curve. The average hardness rose to 393.6 H_v, which may suggest more martensite formed from untransformed austenite at the end of the test.

510 °C

The almost flat dilation curve can be hardly useful to confirm any transformation. Neither can it rule out transformation happened at all. The average hardness is 407.4 H_v. The microstructure is again believed to consist of bainite and martensite. But it is hard to distinguish them in the metallographic images. To make a definitive determination, it requires electron microscopy.

470 °C

From this temperature, the dilation curve rises again, which indicates some transformation during the 2 h at 470 °C. The hardness result breaks the trend

and begins to decrease. The average hardness is 383.1 H$_v$. Like 510 °C, the microstructure is believed to be a combination of bainite and martensite.

430 °C

Referring to Fig. 6.36, at higher magnification, transformed grains are found to be confined only in one side of the austenite grain boundary and having feather-like appearance (Fig. 6.13). The average hardness reduces further down to 330.0 H$_v$.
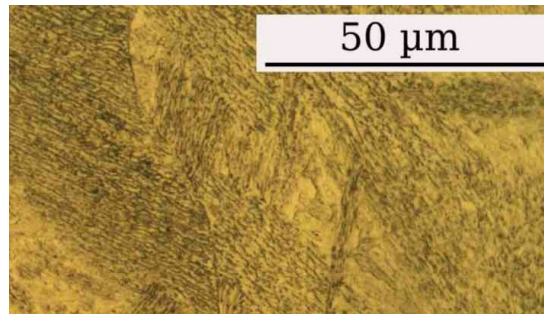

Figure 6.13: Bainite microstructure in magnitude 500X.

Judging by the time span of the dilation curve and the metallographic observations, the transformation product is believed to be mainly bainite.

The microstructures of the samples tested are summarised in Tab. 6.11 together with the predictions by the model. The pearlite predicted by the model was not seen in the metallographic images.

Transformation start time

The transformation start time of each test was estimated based on the dilation versus time curve. A rising dilation curve can indeed indicate a transformation occurring inside a sample. But the dilation curves seem to be poor indicators of the transformation start time. A crude model may be able to clarify this.

Consider a growing cube with edge length a, as one phase γ transforms to another phase α inside the cube. The cube weighs M and the weight fraction of α is x. The densities of the phases are ρ_α and ρ_γ. The edge length a as a function of x has the form

$$a^3 = \frac{Mx}{\rho_\alpha} + \frac{M(1-x)}{\rho_\gamma}$$

Temp. / °C	α^e	P^e	$\alpha_W^e + \alpha_B^e + \alpha'^{,e}$	α^c	P^c	$\alpha_W^c + \alpha_B^c$	$\alpha'^{,c}$
750	0.06	0.00	0.94	0.00	0.00	0.00	1.00
710	0.23	0.00	0.77	0.02	0.00	0.00	0.98
670	0.37	0.00	0.63	0.63	0.00	0.02	0.35
630	0.19	0.00	0.81	0.34	0.18	0.38	0.10
610	0.12	0.00	0.88	0.26	0.34	0.40	0.00
590	0.00	0.00	1.00	0.00	0.32	0.68	0.00
550	0.00	0.00	1.00	0.00	0.26	0.74	0.00
510	0.00	0.00	1.00	0.00	0.20	0.80	0.00
470	0.00	0.00	1.00	0.00	0.00	0.43	0.57
430	0.00	0.00	1.00	0.00	0.00	0.56	0.44

Table 6.11: The volume fraction of various phases. As it is extremely hard to distinguish accurately between bainite, Widmanstätten ferrite and martensite, the estimated value is a combined volume fraction of these phases. Superscript in α^e indicates estimated value and the superscription in α^c indicates calculated value.

The edge length is three orders smaller than weight fraction. Furthermore, x itself is a function of time. The growth of a new phase is often slow at the very beginning of transformation, due to the incubation time. Therefore a could be a few more orders smaller than t. It follows that the time lapse at the beginning of a transformation can only lead to a very small change of edge length a, which is measured as the dilation change in the experiments. It may be hard to detect the rise of dilation at the beginning, as it is so many orders smaller than time.

The estimated start times of all the tests are collected in Tab. 6.12. For the reason above, all the estimations of the transformation start time may be well over-valued.

6.5.5 Comparison with predictions

It is not the intention of this experimental work to produce a rigourous time-temperature transformation diagram for the steel. To determine the transformation start time for a TTT diagram, a better method would be to study the metallographic image on a series of samples quenched after a gradually reduced reaction time. And the tests have to be performed over a range of temperatures. Such work would require far more tests and samples than we have.

Temp. / °C	estimated start / s	predicted start / s
710	600	∞
670	300	α: 6.5, α_W: 228.0
630	50	α: 2.9, α_W: 12.2
610	450	α: 2.8, P: 205.0, α_W: 9.6
590	500	α_W: 6.6, P: 80.5
550	200	α_W: 5.1, P: 55.5
510	undetectable	α_B: 310.0, α_W: 852.0, P: 896.0
470	200	α_B: 216.0
430	20	α_B: 130.0

Table 6.12: Comparison of the estimated transformation start time from the dilation curve and predicted start time by the model.

Nevertheless, many features revealed from the experimental work are consistent with the predictions by the model. Displacive transformation occurs at a temperature as high as ~ 600 °C. The dilation curve can hardly show any transformation at 510 °C, which is also strongly supported by the long incubation time at this temperature by the model. As the temperature moves from 510 to 430 °C, average hardness decreases which may suggest more bainite and less martensite in the microstructure, though the accurate numbers of volume fractions of these phases may be hard to estimate using a optical microscopy. This is supported by the T_0 concept in the model that the maximum volume fraction of bainite decreases with rising temperature (Fig. 6.14).
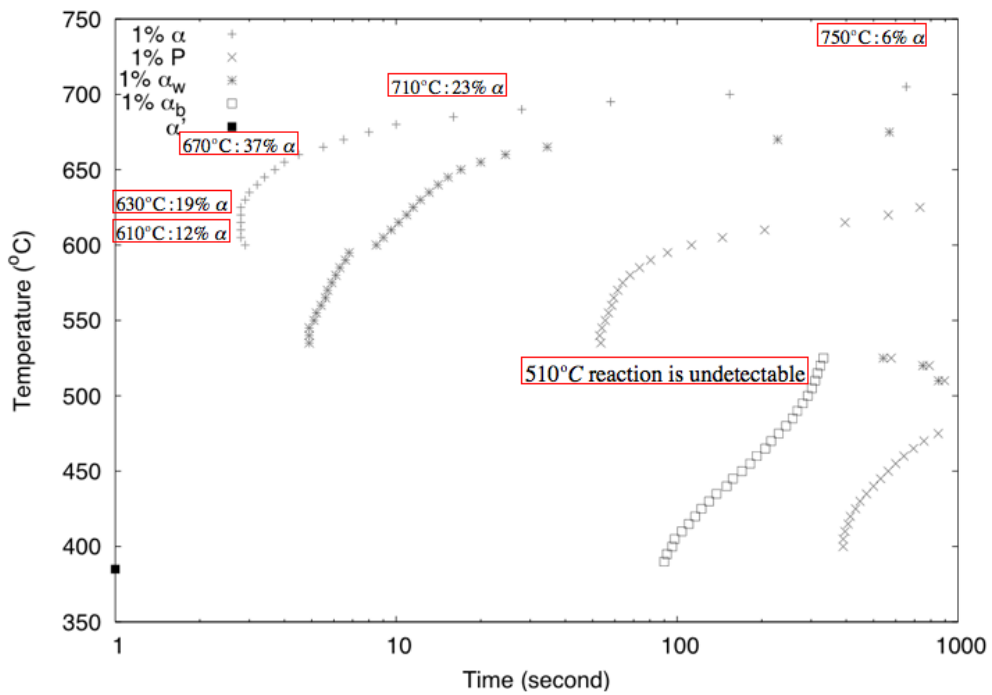
Figure 6.14: The data in the red-framed boxes are experimental results. Time-temperature transformation diagram predicted by theory at current work.

6.6 Comparison against published Isothermal Transformation Diagrams

The book "Atlas of Isothermal Transformation and Cooling Transformation Diagrams" by the American Society for Metals, contains numerous time-temperature transformation (TTT) diagrams for a variety of steels [72]. Two carbon steels, two nickel-chromium steels and two silicon steels were selected for comparison with the predictions of the model. The two carbon steels were chosen as a low demanding test of the model. The two Ni-Cr steels were selected because there is a clear separation between the reconstructive and displacive transformations. The two silicon containing steels were included as silicon would be expected to have a pronounced effect on carbide formation. All six steels were fully austenitic prior to cooling.

The solid lines in the Fig. 6.15, 6.16 and 6.17 represent the transformation start and end times of the experimental results and the points are the predictions. To represent the transformation start time in the calculations, it was selected when 1 % of austenite had transformed. To help to see the reaction speed, the times when 10 % and 40 % of austenite had transformed were included as well.

There are a few key observations in the six comparisons of isothermal transformation diagrams. First, the transformation of allotriomorphic ferrite and pearlite agree well with the experiments in the two carbon steels and the silicon containing steels, but overpredict the rate of formation in the Ni-Cr steels. As such it is believed that the model may only be effective in the prediction of allotriomorphic ferrite over a limited composition range.

Second, for the nickel-chromium steels, the model has successfully reproduced the separation of the two 'C' curves. But the positions of the points of 10% and 40% transformations suggest Widmanstätten ferrite may form too fast. This could explain the discrepancy of bainite data observed in many predictions at the previous sections, as Widmanstätten ferrite competes with bainite with resources and nucleation sites.

Finally, the shape of the predicted transformation contours of bainite are different from that of measurements. Bainite tends to form earlier at lower temperatures in the model. The reasons may due to a larger driving force and increasing volume fraction allowed by the T_0' mechanism at lower transformation temperature. For

the silicon steels, the bainite transformation start time seems overvalued in the model.
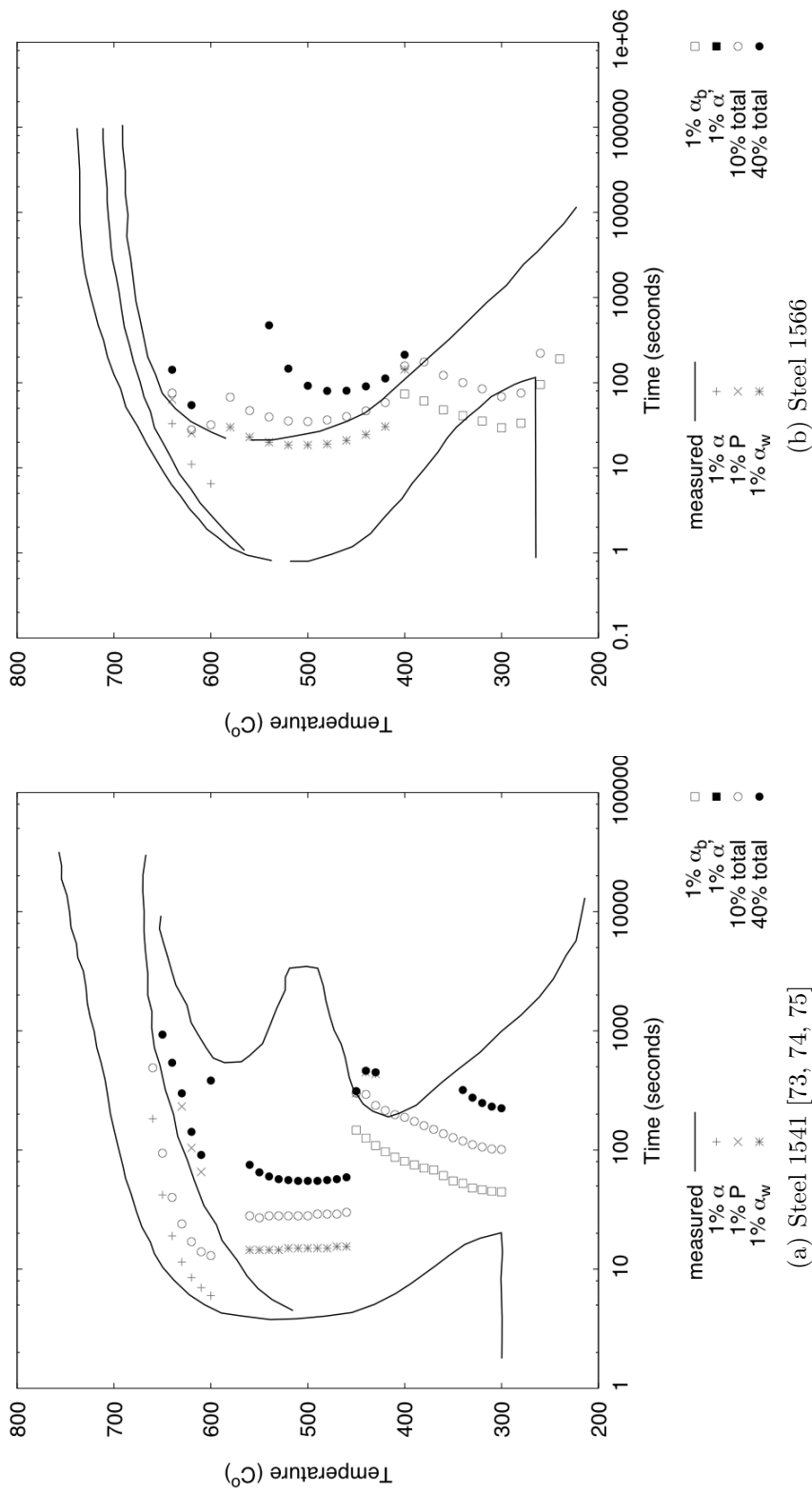
(a) Steel 1541 [73, 74, 75]

(b) Steel 1566

Figure 6.15: (a) Steel 1541 has composition (wt %) 0.43 C, 0.23 Si, 1.57 Mn, 0.2 Ni, 0.07 Mo, 0.12 Cr and 0.0003 V. The austenite grain size is 20.0 μm. (b) Steel 1566 has composition (wt %) 0.64 C, 0.0 Si, 1.13 Mn, 0.0 Ni, 0.0 Mo, 0.0 Cr and 0.0003 V. The austenite grain size is 28.0 μm.
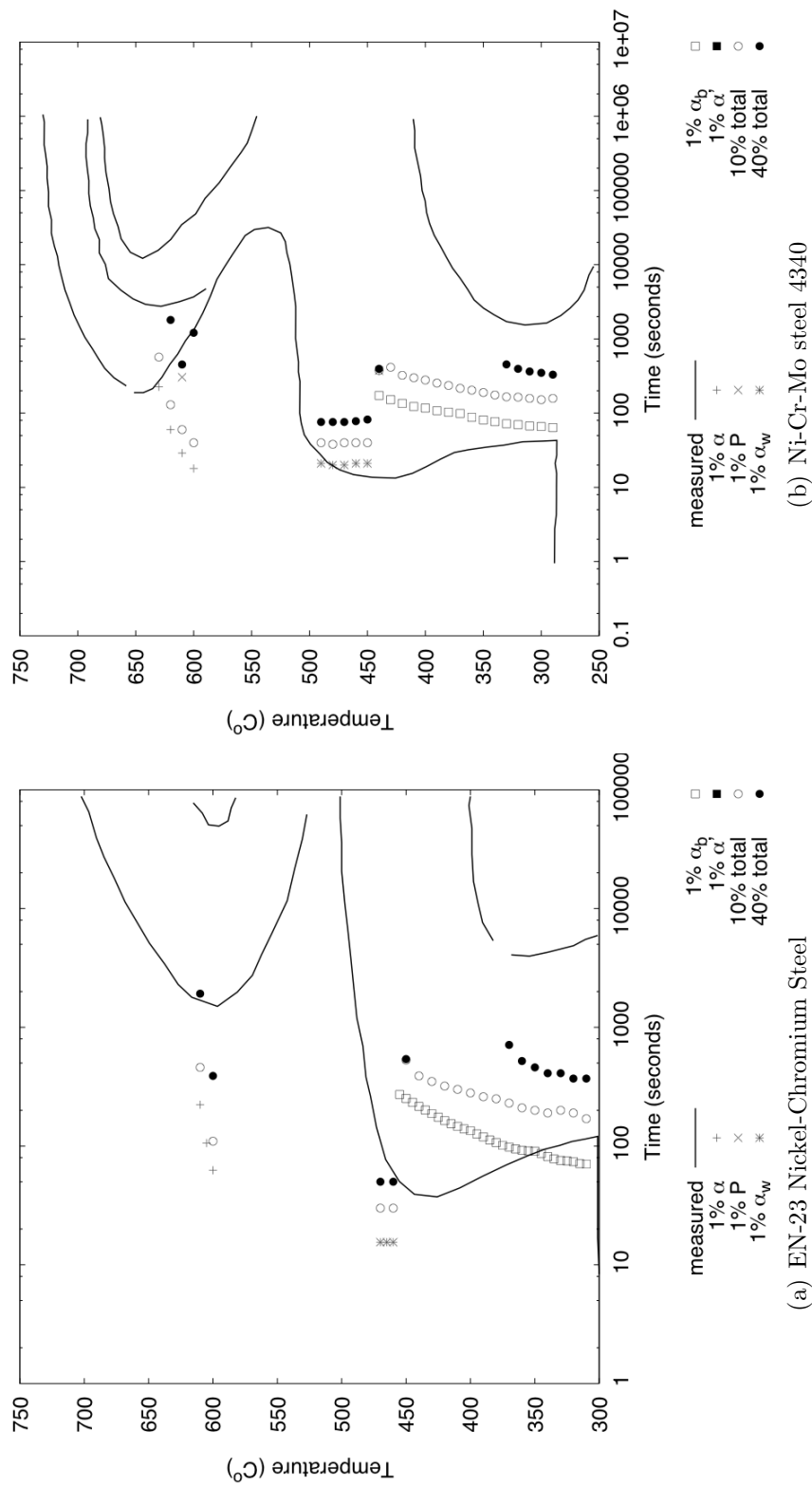
(a) EN-23 Nickel-Chromium Steel

(b) Ni-Cr-Mo steel 4340

Figure 6.16: (a) The Ni-Cr steel has composition 0.33 C, 0.23 Si, 0.57 Mn, 3.26 Ni, 0.09 Mo, 0.85 Cr and 0.0003 V. The austenite grain size is 14.14 μm. (b) the Ni-Cr-Mo steel has composition 0.42 C, 0.0 Si, 0.78 Mn, 1.79 Ni, 0.33 Mo, 0.8 Cr and 0.0003 V. The austenite grain size is 28.0 μm.

(a) Silicon Steel 0.18C-0.7Si-1Ni

(b) Silicon Steel 0.54C-1.3Si
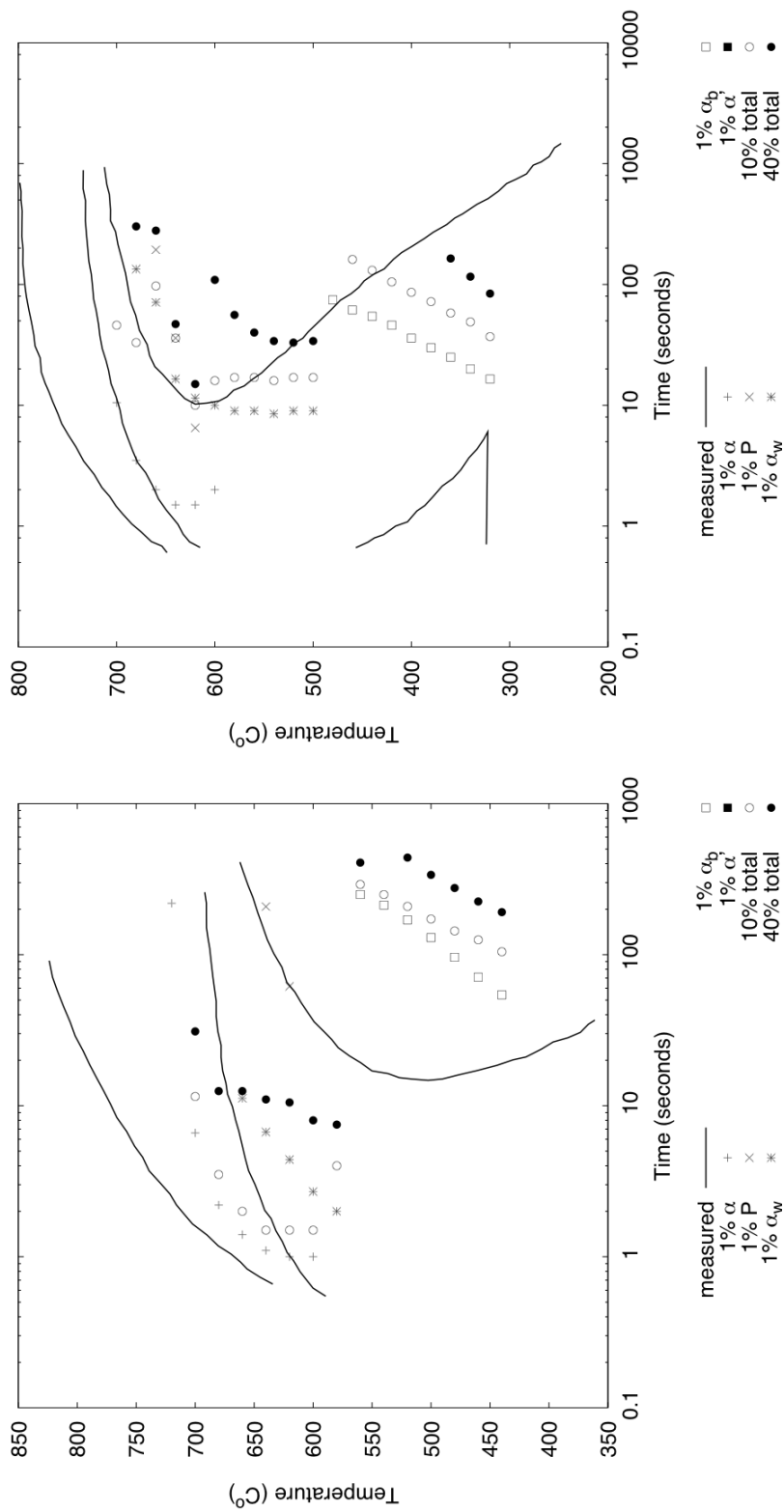
Figure 6.17: (a) The Si steel has composition 0.18 C, 0.71 Si, 0.75 Mn, 1.07 Ni, 0.0 Mo, 0.0 Cr and 0.0003 V. The austenite grain size is 14.14 μm. (b) The Si steel has composition 0.54 C, 1.27 Si, 0.23 Mn, 0.0 Ni, 0.0 Mo, 0.05 Cr and 0.0003 V. The austenite grain size is 57 μm.

102
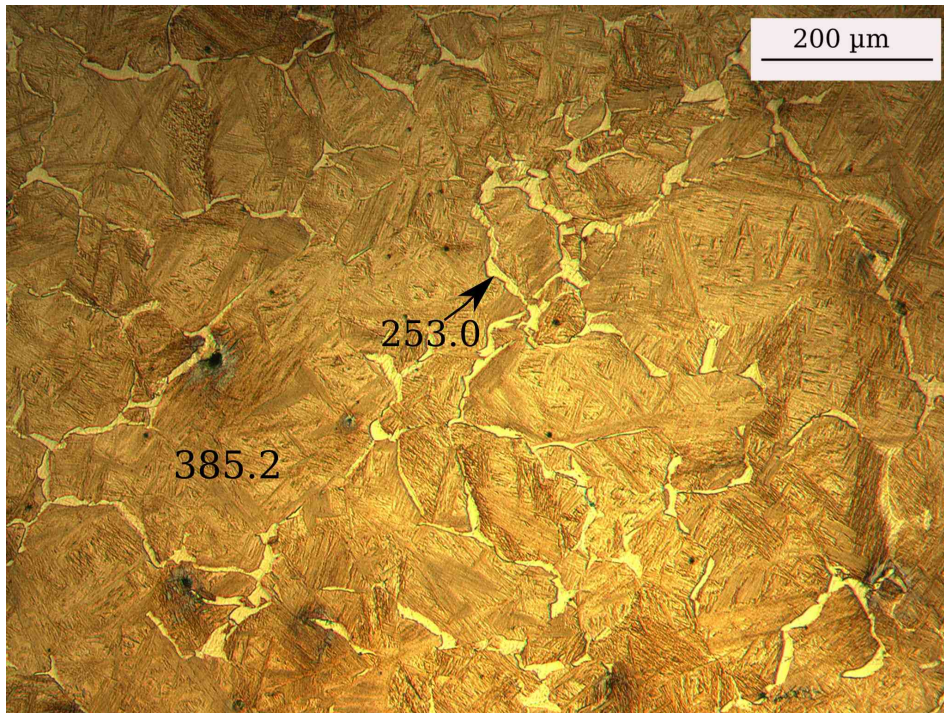
Figure 6.18: Optical micrograph after isothermal swell at 750 °C. The number(s) on the figure is (are) the hardness H_v of the area(s).
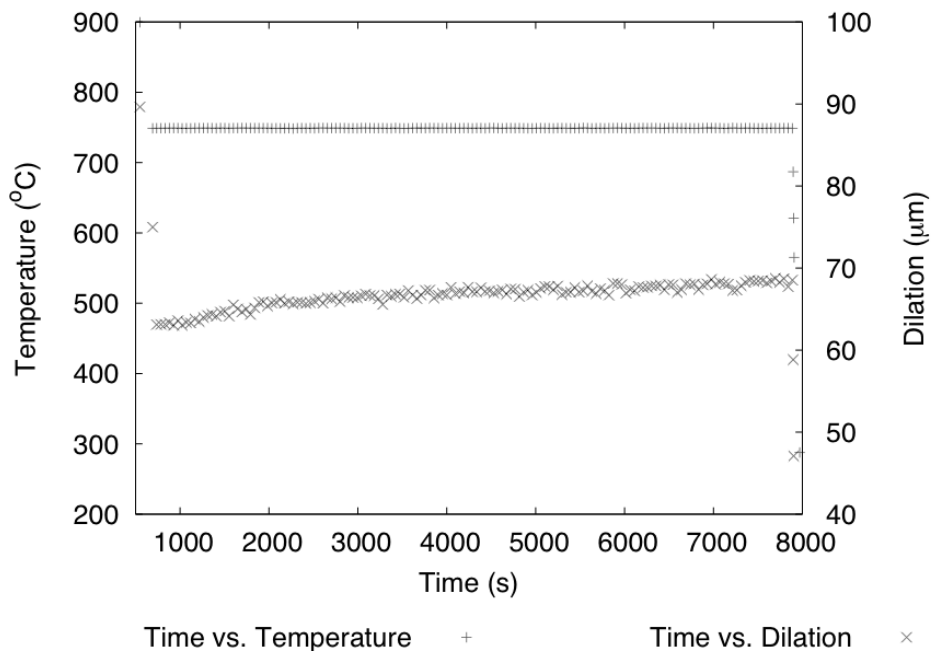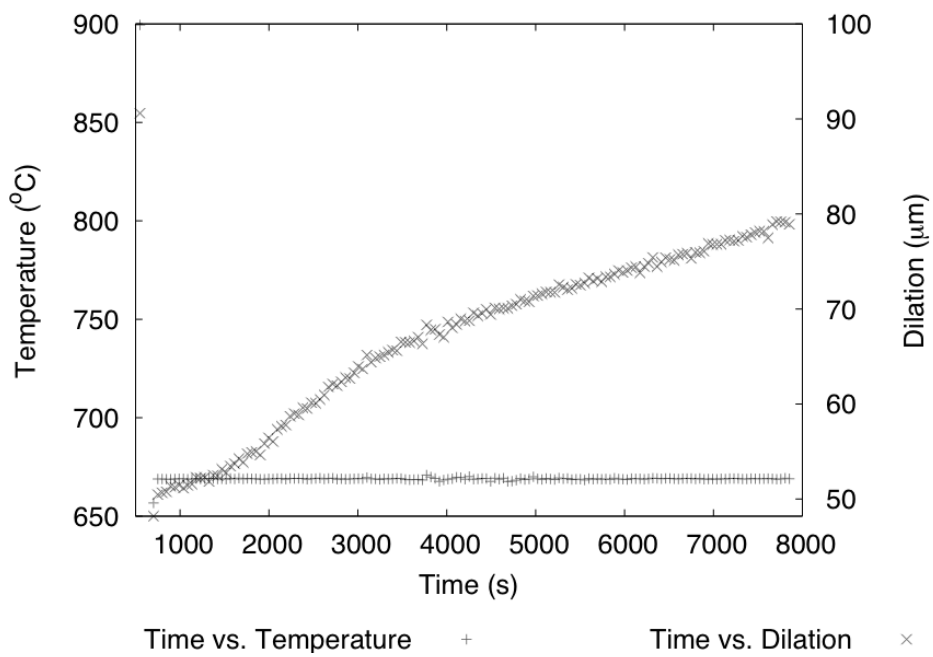

Figure 6.19: Plot of dilatometry data for the sample isothermally transformed for 2 h at 750 °C.
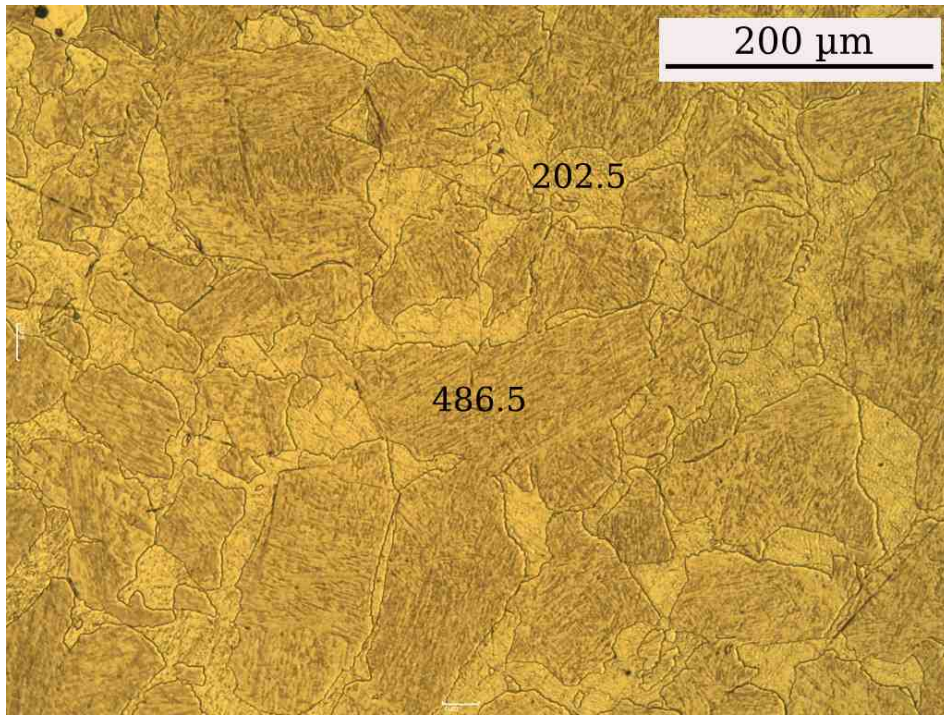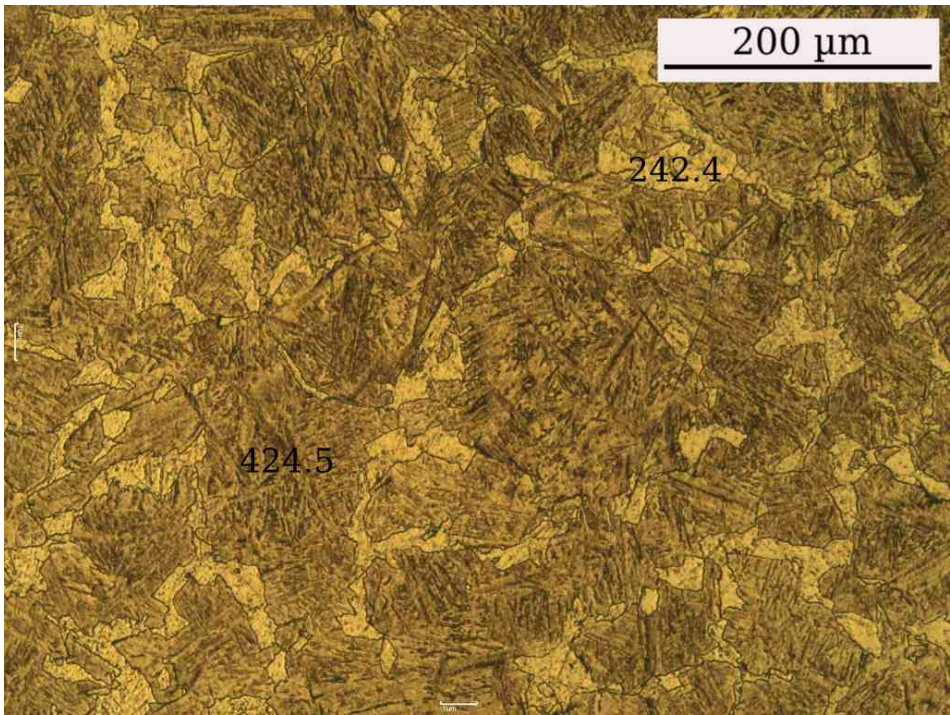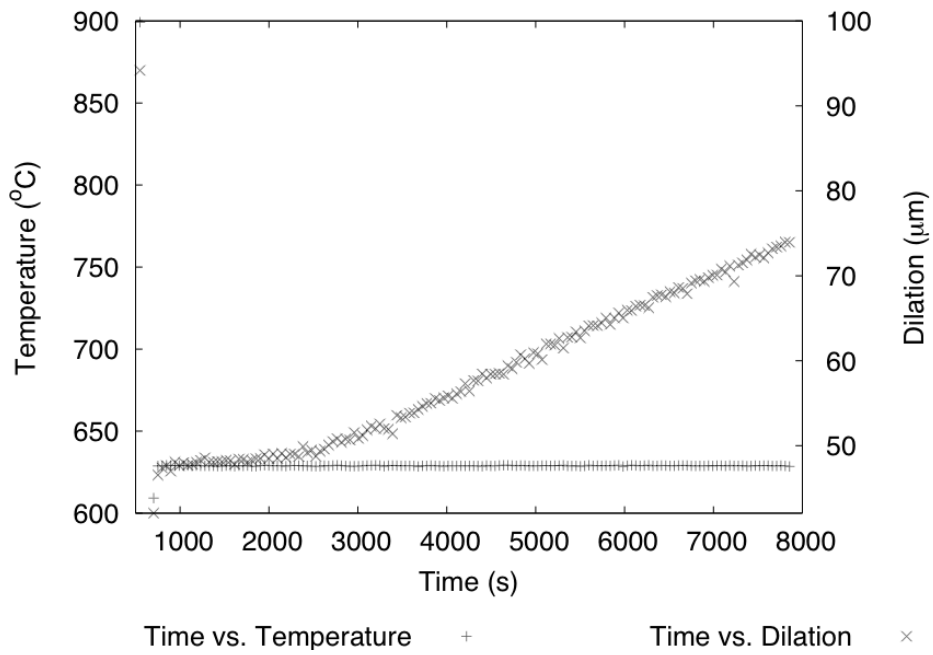
Figure 6.20: Optical micrograph after isothermal swell at 710 °C. The number(s) on the figure is (are) the hardness H_v of the area(s).
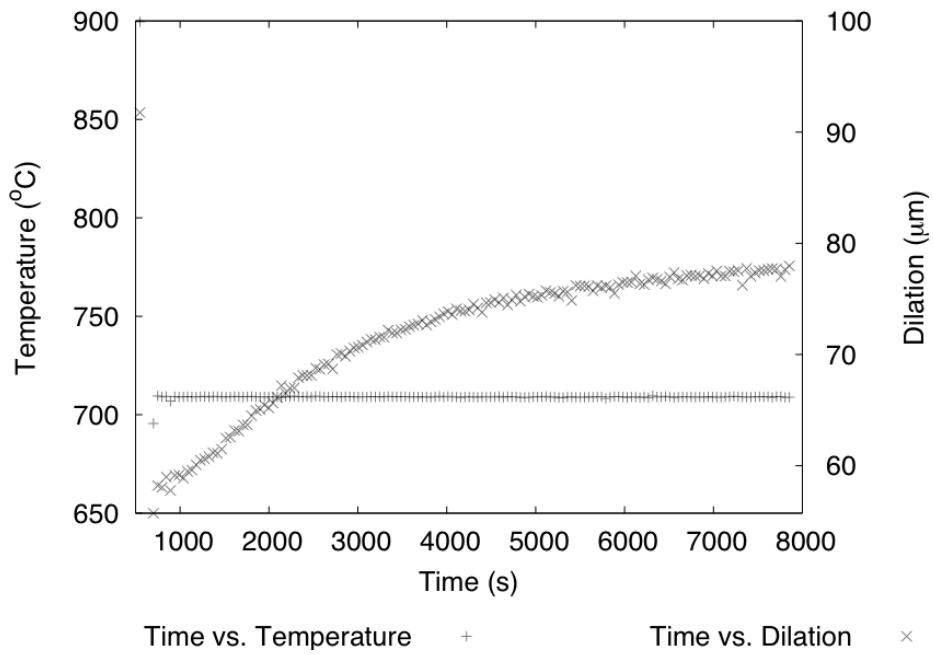
Figure 6.21: Plot of dilatometry data for the sample isothermally transformed for 2 h at 710 °C.
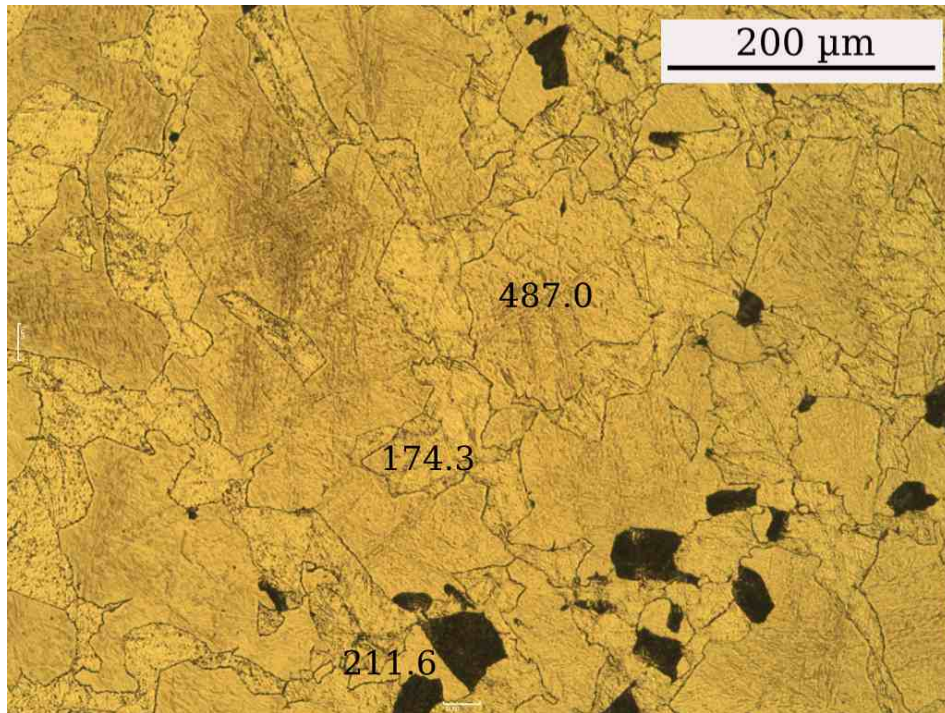
Figure 6.22: Optical micrograph after isothermal swell at 670 °C. The number(s) on the figure is (are) the hardness H_v of the area(s).

Figure 6.23: Plot of dilatometry data for the sample isothermally transformed for 2 h at 670 °C.
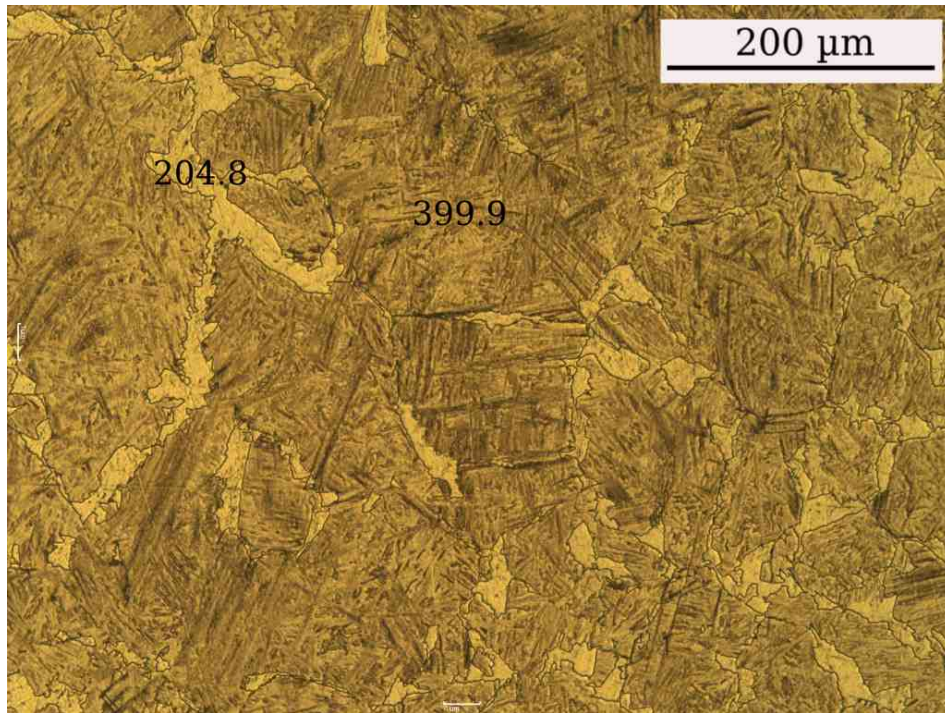
Figure 6.24: Optical micrograph after isothermal swell at 630 °C. The number(s) on the figure is (are) the hardness H_v of the area(s).
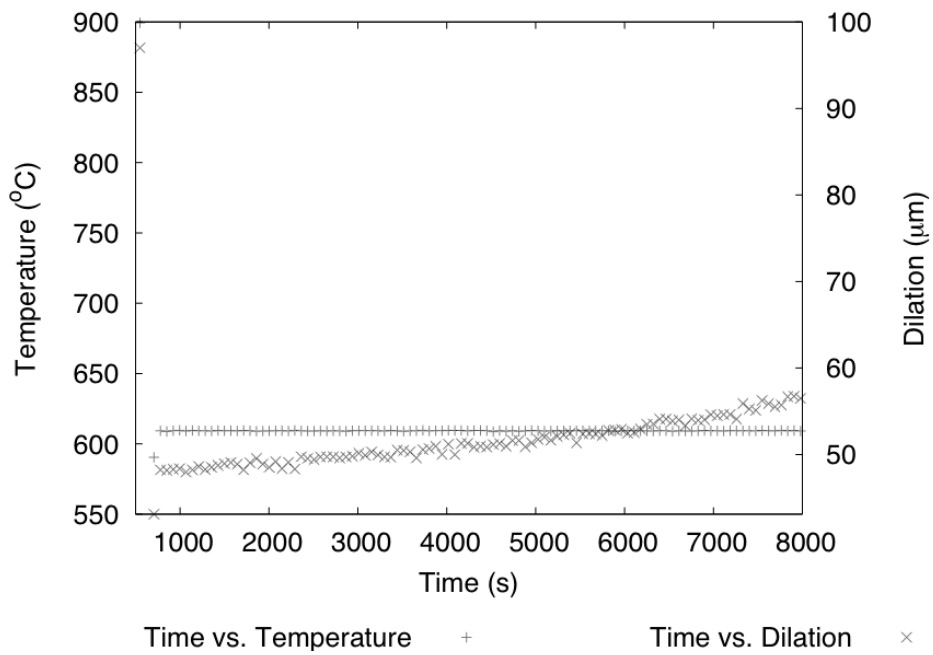

Figure 6.25: Plot of dilatometry data for the sample isothermally transformed for 2 h at 630 °C.

Figure 6.26: Optical micrograph after isothermal swell at 610 °C. The number(s) on the figure is (are) the hardness H_v of the area(s).

Figure 6.27: Plot of dilatometry data for the sample isothermally transformed for 2 h at 610 °C.
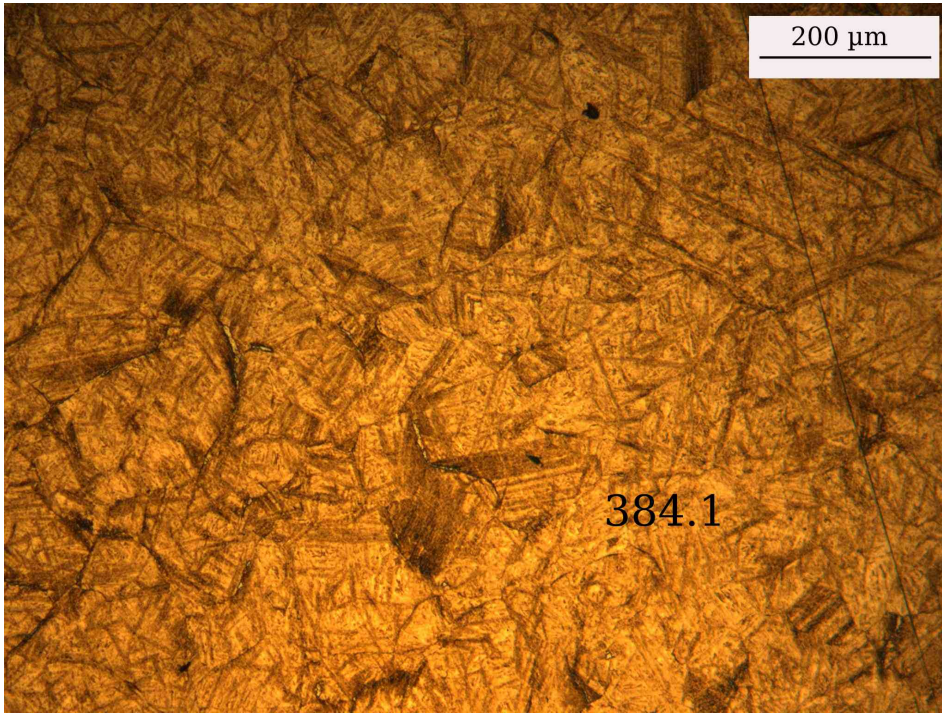
Figure 6.28: Optical micrograph after isothermal swell at 590 °C. The number(s) on the figure is (are) the hardness H_v of the area(s).
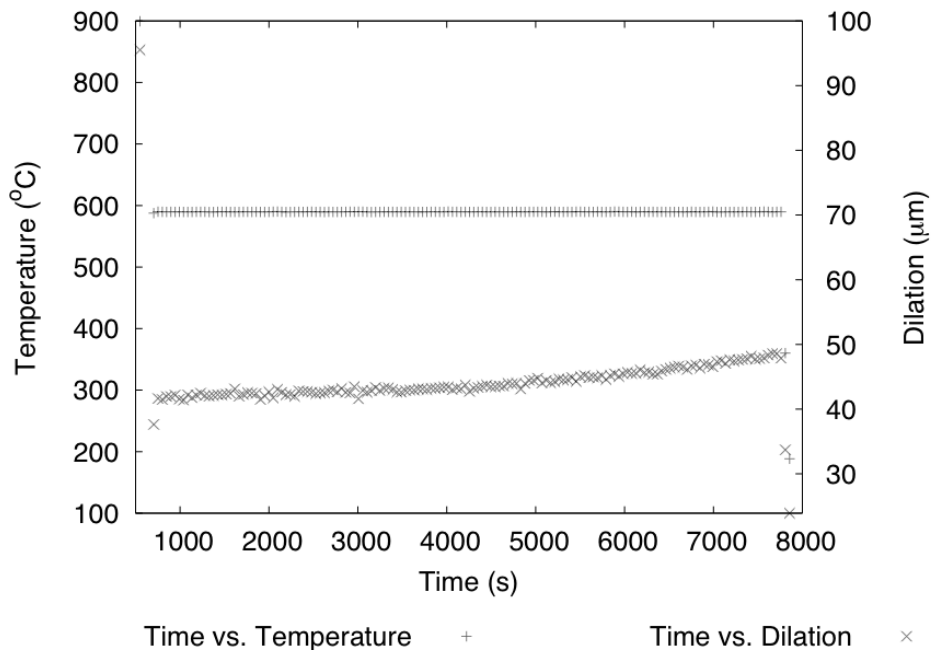

Figure 6.29: Plot of dilatometry data for the sample isothermally transformed for 2 h at 590 °C.
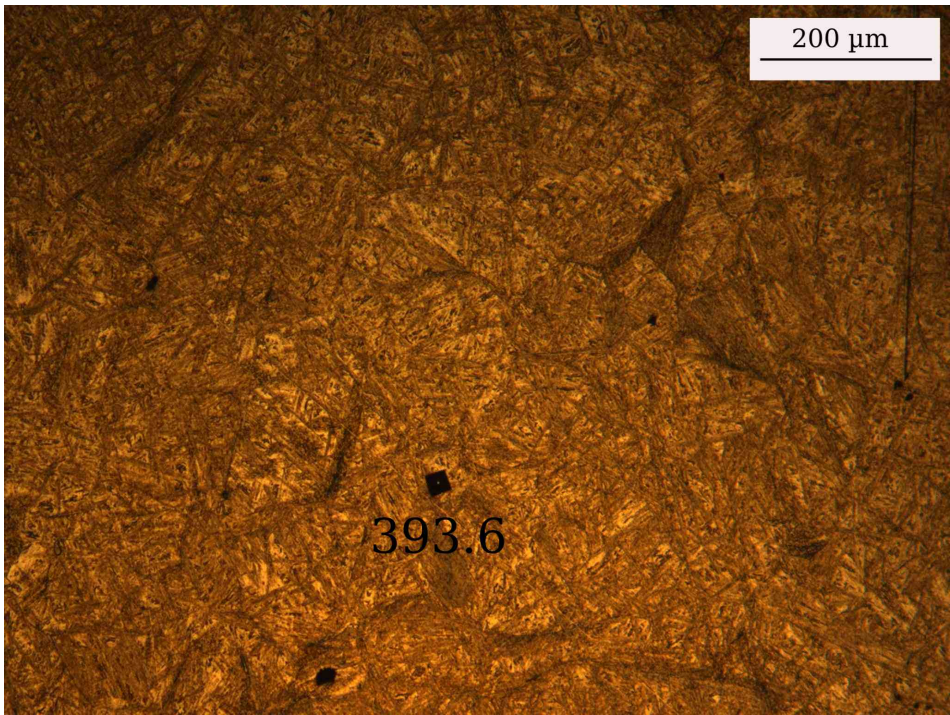
Figure 6.30: Optical micrograph after isothermal swell at 550 °C. The number(s) on the figure is (are) the hardness H_v of the area(s).

393.6

Figure 6.31: Plot of dilatometry data for the sample isothermally transformed for 2 h at 550 °C.

Figure 6.32: Optical micrograph after isothermal swell at 510 °C. The number(s) on the figure is (are) the hardness H_v of the area(s).

407.4

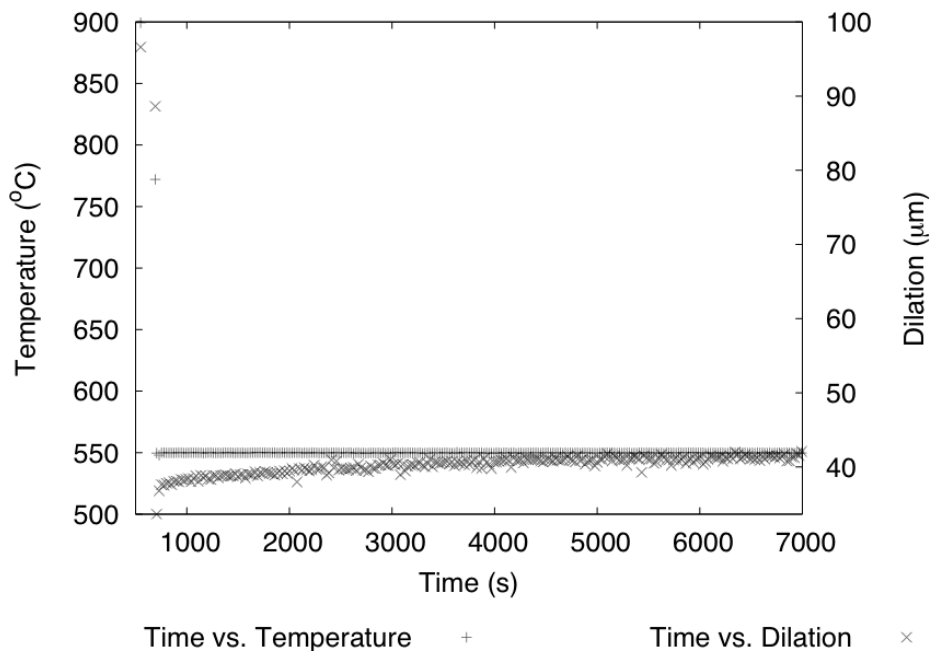Time vs. Temperature $+$ Time vs. Dilation $\times$

Figure 6.33: Plot of dilatometry data for the sample isothermally transformed for 2 h at 510 °C.

Figure 6.34: Optical micrograph after isothermal swell at 470 °C. The number(s) on the figure is (are) the hardness H_v of the area(s).

383.1

Figure 6.35: Plot of dilatometry data for the sample isothermally transformed for 2 h at 470 °C.
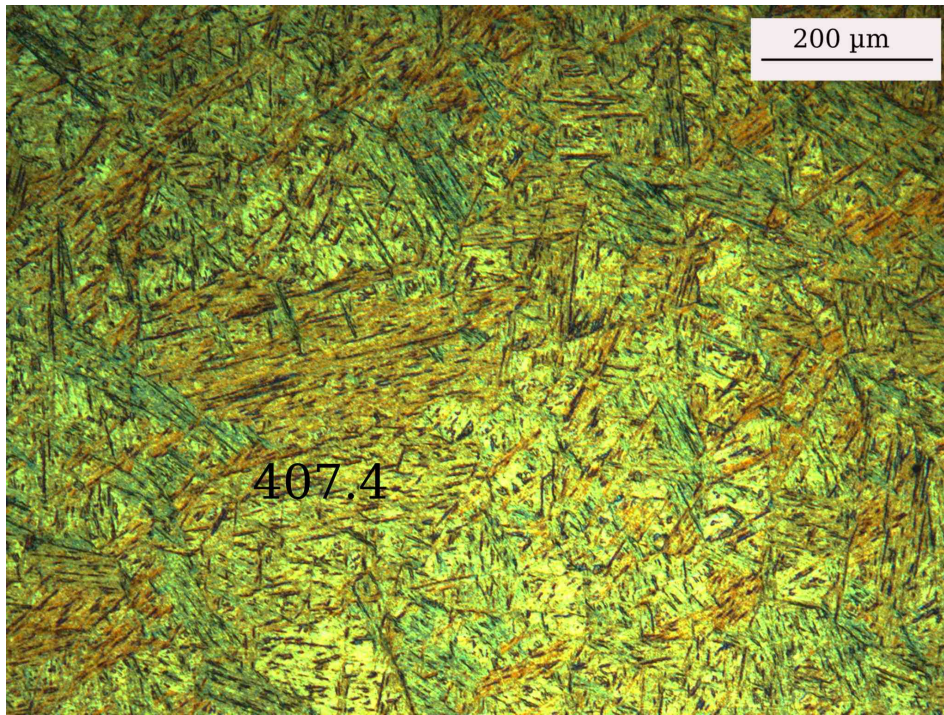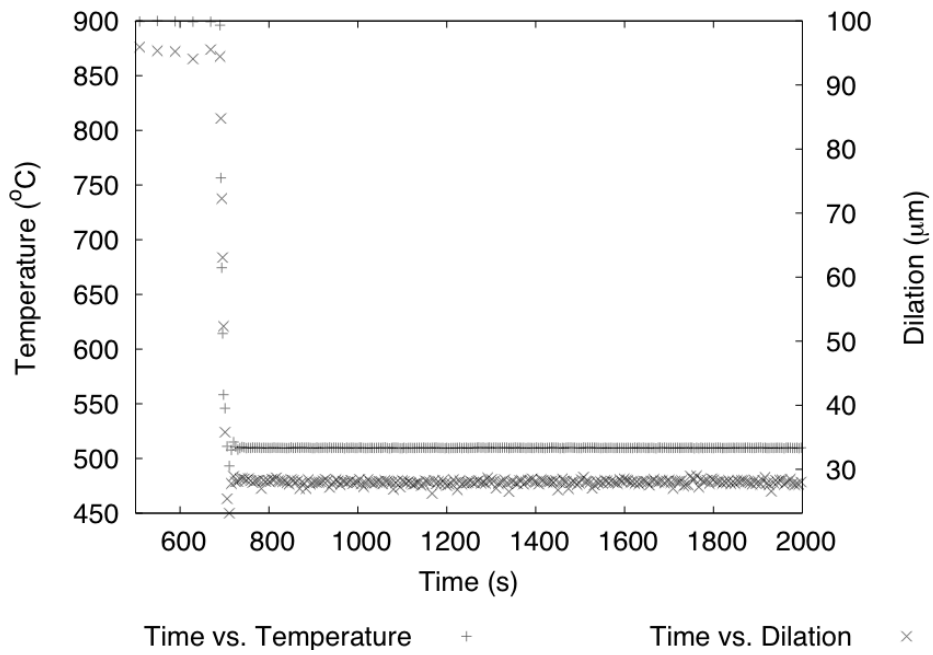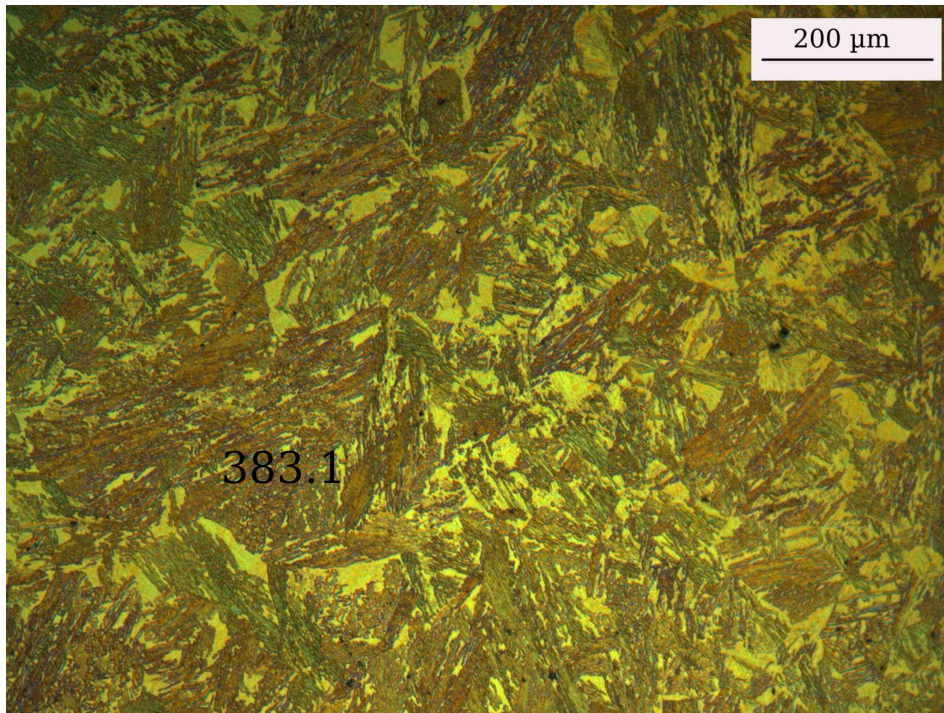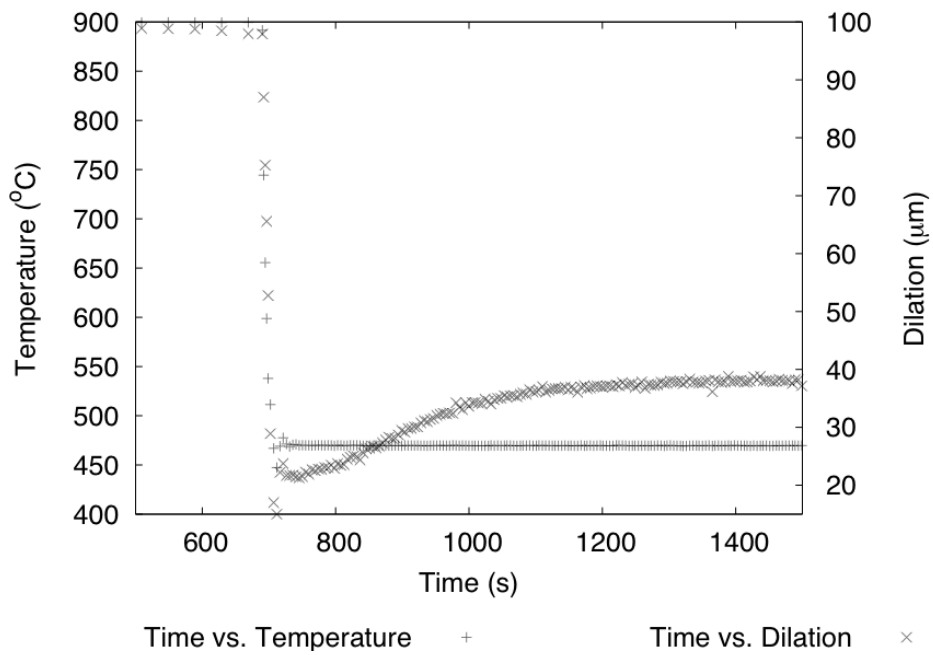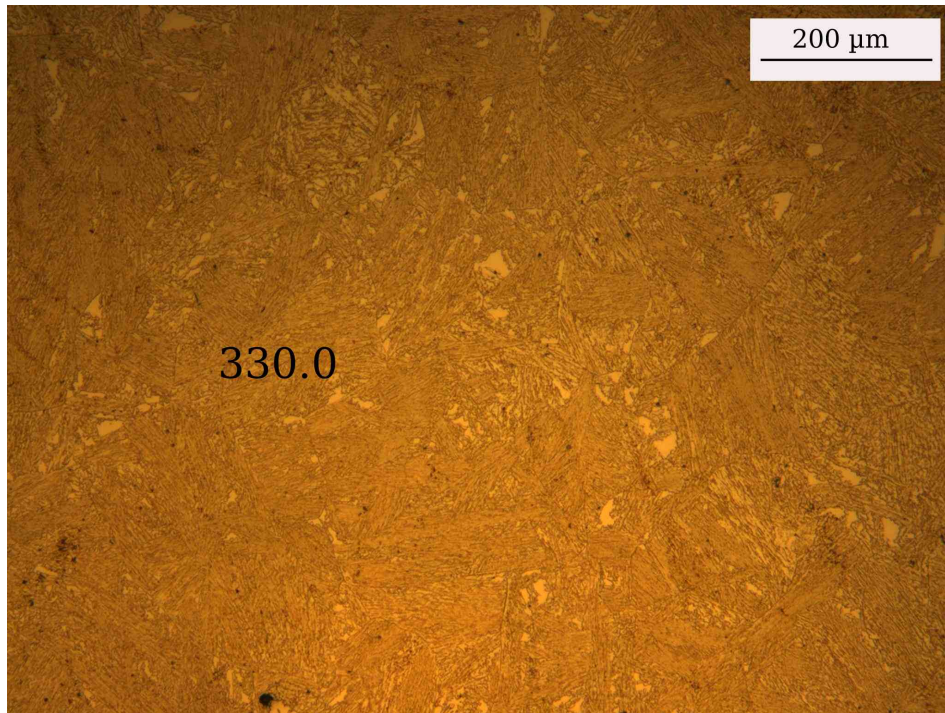
Figure 6.36: Optical micrograph after isothermal swell at 430 °C. The number(s) on the figure is (are) the hardness H_v of the area(s).
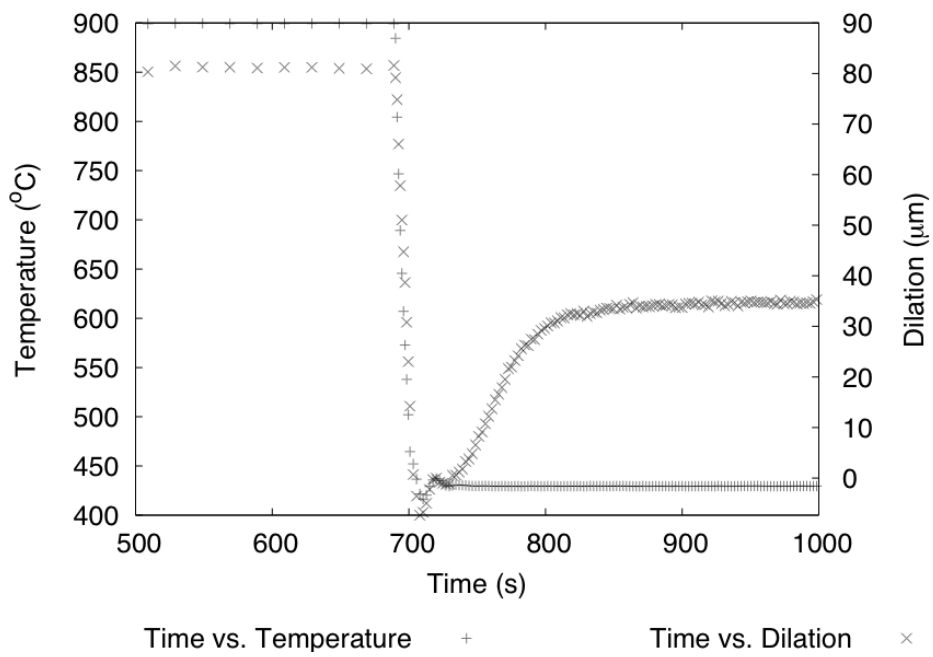

Figure 6.37: Plot of dilatometry data for the sample isothermally transformed for 2 h at 430 °C.

Chapter 7

Conclusion

Bainite has been integrated into a single modelling scheme, which previously included only higher temperature transformation products of austenite [76]. The model allows the temporal evolution of the microstructure in steels to be revealed step by step during the simulation. The model can simulate cooling at constant rates, or isothermal transformation. It follows that the more useful CCT and TTT diagrams can also be produced.

The construction of the model has taken full account of the thermodynamics of transformations, instead of empirical equations, so the model should in principle generalise well. However, comparison with experiment suggests that, at present, the model will provide more reliable predictions over a limited composition range. The suggested limits of the input chemical compositions are listed on Tab. B.1. Many adjustable parameters used in the model are listed on Tab. B.2, which could be fine-tuned for a particular family of steels to achieve optimum performance.

The predictions of the model have been tested systematically, and it was found to successfully capture well-known phenomena. The model has, to some extent, also been validated against both published experimental data and experiments conducted in this work. As the growth rate of one phase can affect the reaction rate of the other phases, the accuracy of the predictions of one phase may be further improved by the refinement of the other phase.

The output of the model is rich in information. Much of it, such as the driving forces etc., is not easy to access experimentally. A calculation of a CCT diagram

takes about 2 hours on a computer with a 2 GHz CPU. Compared with a typical CCT measurement, which may require days or even weeks of work, the model can potentially benefit the development of new steels. The model is ready to be used by other applications, such as the modelling of segregation.

7.1 Further work

Evidently, the rapid growth rate of Widmanstätten ferrite may cause the discrepancy observed between the bainite predictions and experiments. Further improvement of the accuracy of bainite may lie in the improvement of the other phases, as they all compete for the same resources.

The predicted transformation temperature of allotriomorphic ferrite and pearlite can extend well below 600 °C in some calculations. This needs to be validated by experiments. The prediction of Widmanstätten ferrite at high temperatures above 700 °C in some steels also requires confirmation.

The incorporation of other alloying elements can be an important development of the model. The code for boron is incomplete, in the sense that the interaction with titanium and nitrogen have not been taken into account. The input at the moment assumes soluble boron.

Systematic tests are needed to determine the relative strength of many adjustable parameters, listed on Tab. B.2, on the volume fractions of transformed products.

The code for inclusion nucleated transformations have been included in the source code, but are inactive in the model. Further validation is required before the calculations of inclusion nucleated transformations can be successfully integrated into the grain boundary nucleated transformations.

Appendix A

The Boron Effect

Boron has very low solubility in austenite, but its effect on transformations is pronounced. Often ≈ 0.002 wt % boron concentration is sufficient in typical commercial steels to have an impact on the ferrite formation. As boron reacts with nitrogen to form boron nitride, BN, the dissolved active boron can be affected by the presence of nitrogen. Comprehensive reviews on the effect of boron can be found in literature [77, 78].

To investigate the effect of boron, two samples were prepared by Swiss Steel AG, with chemical compositions listed in Tab. A.1. One of these had a deliberate addition of boron.

	C	Si	Mn	Ni	Mo	Cr	V	B
No B	0.14	1.2	1.46	0.06	0.29	1.21	0.0	0.0
With B	0.14	1.23	1.5	0.06	0.3	1.22	0.0	0.003

Table A.1: The chemical composition (wt %) of the two steels.

Dilatometry experiment

Samples were prepared as described previously in Section 6.5, for studies using a thermo-mechanical simulator, also described previously.

In each test, the sample was heated up to 900 °C, and held there for 30 min, then quenched using helium down to a pre-determined isothermal temperature, and held for 2 h. Experiments were repeated at each isothermal temperature to verify the results.

Discussion of the results

The data from the dilatometry experiments are plotted in Fig. A.1. From all of these data, it can be seen that boron additions delay the microstructural changes that lead to the dilatation observed.

Boron is believed to reduce the interfacial energy of austenite grain boundaries [79, 78]. This in turn deters the nucleation of ferrite, as heterogeneous nucleation benefits from the elimination of austenite grain boundaries. From the modelling point of view, this is pragmatically equivalent to a boron-induced increase in the α/γ interface energy.

An attempt has been made to add boron into the model. The predictions by the model are consistent with the trends suggested by experiments (Fig. A.2). To further the development, a comprehensive model about the chemical interaction between boron, nitrogen and titanium is required.
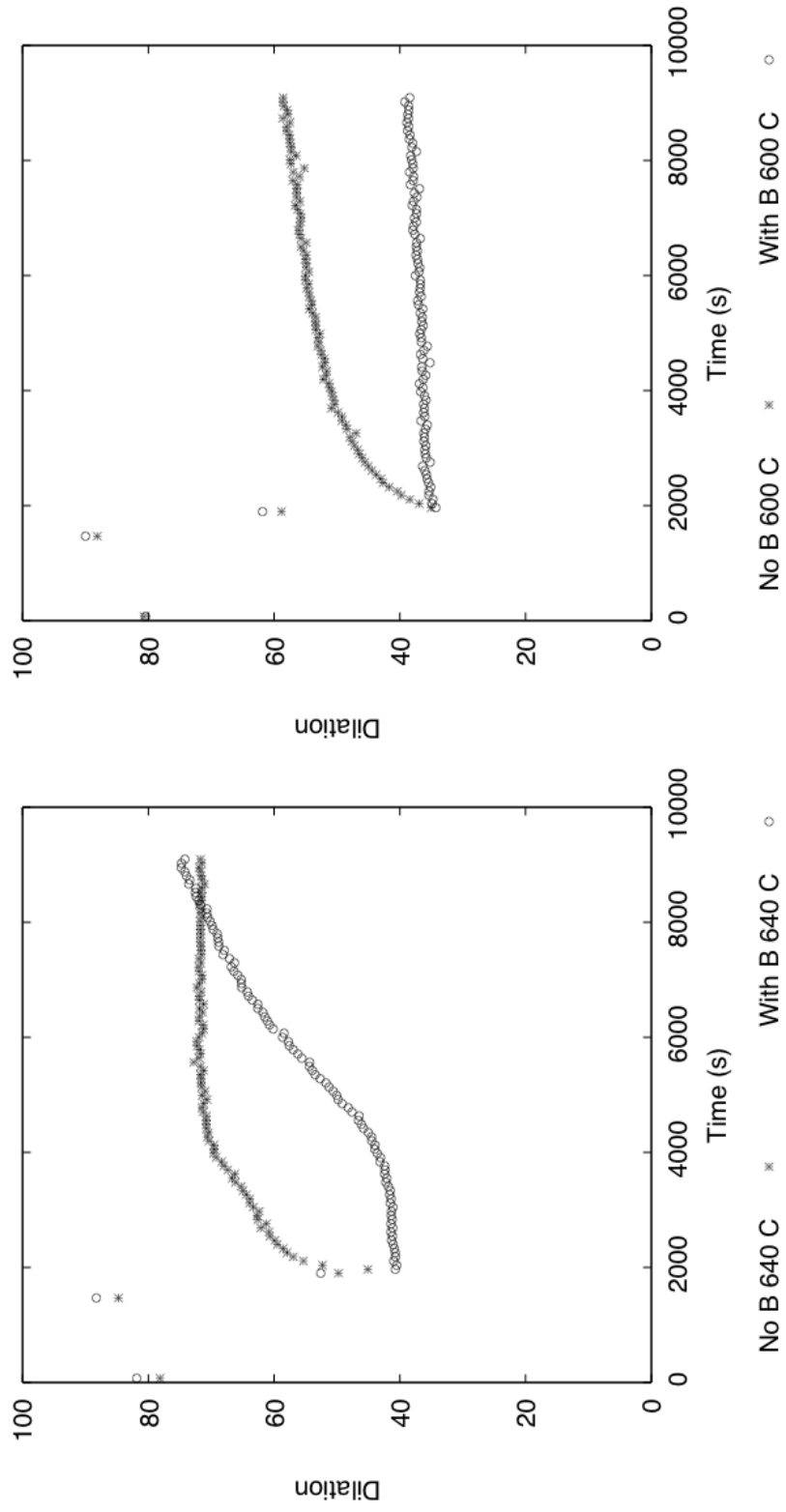
Figure A.1: The experimental data of dilation in the isothermal transformations at 640 °C and 600 °C. Both experiments confirm that the ferrite transformation start time is massively delayed in the presence of boron.
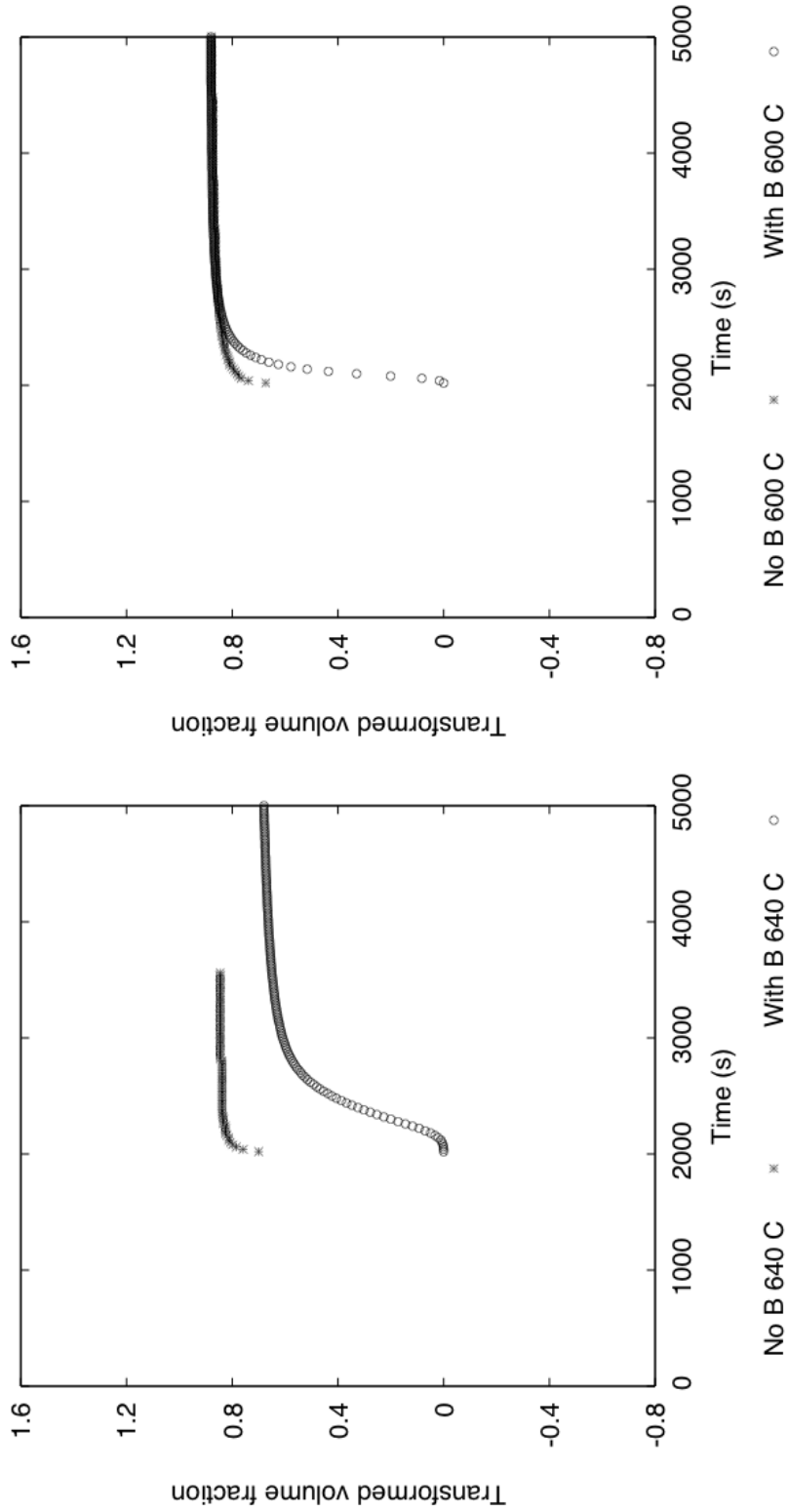
117

Figure A.2: The predicted data of volume fraction of ferrite vs. time in the isothermal transformations at 640 °C and 600 °C. The volume fraction of ferrite should not be a linear function of dilation change for the reason discussed in the previous chapter.

118

Appendix B

Documentation of 'STRUCTURE' Program

A program has been created for the model called STRUCTURE.

Purpose of code

To model simultaneous transformations from austenite to allotriomorphic ferrite, pearlite, Widmanstatten ferrite and bainite nucleated at austenite grain boundaries.

Parameters descriptions

The input parameters are chemical compositions, austenite grain size and temperature scheme. The limit of the chemical compositions are listed in Tab. B.1.

	C	Si	Mn	Ni	Mo	Cr	V
lower limit	0.08	0.0	1.0×10^{-6}	0.0	0.0	0.0	0.0
upper limit	0.8	2.5	3.5	4.5	1.5	3.5	1.5

Table B.1: The limits of the chemical compositions (wt %) that can be predicted by the model.

The adjustable parameters of the program are listed in Tab. B.2.

α/γ interface energy	0.022 J m^{-2}
Activation energy for an atom to cross the α/γ interface	200 kJ mol^{-1}
Factor of energy reduction due to heterogeneous nucleation	0.333
Fraction of effective boundary sites	1.0×10^{-8}
The ratio of the nucleation rate of α to P	1.0×10^{-6}
The shape ratio of α	3.0
The shape ratio of P	1.0
The shape ratio of α_W	0.05
Length of a α_B sub-unit below 528 Kelvin	1.0×10^{-7} m
Intersection area of a α_B sub-unit below 528 Kelvin	2.0×10^{-16} m^2

Table B.2: The adjustable parameters of the program.

Outputs information

The standard five output data are continuous cooling diagram, isothermal transformation diagram, Temperature-Time Transformation diagram (TTT), continuous cooling transformation diagram (CCT) and empirical TTT diagram.
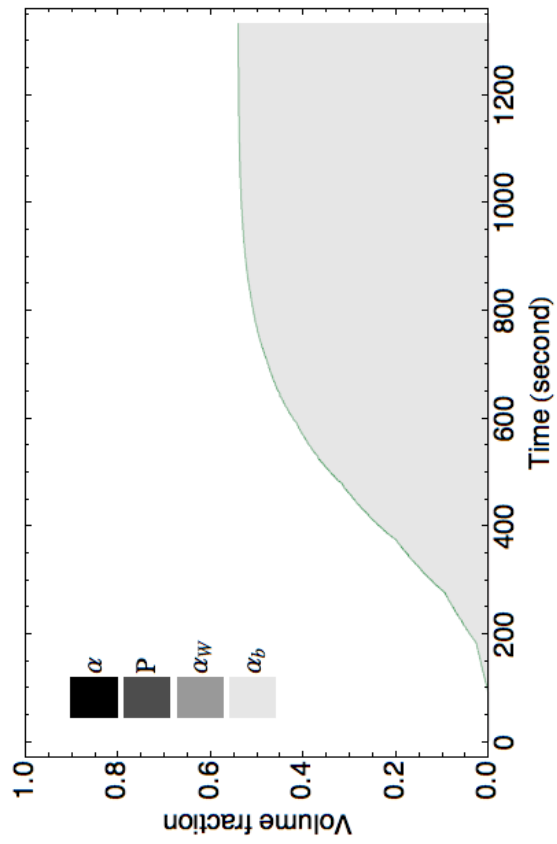
A steel developed in Swiss Steel AG will be used for the purpose of demonstration. Its chemical composition and grain size are listed (Tab. B.3).

C	Si	Mn	Ni	Mo	Cr	V	grain size / μm
0.23	0.96	1.56	0.08	0.14	1.53	0.0	30.0

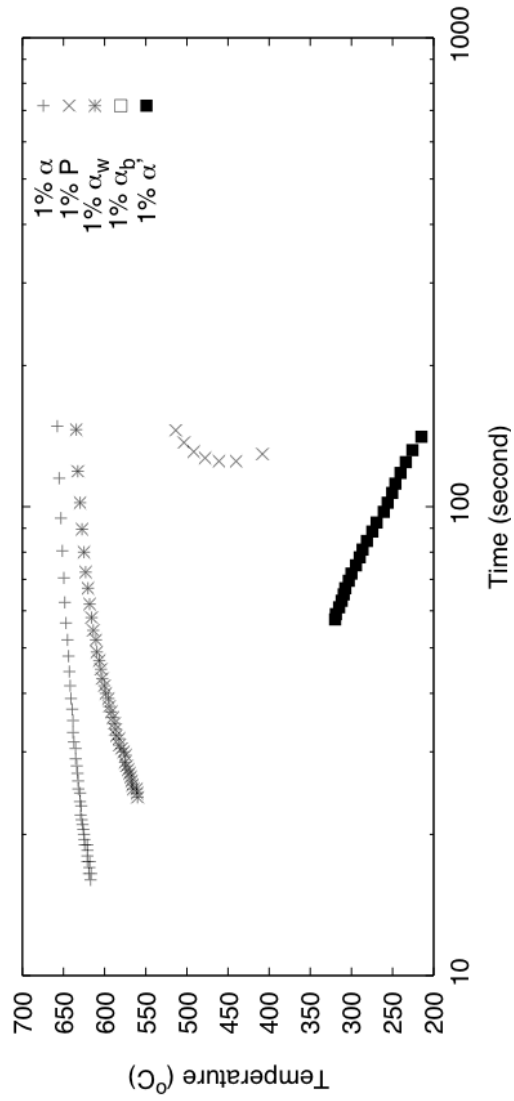Table B.3: The chemical composition (wt %) of the steel samples.
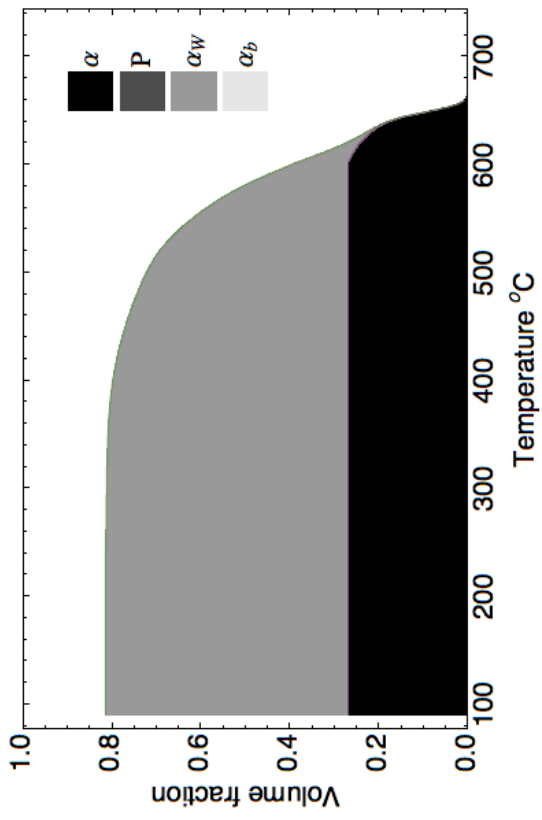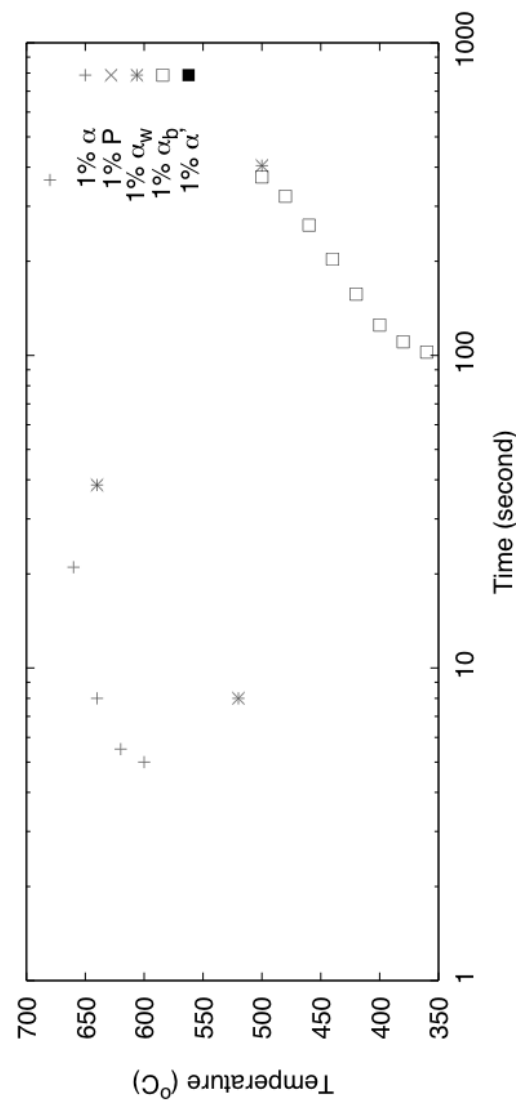
(a) Continuous cooling 60 K/min

(b) Isothermal 400 C

Figure B.1: Diagrams for isothermal and continuous cooling transformations.

(a) Continuous cooling transformation diagram

(b) Time-Temperature-Transformation diagram

Figure B.2:

122

The last diagram is an empirical TTT diagram theorised and verified by Bhadeshia [32]. The transformation start time for the displacive τ_{dis} and reconstructive τ_{rec} transformations are calculated using equations

$$\tau_{\text{dis}} = \exp \left\{ \frac{0.2432 \times 10^6}{RT} - 0.135 \times 10^3 + 20 \ln T - 5 \ln |\Delta G_m| \right\}$$

$$\tau_{\text{rec}} = \exp \left\{ \frac{0.6031 \times 10^6}{RT} - 0.1905 \times 10^3 + 20 \ln T - 4 \ln |\Delta G_m| \right\}$$

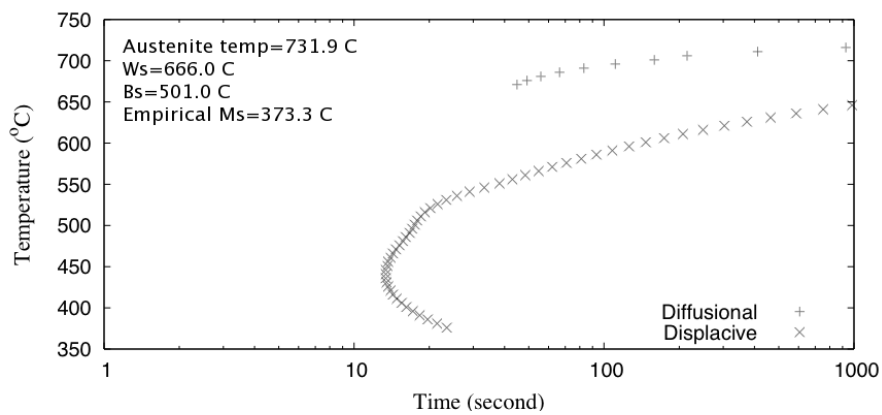where T is the temperature in Kelvin.

Figure B.3: TTT diagrams based on empirical equations. The Widmanstätten, bainite and martensite start temperature determined thermodynamically.

Logic Flow

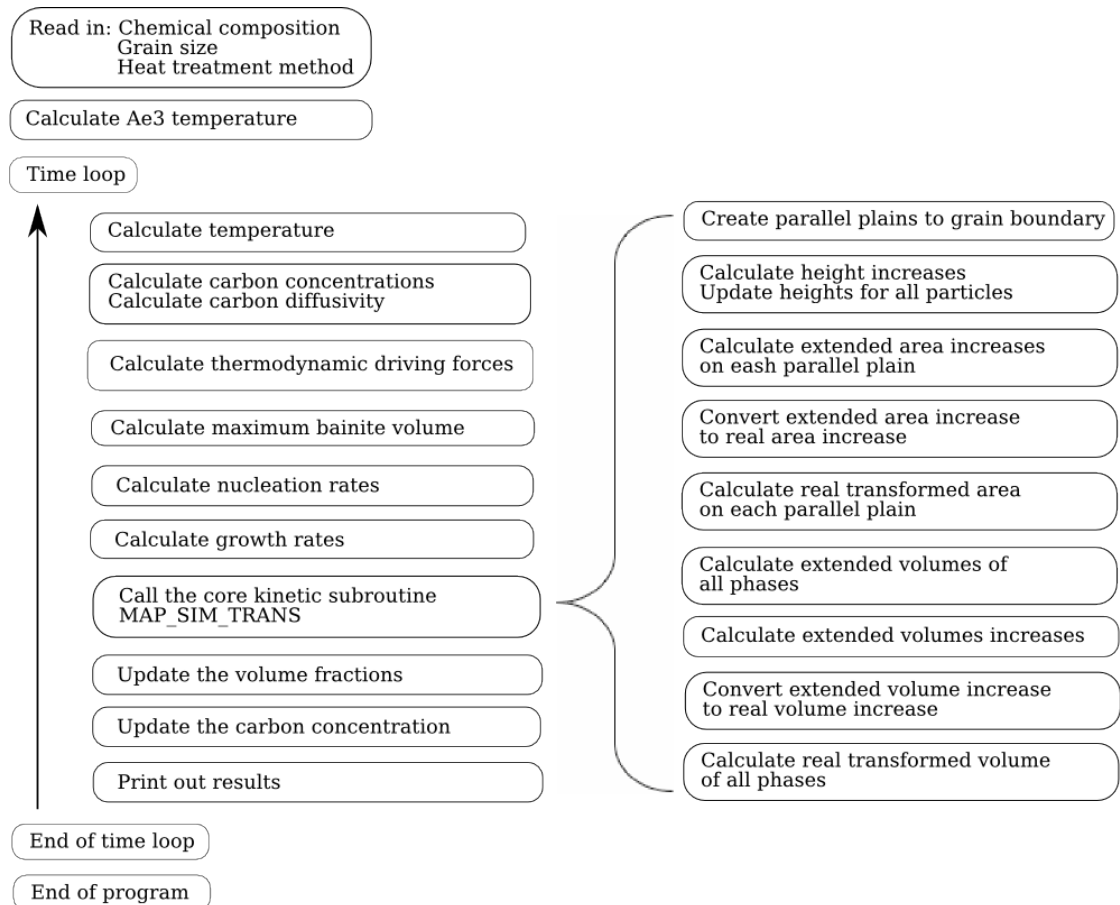The chart of logic flow of the program is presented in the Fig. B.4.

Figure B.4: The logic flow of the program.

References

[1] H. K. D. H. Bhadeshia and R. W. K. Honeycombe. *Steels: Microstructure and Properties*. Elsevier Ltd., 2006.

[2] J. W. Cahn. The kinetics of grain boundary nucleated reactions. *Acta Metallurgica*, 4:449–459, 1956.

[3] H. K. D. H. Bhadeshia. A rationalisation of shear transformations in steels. *Acta Metallurgica*, 29:1117–1130, 1981.

[4] H. K. D. H. Bhadeshia. *Bainite in steels*. Institute of Materials, London, 2nd edition, 2001.

[5] H. K. D. H. Bhadeshia. Mathematical models in materials science. *Materials Science and Technology*, 24:128–135, 2008.

[6] L. E. Svensson H. K. D. H. Bhadeshia and B. Gretoft. A model for the development of microstructure in low alloy steel (Fe-Mn-Si-C) weld deposits. *Acta Metallurgica*, 33:1271–1283, 1985.

[7] B. A. Thomson J. S. Kirkaldy and E. A. Baganis. Prediction of multicomponent equilibrium and transformation diagrams for low alloy steels. In D. V. Doane and J. S. Kirkaldy, editors, *Hardenability Concepts with Applications to Steels*, pages 82–125, Materials Park, Ohio, USA,, 1978. AIME, Warrendale PA.

[8] J. Seitsma P. J. van der Wolk, J. J. Wang and S. van der Zwaag. Modelling the continuous cooling transformation diagram of engineering steels using neural

networks - part I: phase regions. *Zeitschrift fur Metallkunde*, 93:1199–1207, 2002.

[9] T. Trzaska and L. A. Dobrzanski. Modelling of CCT diagrams for engineering and constructional steels. *Journal of Materials Processing Technology*, 192:504–510, 2007.

[10] M. Umemoto and I. Tamura. Computer simulation of isothermal transformation diagrams for steels. *Bulletin of the Japan Institute of Metals*, 22:497–504, 1985.

[11] A. H. Cottrell. *Dislocations and plastic flow in crystals.* Oxford University Press, Oxford, 1953.

[12] J. R. Lacher. The statistics of the hydrogen-palladium system. *Mathematical Proceedings of the Cambridge Philosophical Society*, 33:518, 1937.

[13] E. A. Guggenheim. *Mixtures.* Oxford University Press, 1952.

[14] R. B. McLellan and W. W. Dunn. A quasi-chemical treatment of interstitial solid solution: its application to carbon austenite. *Journal of Physics and Chemistry of Solids*, 30:2631–2637, 1969.

[15] K. Alex and R. B. McLellan. A quasi-chemical approach to the thermodynamics of ternary solid solutions containing both substitutional and interstitial solute atoms. *Journal of Physics and Chemistry of Solids*, 32:449–457, 1971.

[16] J. A. Lobo and G. H. Geiger. Thermodynamics and solubility of carbon in ferrite and ferritic fe-mo alloys. *Metallurgical Transactions A*, 7A:1347, 1976.

[17] H. K. D. H. Bhadeshia. Thermodynamics of steels: carbon-carbon interaction energy. *Metal Science*, 14:230, 1980.

[18] H. K. D. H. Bhadeshia. Quasi-chemical model for interstitial solutions. *Materials Science and Technology*, 14:273–276, 1998.

[19] J. W. Chen. Ternary quasi-chemical model and first principles calculation of C-C interaction in ferrite. Master's thesis, University of Cambridge, Fitzwilliam College, Cambridge, CB3 0DG, 2004.

[20] J. R. Bradley G. J. Shiflet and H. I. Aaronson. A re-examination of the thermodynamics of the proeutectoid ferrite transformation in Fe-C alloys. *Metallugical Transactions A*, 9A:999, 1978.

[21] K. R. Kinsman and H. I. Aaronson. Discussion to J. M. Oblak and R. F. Hehemann. In *Transformation and Hardenability in Steels*, volume 15, Ann Arbor, Mich., 1967. Climax Molybdenum Co.

[22] B. Uhrenius. Optimization of parameters describing the c-metal interaction in ternary austenite. *Scandinavian Journal of Metallurgy*, 2(4):177–182, 1973.

[23] H. K. D. H. Bhadeshia. Thermodynamic extrapolation and martensite-start temperature of substitutionally alloyed steels. *Metal Science*, page 178, 1981.

[24] R. H. Siller and R. B. McLellan. The variation with composition of the diffusivity of carbon in austenite. *Transactions of the Metallurgical Society of AIME*, 245:697, 1969.

[25] R. H. Siller and R. B. McLellan. The application of first order mixing statistics to the variation of the diffusivity of carbon in austenite. *Metallugical Transactions*, 1:985, 1970.

[26] J. H. Hollomon J. C. Fisher and D. Turnbull. Absolute reaction rate theory for diffusion in metals. *Transactions AIME*, 175:202–215, 1948.

[27] H. K. D. H. Bhadeshia. Diffusion of carbon in austenite. *Metal Science*, 15:477, 1981.

[28] R. Trivedi and G. M. Pound. Effect of concentration-dependent diffusion coefficient on the migration of interphase boundaries. *Journal of Applied Physics*, 38:3569, 1967.

[29] Enrico Fermi. *Thermodynamics.* Dover Publications Inc., 1956.

[30] C. Zener. Impact of magnetism upon metallurgy. *Transactions AIME*, 203:619, 1955.

[31] H. A. Domian H. I. Aaronson and G. M. Pound. Thermodynamics of the austenite-¿proeutectoid ferrite transformation. II, Fe-C-X alloys. *Transactions of the Metallurgical Society of AIME*, 236:768, 1966.

[32] H. K. D. H. Bhadeshia. Thermodynamic analysis of isothermal transformation diagrams. *Metal Science*, 16:159, 1982.

[33] H. K. D. H. Bhadeshia and J. W. Christian. Bainite in steels. *Metallugical Transactions A*, 21A:767, 1990.

[34] J. W. Christian. *The theory of transformations in metals and alloys, part 1*. Pergamon Press, 2nd edition, 1975.

[35] R. C. Reed and H. K. D. H. Bhadeshia. Kinetics of reconstructive austenite of ferrite transformation in low alloy steels. *Materials Science and Technology*, 8:421, 1992.

[36] S. J. Jones and H. K. D. H. Bhadeshia. Kinetics of the simultaneous decomposition of austenite into several transformation products. *Acta Materialia*, 45:2911–2920, 1997.

[37] S. J. Jones and H. K. D. H. Bhadeshia. Competitive formation of inter- and intra- granularly nucleated ferrite. *Metallurgical and Materials Transactions A*, 28A:2005–2013, 1997.

[38] C. L. Magee. In *Phase transformations*, pages 115–156. Metals Park, OH, ASM, 1970.

[39] G. B. Olson and M. Cohen. A general mechanism of martensitic nucleation. *Metallurgical and Materials Transactions A*, 7(12):1897–1923, 1976.

[40] H. K. D. H. Bhadeshia. Bainite: Overall transformation kinetics. *Journal de Physique Colloque*, C4(43):443–448, 1982.

[41] G. I. Rees and H. K. D. H. Bhadeshia. Bainite transformation kinetics part 1. modified model. *Materials Science and Technology*, 8:985, 1992.

[42] G. I. Rees and H. K. D. H. Bhadeshia. Bainite transformation kinetics part 2. non-uniform distribution of carbon. *Materials Science and Technology*, 8:994–996, 1992.

[43] A. Ali and H. K. D. H. Bhadeshia. *Materials Science and Technology*, 6:781–784, 1990.

[44] C. Zener. Kinetics of the decompositon of austenite. *Transactions AIME*, 167:550, 1946.

[45] A. Hultgren. Isotherm omvandling av austenit. *Jernkontorets Annaler*, 4:403, 1951.

[46] R. F. Mehl and W. C. Hagel. The austenite: Pearlite reaction. *Progress in Metal Physics*, 6:74, 1956.

[47] R. Trivedi. Growth of dendritic needles from a supercooled melt. *Acta Metallurgica*, 18:287–296, 1970.

[48] J. M. Oblak and R. F. Hehemann. Structure and growth of Widmanstätten ferrite and bainite. in transformation and hardenability in steels. *Ann Arbo, MI: Climax Moly*, pages 15–33, 1967.

[49] R. F. Hehemann. The bainite transformation. In Phase transformations. Paper presented at a seminar of the ASM 12-13 October 1968. *Metals Park, OH: American Society of Metals.*, pages 397–432, 1970.

[50] H. Matsuda and H. K. D. H. Bhadeshia. Kinetics of the bainite transformation. *Proc. R. Soc. Lond. A*, 460:1707–1722, 2004.

[51] M. Avrami. Kinetics of phase change 1. *Journal of Chemical Physics*, 7:1103–1112, 1939.

[52] M. Avrami. Kinetics of phase change 2. *Journal of Chemical Physics*, 8:212–224, 1940.

[53] M. Avrami. Kinetics of phase change 3. *Journal of Chemical Physics*, 9:177–184, 1941.

[54] W. A. Johnson and R. F. Mehl. Reaction kinetics in processes of nucleation and growth. *Transactions of the Metallurgical Society of AIME*, 135:416–458, 1939.

[55] J. D. Robson and H. K. D. H. Bhadeshia. Kinetics of precipitation in power plant steels. *CALPHAD*, 20:447–460, 1996.

[56] J. D. Robson and H. K. D. H. Bhadeshia. Modelling precipitation sequences in power plant steels, part 1: Kinetic theory. *Materials Science and Technology*, 13:631–639, 1997.

[57] J. D. Robson and H. K. D. H. Bhadeshia. Modelling precipitation sequences in power plant steels, part 2: Application of kinetic theory. *Materials Science and Technology*, 28A:640–644, 1997.

[58] R. T. DeHoff and F. N. Rhines. *Quantitative Microscopy*. New York: McGraw Hill, 1968.

[59] S. Parker. *Modelling of Phase Transformations in Hot-Rolled Steels*. PhD thesis, University of Cambridge, 1997.

[60] L. E. Svensson H. K. D. H. Bhadeshia and B. Gretoft. Theory for allotriomorphic ferrite formation in steel weld deposites. In *Welding and Performance of Pipelines*, pages 517–529, London, U.K., 1987. Welding Institute.

[61] S. J. Jones. *Modelling inclusion potency and simultaneous transformation kinetics in steel*. PhD thesis, University of Cambridge, 1996.

[62] G. R. Srinivasan and C. M. Wayman. The crystallography of the bainite transformation- pt. 1. *Acta Metallurgica*, 16:609–620, 1968.

[63] G. R. Srinivasan and C. M. Wayman. Transmission electron microscope study of the bainite transformation in iron-chromium-carbon alloys. *Acta Metallurgica*, 16:621–636, 1968.

[64] L. C. Chang and H. K. D. H. Bhadeshia. Austenite films in bainitic microstructures. *Materials Science and Technology*, 11:874–881, 1995.

[65] E. C. Bain. Alloying elements in steel. *Cleveland, OH, American Society of Materials*, 1939.

[66] R. A. Higgins. *Engineering Metallurgy: Applied Physical Metallurgy*, volume 1. Arnold, sixth edition, 1993.

[67] F. Wever and W. Jellinghaus. The ternary system iron-chromium-nickel. *Mitt. Kaiser-Wilhelm-Inst. Eisenforsch*, 14:85, 1932.

[68] K. W. Andrews. Empirical formulae for the calculation of some transformation temperatures. *Journal of the Iron and Steel Institute*, 184:414, 1956.

[69] R. L. Bodnar and S. S. Hansen. Effects of austenite grain size and cooling rate on Widmanstätten ferrite formation in low alloy steels. *Metallurgical and Materials Transactions A*, 25A:665–675, 1994.

[70] H. K. D. H. Bhadeshia P. G. Self and W. M. Stobbs. Lattice spacings from lattice fringes. *Untramicroscopy*, 6:29–40, 1981.

[71] L. Chabbi U. Urlau J. W. Chen H. Roelofs, S. Hasler and H. K. D. H. Bhadeshia. Multiphase structures in case hardening steels following continuous cooling. In *New Development on Metallurgy and Applications of High Strength Steels*, Buenos Aires, 2008. Ternium, Tenaris and Asociación Argentina de Materiales.

[72] H. E. Boyer and A. G. Gray, editors. *Atlas of Isothermal Transformation and Cooling Transformation Diagrams*. American Society for Metals, 1977.

[73] H. E. Boyer and A. G. Gray, editors. *Atlas of Isothermal Transformation and Cooling Transformation Diagrams*, page 13. American Society for Metals, 1977.

[74] J. H. Hollomon and L. D. Jaffe. Time-tempering relations in tempering steels. *Transactions AIME*, 162:223, 1945.

[75] Discussion. In *AIME T. P. 2059*, pages 17–21, September 1946.

[76] S. Hasler H. Roelofs J. W. Chen, H. K. D. H. Bhadeshia and U. Ulrau. Complete calculation of steel microstructure for strong alloys. In *New Development on Metallurgy and Applications of High Strength Steels*, Buenos Aires, 2008. Ternium, Tenaris and Asociación Argentina de Materiales.

[77] A. Brownrigg. Boron in steel - a literature review 1956-1972. *The Journal of the Australian Institute of Metals*, 18(3):124, 1973.

[78] H. K. D. H. Bhadeshia and L. E. Svensson. Model for boron effects in steel welds. *International conference on modelling and control of joining processes, Orlando, Floridan (1993), Editor: T. Zacharia, American Welding Society*, pages 153–160, 1993.

[79] AIME. *Boron in Steel*, Warrendale, PA, USA, 1980.